

# Computational Hydrodynamic Stability and Flow Control Based on Spectral Analysis of Linear Operators

Shervin Bagheri

Received: 8 November 2011 / Accepted: 8 November 2011  
© CIMNE, Barcelona, Spain 2012

**Abstract** This paper considers the analysis and control of fluid flows using tools from dynamical systems and control theory. The employed tools are derived from the spectral analysis of various linear operators associated with the Navier–Stokes equations. Spectral decomposition of the linearized Navier–Stokes operator, the Koopman operator, the spatial correlation operator and the Hankel operator provide a means to gain physical insight into the dynamics of complex flows and enables the construction of low-dimensional models suitable for control design. Since the discretization of the Navier–Stokes equations often leads to very large-scale dynamical systems, matrix-free and in some cases iterative techniques have to be employed to solve the eigenvalue problem. The common theme of the numerical algorithms is the use of direct numerical simulations. The theory and the algorithms are exemplified on flow over a flat plate and a jet in crossflow, as prototypes for the laminar-turbulent transition and three-dimensional vortex shedding.

## 1 Introduction

Despite the long history of fluid mechanics we lack a complete understanding of why fluid flows have a tendency to change pattern when perturbed. Two examples of flows that

transition from an organized and steady state to an irregular and fluctuating state when perturbed are the laminar-turbulent transition of flows on slender bodies and the alternating shedding of vortices of flows behind bluff bodies. It has been known for over a century that these flow phenomena are governed by the basic conservation laws of mechanics, but the difficulties that arise when one attempts to solve or analyze the system of equations have proved to be a major obstacle.

In this paper, we are concerned with the laminar-turbulent transition of a flow along a flat plate and the vortex shedding in a jet in a crossflow. In particular, a global viewpoint is adopted where the flow is allowed to move as it wishes in the physical domain without assumptions about or constraints on its dynamics. There are countless examples in both nature and industry pertaining to the study of the flow along a flat plate, since it is the archetype of boundary layer flows. In these flows the layer of fluid in the immediate vicinity of the surface is sheared, resulting in rapid velocity change over a short distance normal to the surface. Examples of boundary-layer flows are the layer of air near the ground or near an aircraft wing, where the observed flow pattern depends on the smoothness of the surface, level of diurnal heat, moisture, turbulence levels far away from the surface and so on. The fundamental issue is a physical and mathematical understanding of the transition of a laminar smooth flow to a turbulent unpredictable one. Compared to a laminar flow, a turbulent flow is more expensive and often undesirable in practical applications. For instance, to sustain a turbulent flow in a pipe, more pressure is required to maintain the same volume of discharge as a laminar flow. Also, turbulent flow around vehicles increases the friction, resulting in higher fuel costs. Understanding the transition process is adjacent to the field of flow control and in particular *transition control*, where the aim is to modify the flow

---

S. Bagheri  
DICAT, Università di Genova, Via Montallegro 1,  
16145 Genova, Italy

S. Bagheri (✉)  
Linné Flow Centre, Royal Institute of Technology (KTH),  
10044 Stockholm, Sweden  
e-mail: [shervin.bagheri@mech.kth.se](mailto:shervin.bagheri@mech.kth.se)

conditions in order to delay the laminar-turbulent transition. The necessary flow conditions can be obtained by changing initial and boundary conditions (e.g. surface roughness), the flow properties (e.g. velocity, pressure distribution, turbulence level) or the fluid properties (e.g. density, viscosity and temperature).

The classical example of vortex shedding is the von Kármán vortex street that can be observed in the formation of clouds behind mountains and islands or in the flow behind vehicles, buildings and chimneys of factories. It is of great practical significance to identify the source from which alternating pairs of vortices are shed downstream, since they often lead to large structural vibrations, acoustic noise and resonance. Another example of a flow dominated by vortex shedding is the jet in crossflow, which is found when gas or liquid is injected through a small orifice into a crossflow of a similar fluid. The flow is related to a wide range of applications. A few examples are plume dispersal from smoke stacks and volcanos, reduction of environmental pollution (the “jet” represents a stream flowing into a lake) and film cooling applications in jet engine combustors.

This introductory section is organized as follows. Section 1.1 describes the laminar-turbulent transition of a flow over a flat plate in a phenomenological way and introduces the key ideas behind transition control. Section 1.2 gives an insight into the physics of the jet in crossflow obtained by direct numerical simulations and paves the way for the analysis in Sect. 2. The present section concludes with an overview of the main results of the paper and a brief motivation of the global mode approach undertaken in the subsequent section.

### 1.1 Physics of the Flow on a Flat Plate

Viscous flows in straight tubes, pipes, channels and on flat plates are steady for sufficiently small values of the (dimensionless) number  $UL/\nu$ , where  $U$  and  $L$  are, respectively, a velocity and a length characteristic of the flow and  $\nu$  is the kinematic viscosity of the fluid. At higher values, however, the flow shows intermittent oscillations and eventually becomes highly irregular and unsteady. This transition from a laminar flow to a turbulent one at a critical *Reynolds number*,  $Re = UL/\nu$  was first investigated in a pipe by Reynolds [82].

Consider a steady uniform stream of flow with speed  $U$  that encounters a flat plate of length  $L$ . It is appropriate to define the Reynolds number as  $Re_x = Ux/\nu$  where  $0 \leq x \leq L$  is the distance on the plate from the leading edge. The critical Reynolds number,  $Re_x$ , for the laminar-turbulent transition is notoriously difficult to determine. Transition can occur abruptly, gradually and at completely different locations on the plate depending on the size, spatial structure and temporal behavior of the disturbances that can be found

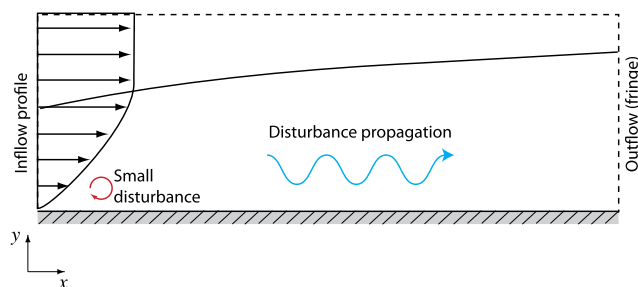


**Fig. 1** Sketch of a numerical experiment of the evolution of a wavepacket disturbance in a flat-plate boundary layer. The Reynolds number at the computational inlet is  $Re_x \approx 3 \times 10^5$  and the computational outlet it is  $Re_x \approx 1 \times 10^6$ . The numerical parameters are given in Table 5 (case 3D-NLIN-BL) in Sect. 4.4

in the laboratory or numerical experiments. For example, the presence (or combination) of acoustic waves, roughness on the plate, vortical structures in the free stream critically affects the transition process. A number of books [15, 89, 91] treat the different laminar-turbulent transition scenarios in boundary layers. We proceed by a simple numerical experiment to characterize the evolution of a small disturbance in the flow on a flat plate in order to highlight the essential physics that is relevant for our purposes. In practice, flow conditions are significantly more complicated than our single-disturbance example but the underlying physics is essentially the same. The simulation is performed using the pseudo-spectral code described in Sect. 4.4.

A sketch of the setup is given in Fig. 1. Prandtl [79] introduced the concept of a boundary layer, as a thin (about 2–5 mm on a 180 cm plate) layer, where the effects of viscosity are important. This layer is the region (marked in Fig. 1 with solid black line) where diffusion of the vorticity generated at the surface is significant. The thickness of the laminar boundary layer  $\delta$  is related to the viscosity and the downstream distance as  $\delta \sim (\nu U/x)^{-1/2}$ , which indicates that the layer grows slowly in the downstream direction. Prandtl showed that for the boundary layer, the Navier–Stokes equations (see Sect. 2.1) can be reduced to a simpler form and it was Prandtl’s student Blasius [18] who formulated a nonlinear ODE and solved it, with the velocity profile shown schematically (as the inflow profile) in Fig. 1. Inside the boundary layer and far upstream in the flow domain we place a small localized perturbation. As the disturbance is released, it propagates in the downstream direction and its fate depends on its initial amplitude and on its initial physical shape. The disturbance could for instance be introduced by using a loudspeaker to generate a short pulse, injected through a small hole in the plate. The volume of the loudspeaker would then determine the disturbance amplitude and the structure of the hole in the plate its shape.

Figure 2 shows “snapshots” of the disturbance (top view of the plate) at three different instances in time using iso-contour levels of the  $\lambda_2$ -criterion [46]. The  $\lambda_2$  levels are

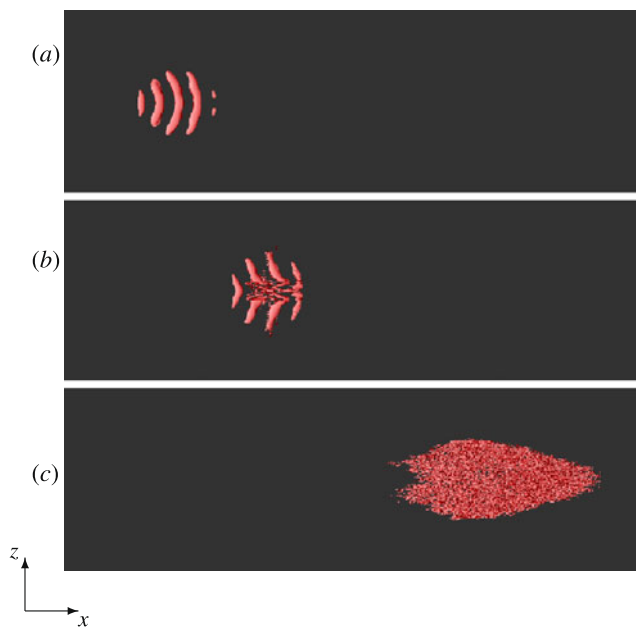


**Fig. 2** Snapshots of the disturbance at  $t = 300$ ,  $600$  and  $t = 1000$  are shown in (a), (b) and (c) respectively. Red iso-contour levels depict the  $\lambda_2$ -criterion. The plate is shown in black and viewed from top (Color figure online)

useful to identify vortical structures in the flow. In the initial stage (Fig. 2(a)), the disturbance is nearly two dimensional in the spanwise direction ( $z$ ) and it grows in amplitude rapidly. After approximately 300 time units the disturbance has a different structure; now significant three-dimensional components (Fig. 2(b)) and smaller wavelengths are observed. Finally at  $t = 1000$ , a localized turbulent spot is developed with a typical arrow-shaped structure. The disturbance is now characterized by a wide range of scales in all spatial directions (Fig. 2(c)). The turbulent spot eventually leaves the computational domain and the flow returns to the steady boundary layer. We have thus identified three distinct flow regimes; (i) *the laminar region* where a smooth disturbance grows in size; (ii) *the transition region* where there is breakdown of the disturbance into a significantly more complicated structure; (iii) *turbulent region* where a turbulent spot emerges.

Depending on the Reynolds number, the drag due to the skin friction in the laminar region can be as much as an order of magnitude less than that in the turbulent region [89]. For an aircraft<sup>1</sup> or a vehicle the reduced drag means longer range, reduced fuel cost or increased speed. To illustrate this, for each snapshot in Fig. 2, the streamwise velocity component  $u$  at the location on the plate where the disturbance is

<sup>1</sup>Friction drag constitutes more than half of the total aircraft drag, with 18 %, 4 %, 3 % and 3 % for wing, horizontal tail plane, fin and nacelles, respectively. If the flow were laminar on 40 % of the surfaces, the total drag would be reduced by 16 % [92].

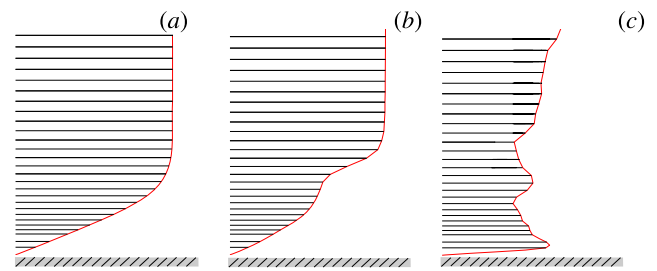


**Fig. 3** Velocity profiles of the streamwise component ( $u$ ) as a function of the wall-normal distance from the plate ( $y$ ). The profiles (a), (b) and (c) correspond to the snapshots (a)–(c) in Fig. 2 and are extracted approximately in the center of the disturbance

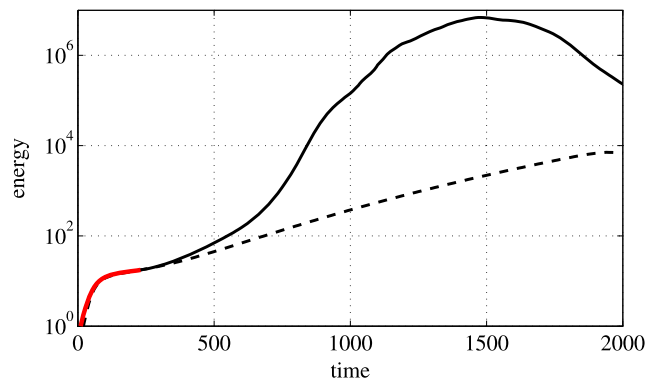


**Fig. 4** The evolution of the kinetic energy of a disturbance in time corresponding to a nonlinear simulation (solid black) and linear simulation (dashed black). The initial growth phase where the linear and nonlinear curves nearly collapse is marked in red (Color figure online)

present is shown as a function of the wall-normal coordinate  $y$  in Fig. 3. For the first snapshot, the characteristic laminar boundary-layer profile (Fig. 3(a)) is observed, but already after a short period, the disturbance has modified the profile considerably (Fig. 3(b)), and an inflection point can be observed. The third profile (Fig. 3(c)) extracted from the turbulent spot is very distorted and the smooth boundary layer has changed its character completely. The turbulent profile changes rapidly over a very short distance normal to the surface compared to the laminar profile. As a consequence the local shear stress is considerably higher in the turbulent region.

### 1.1.1 Linear Amplification

If the upstream disturbances in the boundary layer are small—determined by the receptivity [30] of the boundary layer to external flow conditions—the initial stage in the transition process is a linear amplification. In Fig. 4 the time evolution of the disturbance kinetic energy of the numerical experiment is shown with a black solid line. We observe a rapid energy growth until the disturbance is propagated out of the computational domain at  $t = 1500$ . In the

figure, the kinetic energy of a disturbance with an infinitesimal amplitude—where the nonlinear effects are neglected—is shown by the dashed line. We observe that the energy of the infinitesimal amplitude and the finite-amplitude disturbance initially grow with the same rate.

The linearized flow is considerably easier to analyze, since the temporal part of the disturbance can be decomposed into a number of waves that grow or decay independently of each other as predicted by linear stability theory. However, for the boundary layer, no single wave grows exponentially in time; in fact all waves decay for long times, but their superposition may result in a wavepacket that grows as it propagates downstream. Since late 1980's a new (linear) mathematical approach to characterize the disturbance behavior has emerged, based on transient growth analysis [81], pseudo spectra [102], categorizing flows as noise amplifiers or oscillators [42] and analysis of input-output norms [47].

### 1.1.2 Transition Control

The natural question that arises is: If we can suppress the growth of the disturbance, can we delay the transition to turbulence? In many cases the answer is yes; for our numerical example above if we assign an order of magnitude smaller amplitude to the initial disturbance, it breaks down further downstream and the development of the turbulence spot is delayed. One major objective of flow control is thus to damp the amplitude of disturbances at an early stage in the boundary layer in order to delay transition to turbulence. Since we observe that the disturbance energy growth is initially a linear process [52, 91], transition control focuses mainly on the simpler linear system.

If the necessary flow conditions resulting in lower disturbance growth are achieved in a way that requires energy input, one needs to introduce actuators, such as loudspeakers, synthetic jets [94], electro-magnetic actuators [74], plasma actuators [32] or various MEMS actuators [39] constructed using micro-machining techniques. Flow control is indeed engineering, where besides the type of actuators, the distribution and location of actuators has to be determined. In general, the more physical insight one has into the disturbance behavior, the better design decision one is able to make. If we know *exactly* what type of disturbances are present in the flow, e.g. if perturbations are traveling waves or in the form of elongated streamwise vortices called streaks, using the actuators we can introduce other disturbances that counteract them. For example a second wave of appropriate amplitude and phase would cancel the traveling wave by interference [67] or blowing and suction at the wall [37] would cancel out the streaks. If we don't know the exact form of the disturbance, we can monitor the flow using sensors and adjust the actuation accordingly to achieve the control objectives. This type of control is known as feedback control,

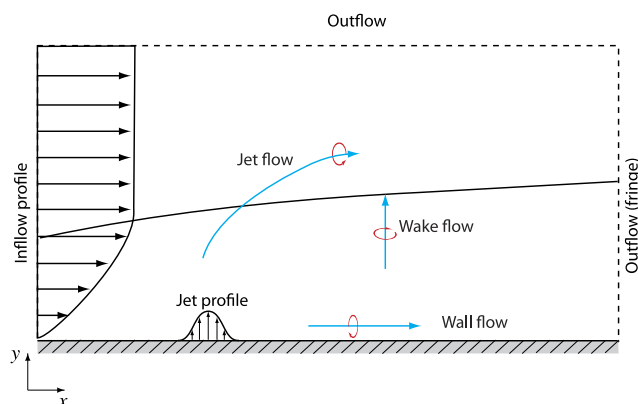


**Fig. 5** Sketch of a numerical experiment of the jet in crossflow. The initial fields are the flat-plate boundary layer profile and a parabolic jet profile. The ratio between the jet flow and the crossflow denoted by  $R$ , is three. The numerical parameters are given in Table 5 (case JCF) in Sect. 4.4

where in addition to actuators, the design and distribution of sensors have to be taken into account. The sensor measurements could be a few pressure measurements using a small microphone membrane mounted flush to the wall, velocity measurements using hot-wire anemometry near the wall or shear-stress measurements using thermal sensors (wall wires).

## 1.2 Physics of the Jet in a Crossflow

The jet in crossflow (JCF) is the interaction of two well-studied canonical flows, the flat-plate boundary layer flow and the flow ejected through an orifice into a quiescent environment, a free jet flow. Since vorticity cannot be created or destroyed in the interior of a flow and is produced only at boundaries (or by initial conditions), the orifice is the only source of vorticity for a free jet and consequently, the dynamics of jets are commonly described by convection, diffusion, stretching and turning of vorticity in an otherwise irrotational flow. In contrast (as discussed previously), in a flat-plate boundary layer, vorticity generated at the wall convects and diffuses in the wall-normal direction, causing growth of the boundary layer. The interaction of the boundary layer and the jet vorticity results in a highly unsteady fully three-dimensional flow and a number of “vortical structures”, which refer to flow features that are relatively well organized and appear rotational in nature. These structures can be identified in three different regions of the flow domain as shown schematically in Fig. 5; the jet region, the wake region and the wall region. In particular, four large-scale vortical structures of the JCF have been studied extensively by researchers; (1) the counter-rotating vortex pair [70]; (2) the horse-shoe vortex and its wall vortices [51]; (3) loop-like or ring-like vortices [50, 61] and (4) upright vortices [27, 50].

### 1.2.1 Steady-Unsteady Transition

We will now illustrate how a steady jet in crossflow gradually exhibits unsteady behavior that is sustained for all times when it is perturbed. One major obstacle towards understanding the physical mechanisms of the unsteadiness in the flow is that the “natural state” of the JCF is unsteady. A steady flow will never be observed in laboratory experiments or in applications. One of the advantages of numerical experiments is that we can artificially force the unsteady flow to become steady, in order to better understand the underlying physics. Figure 5 shows a sketch of the numerical setup used to simulate the jet in crossflow. In addition to the laminar boundary-layer profile at the upstream inlet investigated in the previous section, an inhomogeneous parabolic boundary condition is imposed in order to model a laminar pipe flow mounted to the plate.

The steady flow obtained by filtering out all the unsteady structures [2] is “released” and its evolution in time is followed by a numerical simulation. A disturbance is not explicitly introduced, instead background numerical noise acts as flow perturbation. Figure 6 shows the  $\lambda_2$  criterion (red) and the streamwise velocity (gray) of a sequence of snapshots from the numerical experiment. We observe how a well organized smooth flow is gradually transformed into a more complicated irregular flow with significantly smaller vortices. The most dominant feature of the steady flow (label ① in Fig. 6(a))—and the largest vortical structure of the JCF—is the *counter-rotating vortex pair* (CVP) that takes the form of two distinct tubes. The direction of rotation is in such a way that fluid is lifted up in between the vortices. This vortex pair develops because the crossflow skirts laterally around the jet and shears the jet fluid along its edges and then folds the face of the jet over itself to form the CVP. The CVP emerge from the center of an cylindrical vortex sheet (or a shear layer) developed when the crossflow and the jet fluid come into contact. Close to the wall, when the crossflow encounters the jet, part of the crossflow is deflected in direction of the jet flow and part of it is pushed towards the wall, to form a spanwise oriented vortex, the *horse-shoe vortex* (label ③ in Fig. 6(a)). This vortex wraps around the base of the jet and forms a streamwise vortex pair, the *wall vortices* in the wall region, as shown in by the gray contour levels of the streamwise velocity (label ② in Fig. 6).

After a long time ( $t = 300$ ) the disturbances triggered by the background noise have grown sufficiently in amplitude to modify the steady flow. As shown in Fig. 6(b), the disturbance modifies mainly the CVP; a varicose out-of-phase oscillation of the two vortex tubes is observed and “arches” are created, i.e. the vortex loops coil up around the upper side of the CVP and their bases join with the CVP. This type of symmetric structures are associated with the roll-up of the cylindrical vortex sheet. Finally, at  $t = 500$ , the symmetric

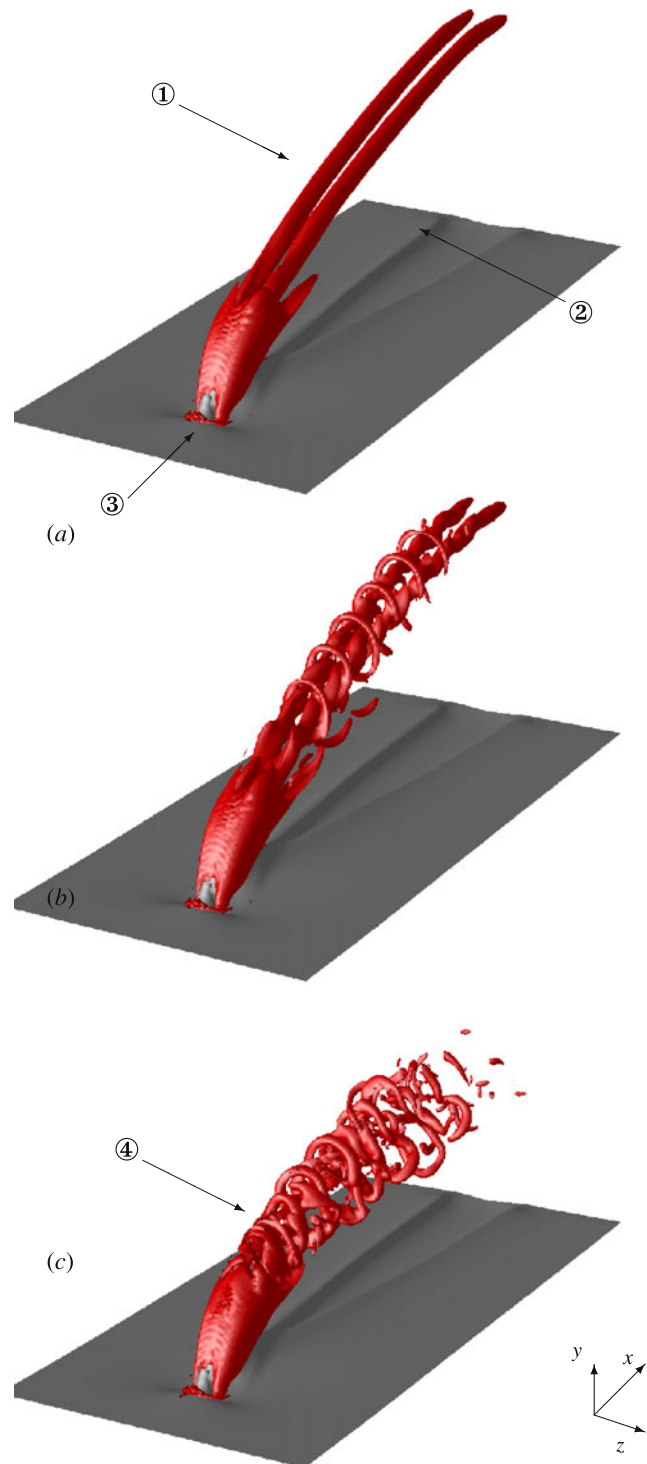


**Fig. 6** Three instantaneous snapshots of the steady-unsteady transition at  $t = 0$ , 300 and  $t = 500$  are shown in (a), (b) and (c) respectively. Red contour levels represent the  $\lambda_2 = -0.09$  and the gray contour levels represent the streamwise velocity  $u = 0.2$ . See text for explanations of labels ①–④ (Color figure online)

vortex loops are distorted into half-ring shaped asymmetric vortices (label ④ in Fig. 6(c)) which rapidly break down into a series of smaller vortices. This flow is sustained for

all times; half-ring shaped vortices are continuously generated from an internal source upstream, they grow as they are convected downstream, and finally they gradually dissipate due to viscosity.

### 1.2.2 Self-Sustained Oscillatory Behavior

It is of interest to determine whether the unsteadiness depends on the external disturbance environment (in our case numerical noise due to discretization errors) or if it is an intrinsic property of the JCF. It is well known [43] that (co-flowing) shear layers amplify upstream incoming disturbances and the frequencies observed in the flow depend highly on the frequencies present in the external disturbance environment. However, under certain flow conditions a resonance can arise where one observes a few dominant frequencies, independent of the spectral content of the noisy outside environment. A resonance can for example be triggered when one introduces a rigid body at an appropriate downstream location in the flow. The body creates a pressure feedback loop giving rise to oscillations at discrete resonant frequencies.<sup>2</sup> However, such a feedback loop can also be produced by purely hydrodynamic means, where a downstream body is not necessary. Such flows often have a region of significant reversed flow (e.g. backflow). A classical example is the von Kármán vortex street developing behind a circular cylinder at low Reynolds numbers. The unsteadiness usually consists of small patches of vorticity being released periodically from a location, i.e. *vortex shedding*, where the oscillation frequency is insensitive to external low-amplitude forcing. Many examples of hydrodynamic resonances exist, [14, 21, 68, 97], and during the last decade a large number of experimental and numerical studies have been devoted to categorization of flows as oscillators or amplifiers [41, 42].

The simplest approach, that provides only supporting evidence for oscillatory behavior, is to place probes in the flow and study single-point spectral data. The time signal of a probe located in the shear layer of the JCF is shown in Fig. 7(a), where Fourier analysis reveals a dominant frequency of Strouhal number  $St_2 \equiv f_2 D / V_{\text{jet}} = 0.14$ . In addition to this high frequency, a distinct low frequency  $St_1 = 0.017$  is observed by a probe located in the wall region downstream of the jet orifice (Fig. 7(b)). Several time signals from other probes have been obtained and all the additional frequency peaks are linear combinations of  $St_1$  and  $St_2$ , corresponding to higher harmonics triggered by nonlinear interactions between the two main frequencies.

There is some evidence [36] and numerous studies [4, 5, 14, 28, 64, 99] that connect self-sustained oscillations in fluid systems with large unsteady separated regions. The

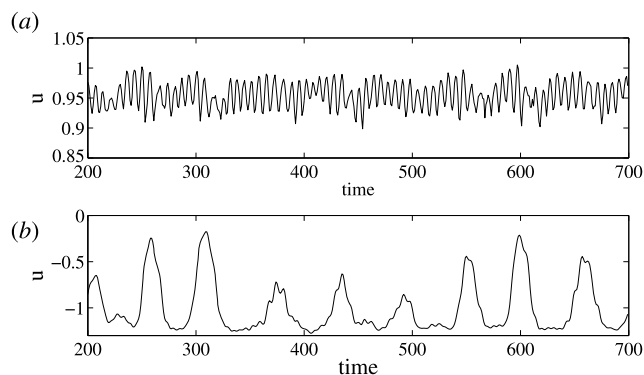


**Fig. 7** Time signals of two probes measuring the streamwise velocity  $u$  component at a single point in the flow. In (a) the probe is placed in the shear layer and in (b) near the separated region downstream of the jet near the wall

flow under investigation here has two regions of reversed flow: a smaller, steady separated region upstream of the jet which coincides with the horse-shoe vortex, and a larger unsteady region of reversed flow directly downstream of the emerging jet near the wall. The animation of the DNS data shows that the separation region downstream of the jet orifice is highly unsteady. In the upper part of this region, patches of negative  $u$  are periodically released in the wall-normal direction with the fundamental frequency  $St_2 = 0.14$ . The separated region also oscillates with the lower fundamental frequency  $St_1 = 0.017$ , however this time the entire recirculation zone downstream of the jet is periodically moving back and forth in the spanwise direction. In Fig. 8, the movement of the separation region, downstream of the jet, oscillating in two directions with two distinct frequencies is shown.

### 1.3 Paper Overview

In the previous two sections, using numerical experiments, we have observed the following:

- (i) The breakdown of a small-amplitude disturbance in a boundary layer, resulting in a turbulent spot. Our interest lies in damping the growth of disturbances at an early stage in the transition process in order to delay the development of turbulence.
- (ii) The nonlinear saturation of a small-amplitude disturbance (background numerical noise), resulting in self-sustained oscillatory behavior of the flow. Our interest lies in understanding the underlying mechanisms of the disturbance growth and identifying the spatial flow structures associated with the oscillations.

The aim of the present paper is to study these two phenomena using *global modes*.

<sup>2</sup>Similar to bounded states in quantum mechanics, resulting in a discrete energy spectrum.

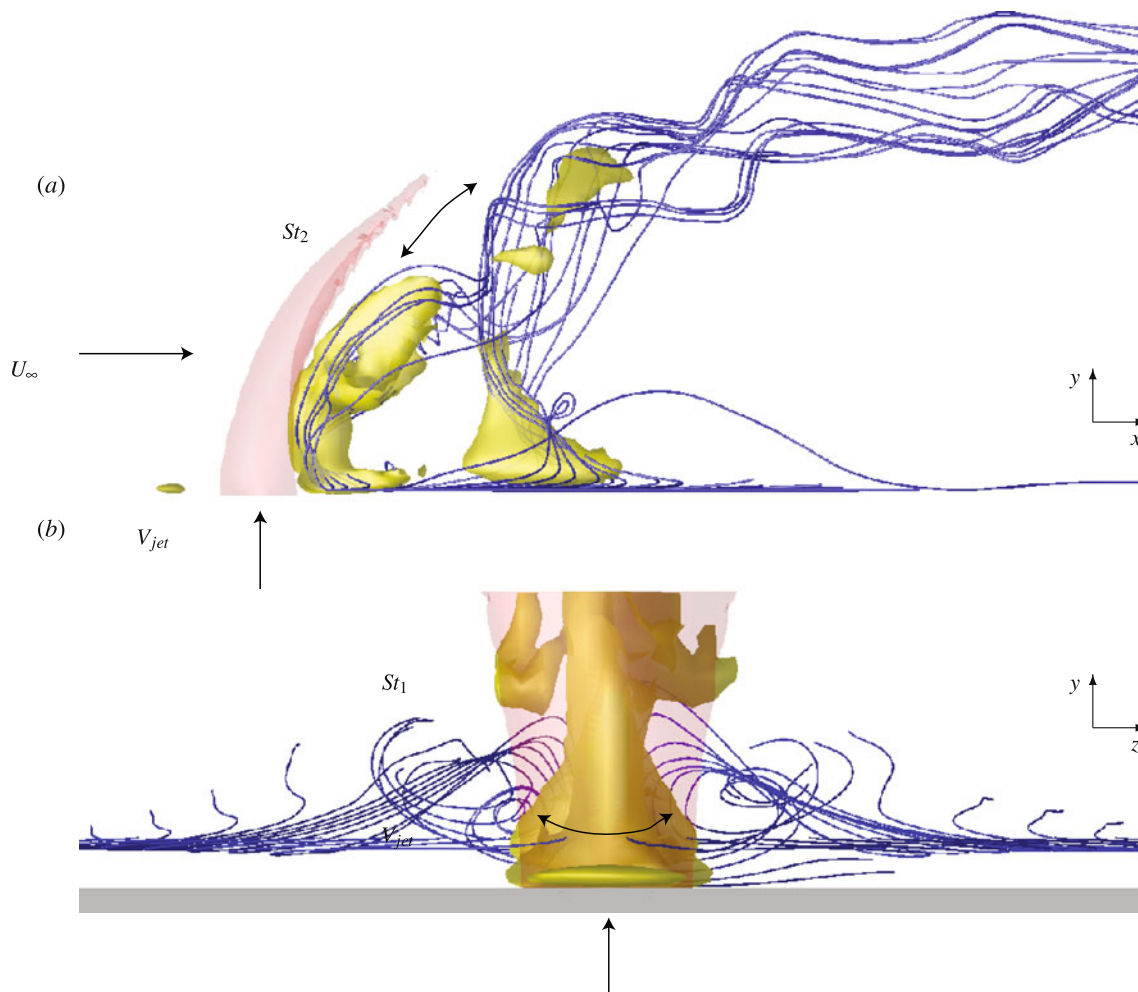


**Fig. 8** Yellow iso-contour levels represent zero streamwise velocity, marking the region of reversed flow, red levels show positive wall-normal velocity, marking the jet fluid. The blue streamlines originate from the crossflow fluid and show how the crossflow is sucked into the jet (a) and how it develops a pair of streamwise wall vortices (b).

Top figure is a side view, where the region of reversed flow oscillates back and forth in the wall-normal direction. Bottom figure is a front view, illustrating the movement of the separated region in the spanwise direction (Color figure online)

### 1.3.1 Global Modes

The concept of global modes in fluid mechanics has over the last two decades been used in various contexts. In the early nineties it was part of a theoretical framework [42] for the understanding of self-sustained oscillations. A global mode was defined as a flow structure that oscillates with one single frequency and satisfies certain boundary conditions, similar to bound states in quantum mechanics. More recently [38, 99], global modes have been associated with the eigenmodes of the linearized Navier–Stokes operator for flows that have two or three inhomogeneous spatial directions. The term “global” in this context is used to differentiate from the approach to the classical local hydrodynamic stability analysis applicable to parallel shear flows, for example the eigenmodes of the Orr–Sommerfeld/Squire equations. A third usage of the term “global mode” is to denote any localized

vortical structure that is contained in the full global spatial domain. In this sense, global modes are not simply instantaneous snapshots of flow fields containing vortical structures, rather they are extracted from experiments or numerical simulations by some method to isolate certain dynamical features, such as coherent structures either growing with one rate, oscillating with one frequency or containing the largest possible kinetic energy, etc. We adopt the latter definition of a global mode.

In particular, the following global modes are considered:

- (i) *Linear global eigenmodes* are small-amplitude perturbations that grow or decay exponentially and pulsate with one frequency. They are useful to determine the linear stability of a steady flow and to describe the underlying physical mechanisms for perturbation growth.

- (ii) *Koopman modes* represent spatial flow structures with time-periodic motion. They are useful to characterize oscillatory nonlinear flow dynamics.
- (iii) *Balanced modes* are used to construct low-dimensional models of large-scale flow systems in order to design efficient controllers for transition delay. The reduced-order model captures the relation between inputs (disturbances and actuators) and outputs (sensors used for flow measurements).

### 1.3.2 Organization

In Sect. 2, the transition from a steady flow to an unsteady one is analyzed using linear global eigenmodes and Koopman modes. The global mode theory is presented for general fluid systems followed by examples on the jet in crossflow. Section 3 gives a treatment of linear systems theory including model reduction and control design. Along the way, the concepts are illustrated on the flat-plate boundary layer flow. Section 4 provides a detailed description of the numerical algorithms used to compute global modes, with a few simple examples to demonstrate convergence behavior of the methods. The paper finalizes with a short summary and outlook in Sect. 5.

## 2 Flow Analysis Using Global Modes

The jet in crossflow is a complex flow. It involves the interaction of at least four shear layers, namely the boundary layer, the jet shear layer, a separated shear layer and a wake. Due to the strong coupling between the shear layers, one is obliged to study the *global* behavior of the flow, in order to obtain a complete picture of the dynamics. The complete steady-unsteady dynamics of the jet in crossflow can be divided into a number of stages. Figure 9 shows the time evolution of the streamwise velocity component at  $(x, y, z) = (12, 6, \pm 2)$  extracted from the numerical simulation discussed in Sect. 1.2. The trajectory starting at the steady flow at  $t = 0$  (marked with filled black circle in Fig. 9), departs from the steady solution and advances towards an attractor region where the trajectory appears to fluctuate randomly back and forth. In this section, we describe the dynamics in the two regions (marked schematically with circles in Fig. 9): the linear dynamics in a small neighborhood (black circle) of the steady solution and the nonlinear dynamics evolving in the attractor region (blue circle).

Global linear stability analysis determines whether exponentially growing perturbations exist in a neighborhood of the steady solution. These perturbations, called linear global eigenmodes, represent spatially coherent structures that grow or decay exponentially and pulsate with one frequency. The fact that the instabilities are global modes does

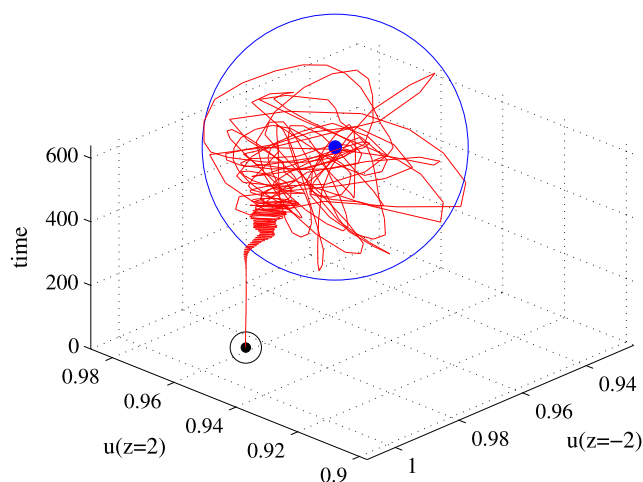


**Fig. 9** The streamwise velocity at  $(x, y, z) = (12, 6, \pm 2)$  is plotted as function of time. The black circle marks the region where the flow behavior is linear, whereas the blue circle marks the nonlinear flow dynamics. The figure shows the entire linear-transient-nonlinear development (Color figure online)

not mean that the elementary mechanisms of the instabilities are not local. In fact, this is often the case, where locally the inviscid Kelvin-Helmholtz instability, inviscid elliptic instability or viscous Tollmien-Schlichting waves are active, but the coupling between them is a truly global phenomenon. If unstable global eigenmodes exist, disturbances will grow until they saturate nonlinearly to a more complicated state. For self-sustained oscillatory flows, the nonlinear flow commonly evolves near a limit cycle or quasi-periodic attractors. The most convincing reports so far are the milestone experiments of [80] that showed that the vortex shedding behind a circular cylinder at low Reynolds number is due to an amplified global instability that saturates via Hopf bifurcation to a self-sustained limit cycle.

The flow dynamics evolving in the attractor region is difficult to analyze by studying individual trajectories. To understand the global features of the unsteady flow, an easier task is to study its statistical properties, such as time-averages. One approach, explained in this paper, is the decomposition of the unsteady nonlinear dynamics into a set of global modes, referred to as the Koopman modes. The modes can be considered as a generalization of the time-averaged mean flow; the first mode is the mean flow, whereas other Koopman modes are harmonic averages, i.e. spatial structures that display periodic behavior in time. In this way we can identify the flow structures that oscillate with precisely the same frequency as the vortex shedding observed in the flow.

This section is organized as follows. In Sect. 2.1, we present the governing equations for an incompressible flow. In Sect. 2.2, we define the linear global eigenmodes and discuss their significance for the jet in crossflow. Finally, in the last part of the section we introduce the spectral properties

of the Koopman operator and the nonlinear analysis of the jet in crossflow.

## 2.1 Equations of Motion

The Navier–Stokes equations governing the rate of change of momentum per unit volume of an incompressible fluid are given by

$$\frac{\partial \mathbf{u}}{\partial t} + (\mathbf{u} \cdot \nabla) \mathbf{u} = -\nabla p + \frac{1}{\text{Re}} \nabla^2 \mathbf{u} + \mathbf{F} \quad (1a)$$

$$\nabla \cdot \mathbf{u} = 0 \quad (1b)$$

where  $\mathbf{u}(\mathbf{x}, t) = (u, v, w)^3$  and  $p(\mathbf{x}, t)$  are the velocity and pressure in space  $\mathbf{x} = (x, y, z) \in \Omega$  and time  $t \geq 0$ ,  $\nabla = (\partial_x, \partial_y, \partial_z)$  is the divergence operator and the term  $\mathbf{F} = (f_1, f_2, f_3)$  represents a body force. The Reynolds number is defined as

$$\text{Re} = \frac{U_\infty \delta_0^*}{\nu}$$

where  $U_\infty$  is the constant streamwise free-stream velocity,  $\delta_0^*$  is the displacement thickness at a particular distance from the leading edge  $x_0$  and  $\nu$  is the kinematic viscosity. The flow evolves in the spatial domain defined by,

$$\Omega = \{\mathbf{x} \in \mathbb{R}^3 \mid 0 \leq x \leq L_x, 0 \leq y \leq L_y, -L_z/2 \leq z \leq L_z/2\}.$$

For all flows investigated in this paper the solutions to (1a)–(1b) are periodic in the streamwise  $x$  and spanwise  $z$  directions with periodicity  $L_x$  and  $L_z$  respectively. For the flow on a flat plate and the jet in crossflow, periodic boundary conditions in the streamwise direction are artificially enforced by  $\mathbf{F}$ . In the wall-normal direction  $y$ , different boundary conditions are imposed depending on the flow configuration. See Sect. 4.4.2 and Table 5 for details on the imposed boundary conditions.

We omit entirely any discussion of partial differential equations and the subsequent analysis is presented for finite-dimensional systems—ordinary differential equations—for simplicity. One can either think that the flow is represented on a number of grid points obtained by discretizing the domain  $\Omega$ , or that the dynamics takes place over some finite-dimensional smooth manifold [98].

Henceforth, let the flow dynamics be described by an  $n$ -dimensional nonlinear system

$$\dot{\mathbf{u}} = \mathbf{f}(\mathbf{u}) \quad (2)$$

<sup>3</sup>A note on the basic notation used through out the paper is appropriate at this point. Square brackets [ and ] are used to construct matrices and vectors, i.e.  $[1 \ 2]^T$  is a column vector  $\in \mathbb{R}^{2 \times 1}$  which is abbreviated as  $\mathbb{R}^2$ . Curved brackets ( and ) are used surrounding lists of entries, delineated by commas as an alternative method to construct (column) vectors,  $(1, 2) = [1 \ 2]^T$ .

where  $\mathbf{u} \in \mathbb{U}$  is the state variable. The state space  $\mathbb{U} \subset \mathbb{R}^n$  is endowed with the inner-product denoted by  $\langle \cdot, \cdot \rangle_{\mathbb{U}}$  so that the associated norm  $\|\cdot\|_{\mathbb{U}}$  equals twice the kinetic energy of the flow field. The subscript  $\mathbb{U}$  will be omitted unless it is necessary to include.

Associated with the vector-field is the *evolution operator*,  $\mathbf{T}(t) : \mathbb{U} \rightarrow \mathbb{U}$

$$\mathbf{u}(s+t) = \mathbf{T}(t)\mathbf{u}(s) \quad (3)$$

that satisfies (i)  $\mathbf{T}(0) = \mathbf{I}$  and (ii)  $\mathbf{T}(s+t) = \mathbf{T}(s)\mathbf{T}(t)$ . Given a flow field at time  $s$ ,  $\mathbf{T}(t)$  provides the velocity field at a later time  $t+s$  by solving (2) with  $\mathbf{u}(s)$  as initial condition. Our analysis is often based on flow fields sampled at discrete equidistant points in time, where for a fixed  $t = \Delta t$ , (3) is a discrete dynamical system,

$$\mathbf{u}_{k+1} = \mathbf{g}(\mathbf{u}_k), \quad (4)$$

where  $\mathbf{g} = \mathbf{T}(\Delta t)$  and  $k$  is an integer index. Note that, in the context of fluid mechanics,  $\mathbf{g}$  represents a numerical flow solver, which in its simplest form, sets up a grid in space and time and computes approximate solutions on this grid by marching in time.

## 2.2 Linear Global Eigenmodes

We are interested in the behavior of disturbances evolving near the steady-state solution as  $t \rightarrow \infty$ , that is the linear perturbation dynamics after “a short transient period”. For highly unsteady flows, finding a steady solution  $\mathbf{u}_s$ , so that  $\mathbf{f}(\mathbf{u}_s) = 0$  is a formidable task when  $n$  is large. Usually, one has to resort to iterative [103] or filtering [2] techniques. For now, suppose that we have found  $\mathbf{u}_s$ .

To characterize the flow field near  $\mathbf{u}_s$ , let

$$\mathbf{u} = \mathbf{u}_s + \mathbf{u}' \quad (5)$$

with  $\|\mathbf{u}'\| \ll 1$  as a small perturbation. We substitute (5) into (2) and expand in Taylor series around  $\mathbf{u}_s$  to obtain

$$\dot{\mathbf{u}}' = \nabla \mathbf{f}(\mathbf{u}_s) \mathbf{u}' + \mathcal{O}(\|\mathbf{u}'\|^2),$$

where  $\nabla \mathbf{f}(\mathbf{u}_s)$  is the Jacobian  $n \times n$  matrix with the elements as first partial derivative  $\partial \mathbf{f}_i / \partial \mathbf{u}_j$  at  $\mathbf{u}_s$ . Denoting the Jacobian matrix by  $\mathbf{A}$ , omitting the primes and neglecting high-order terms, we obtain the linear system,

$$\dot{\mathbf{u}} = \mathbf{A}\mathbf{u}. \quad (6)$$

The matrix  $\mathbf{A}$  can be regarded as the discretized and linearized Navier–Stokes equations, and could also be obtained by substituting (5) directly into the PDE (1a)–(1b), neglecting nonlinear terms and then discretizing the spatial domain  $\Omega$ .

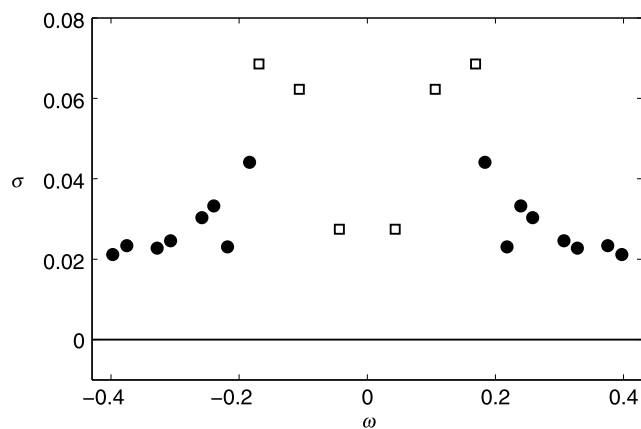


**Fig. 10** The linear spectrum of the jet in crossflow at  $R = 3$ . The eigenvalues marked with *open squares* correspond to anti-symmetric eigenmodes, whereas *black circles* correspond to symmetric eigenmodes

The *linear global eigenmodes* are defined as the eigenvectors and eigenvalues of  $\mathbf{A}$ ,

$$\mathbf{A}\boldsymbol{\phi}_j = \lambda_j \boldsymbol{\phi}_j, \quad j = 1, \dots, n, \quad (7)$$

where  $\boldsymbol{\phi}_j \in \mathbb{U}$  are complex valued and

$$\lambda_j = \sigma_j + i\omega_j. \quad (8)$$

The modes form a basis, in which any perturbation  $\mathbf{u}$  can be expanded as follows

$$\mathbf{u}(t) = \sum_{j=1}^n a_j \boldsymbol{\phi}_j e^{\lambda_j t},$$

where  $a_j$  are the scalar expansion coefficients. From the above expression and (8), it is clear that if  $\sigma_j > 0$  for any  $j$ , the corresponding mode  $\boldsymbol{\phi}_j$  will grow in time, regardless of the behavior of other modes, and the steady flow (or “base-flow”) is rendered unstable. Conversely if  $\sigma_j < 0$  for all  $j$  the steady flow is stable, since any perturbation for long times will decay in time. If there exists  $\sigma_j = 0$ , the stability of  $\mathbf{u}_s$  cannot be determined by linearization and one has to resort to other methods [33]. The frequency at which the eigenmode  $\boldsymbol{\phi}_j$  pulsates is given by  $\omega_j$ .

### 2.2.1 Linear Global Eigenmodes of the Jet in Crossflow

In this section, the linear stability analysis of the steady solution (discussed in Sect. 1.2.1) of the jet in crossflow is presented. The steady solution is obtained using the selective frequency damping (SFD) approach introduced by [2]. The linear global eigenmodes of JCF are fully three-dimensional ( $n \approx 10^7$ ), and must be computed using iterative algorithms (such as the Arnoldi method) described in Sect. 4.1. From the linear spectrum shown in Fig. 10 it is clear that  $\sigma_j > 0$

**Table 1** Properties of three global eigenmodes

Mode	Local mechanism	Symmetry	Location
A	Elliptic instability	Anti-symmetric	Jet & wake region
B	Kelvin-Helmholtz instability	Symmetric	Jet region
C	von Kármán instability	Anti-symmetric	Wall region

for all the leading modes, rendering the steady solution strongly unstable for the chosen parameters (velocity ratio,  $R = V_{\text{jet}}/U_\infty = 3$ ). The Strouhal number, defined as  $\text{St} = fD/V_{\text{jet}}$  ( $D$  is the jet diameter), of the unstable modes are in the range  $[0.04, 0.17]$ , and none of the frequencies of the linear modes match the nonlinear shedding frequencies observed in the numerical simulations. Recall from Sect. 1.2.2, that one separation region just downstream of the jet orifice was observed to oscillate in two directions, slowly in the spanwise direction with  $\text{St}_1 = 0.017$  and rapidly along the jet trajectory with  $\text{St}_2 = 0.14$ . However, the stability analysis merely accounts for the linear dynamics in the neighborhood of the steady solution, where the Strouhal numbers can be considerably different from the saturated dynamics near the attractor (also indicated by Fig. 9). The eigenvalues in Fig. 10 marked by black circles are symmetric, where the symmetry refers to the  $u$  and  $v$  component with respect to the  $z = 0$  axis, i.e.

$$\begin{aligned} &(u(x, y, z), v(x, y, z), w(x, y, z)) \\ &= (u(x, y, -z), v(x, y, -z), -w(x, y, -z)) \end{aligned}$$

The modes marked with open squares display opposite symmetry properties.

The global modes provide a remarkable insight into the underlying growth mechanisms present in the flow. We will focus on three global modes, listed in Table 1, each associated with one global spatial structure and one local physical instability mechanism.

**Mode A—Elliptic Instability** The most unstable mode ( $\boldsymbol{\phi}_1$ ), shown in Fig. 11(a) is an anti-symmetric mode. The instability extends spatially in all three regions discussed in Sect. 1.2 (see also [12, 88]); in the jet region it takes the form of a wavepacket located on and around the CVP; in the wake region it is associated with the upright vortices; and finally the mode has a small amplitude in the wall region. The various vortex systems are thus coupled and in a linear approximation grow with the same rate and oscillate with the same frequency, illustrating the global character of the flow.

This instability has the strongest direct effect on the CVP; the two vortex tubes of the CVP are modified by a sinuous in-phase wavy oscillation in top view ( $xz$ -plane) and an out of phase oscillation in side view ( $xy$ -plane). Moreover, the

wavelength of the instability is of the same order as the diameter of the vortex cores of the CVP. These observations are the traits of a short-wavelength instability of a vortex pair as observed by the experiments of [59] and the numerical simulations of [55]. Such an instability is due to a resonance between two waves of one vortex and the straining field induced by the other vortex. In Fig. 12 the streamwise vorticity component in a cross plane ( $yz$ -plane) far downstream is shown for the baseflow and the most unstable global mode.

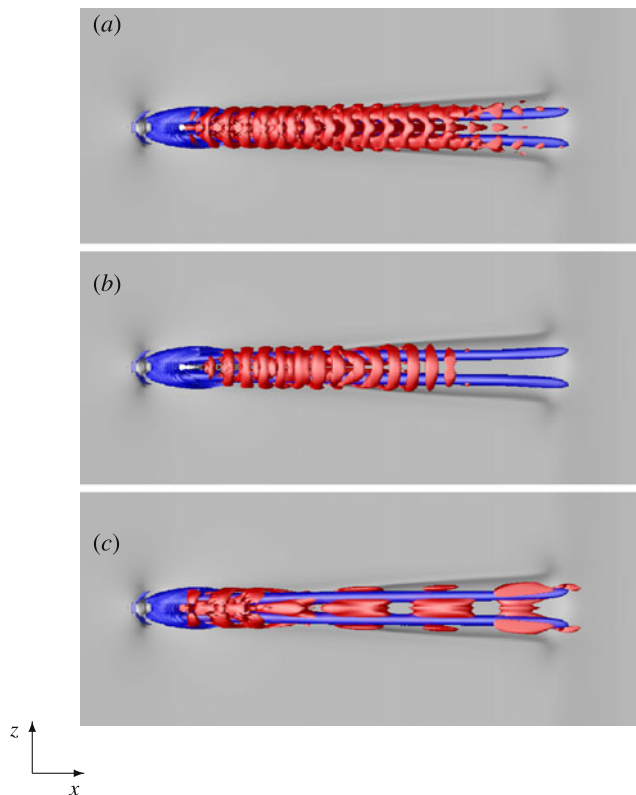
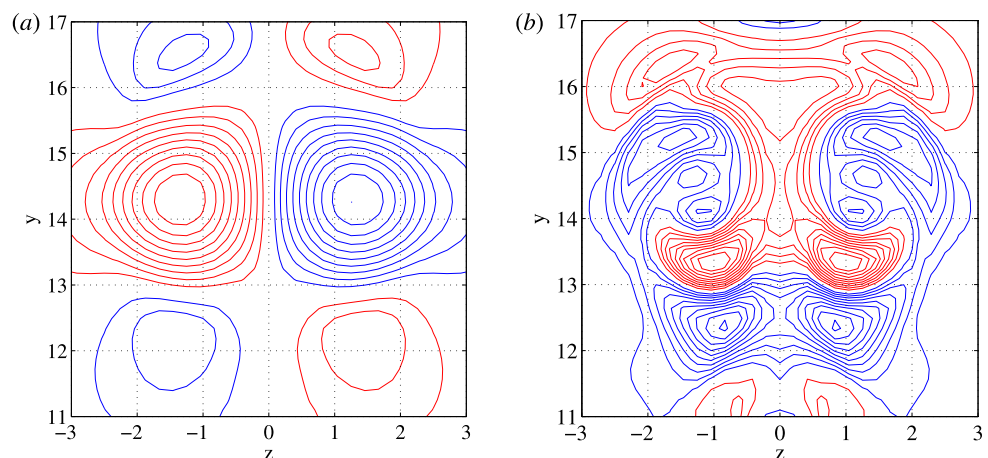


**Fig. 11** Linear global eigenmodes A, B and C of the jet in crossflow shown from top view. The red contour levels represent the  $\lambda_2$  criterion, whereas the baseflow is shown in blue ( $\lambda_2$ ) and gray ( $u$ ). The modes are complex and shown at one phase only (Color figure online)

**Fig. 12** Streamwise vorticity at  $x = 40$  for the steady baseflow (a) and mode A (b). Contour levels are  $0.1, 0.2, \dots, 1.0 \cdot \omega_{x,\max}$ , red is positive, blue negative. Only a portion of the  $zy$ -plane is shown (Color figure online)



The CVP centered around  $y = 14$  can clearly be seen in Fig. 12(a). The global mode (Fig. 12(b)) shows a characteristic two-lobe structure in each CVP vortex. This is remarkably similar to the vorticity computed analytically for the elliptic instability [105, Fig. 2] and the short-wave instability [59, Fig. 10].

**Mode B—Kelvin–Helmholtz Instability** The most unstable symmetric mode is shown in Fig. 11(b). The global mode consists of a symmetric spanwise oriented row of vortex loops that wrap around the upper part of the CVP. They are gradually stretched, and develop “legs” that align with the direction of CVP tubes. In Fig. 13 the spanwise vorticity of the steady flow and mode B is compared at the center  $xy$ -plane ( $z = 0$ ). The baseflow shows a shear layer, which is due to the cylindrical vortex sheet emerging from the jet nozzle and its interaction with the crossflow. The effect of the global instability (Fig. 13(b)) on the shear layer is a periodic deformation of the shear layer, which results in a redistribution of the vorticity in an alternating manner. Such a perturbation of a shear layer is unstable and is referred to as the Kelvin–Helmholtz instability. More generally, when two streams of different velocities come into contact, a vortex sheet develops which is unstable to infinitesimal periodic perturbations (see [15], p. 511 for an elementary stability analysis of the vortex sheet). Mode B modifies the CVP in a varicose fashion viewed from top ( $xz$ -plane). The nonlinear simulation discussed in Sect. 1.2.1 (see Fig. 6(b)), shows how mode B grows in amplitude and develops the characteristic “arches”. This type of symmetric structures has been observed in many experimental studies (see e.g. [50, 61]).

**Mode C—von Kármán Instability** Mode C shown in Fig. 11(c), is an anti-symmetric mode that oscillates with the frequency  $St = 0.043$ . Its global structure is mostly concentrated close to the wall, although it has a small amplitude along the CVP. In particular, the structure near the wall is considerably different compared to the other modes. The

**Fig. 13** Spanwise vorticity at  $z = 0$  for the steady baseflow (a) and the mode B (b). Contour levels are 0.1, 0.2, ...,  $1.0 \cdot \omega_{z,\max}$ , red is positive, blue negative. Only a portion of the  $xy$ -plane is shown

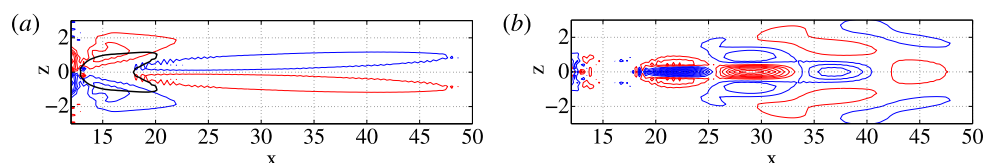
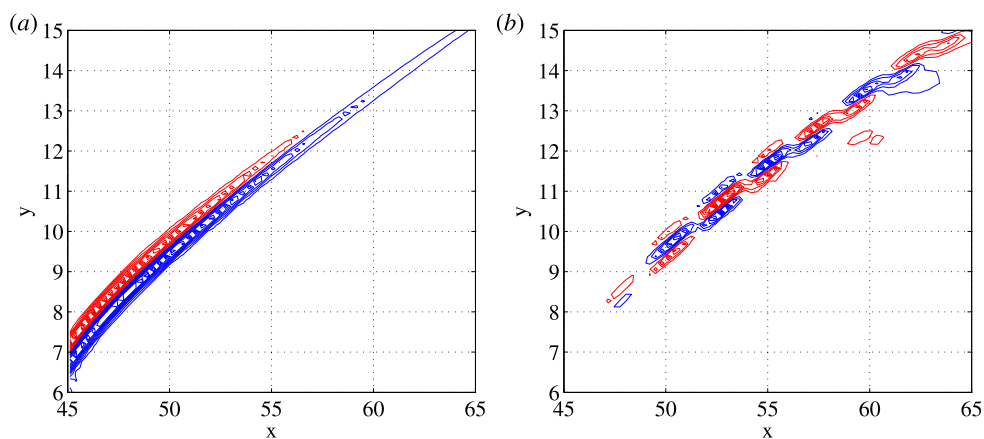


**Fig. 14** Wall-normal vorticity at  $y = 1$  for the steady baseflow (a) and mode C (b). Contour levels are 0.1, 0.2, ...,  $1.0 \cdot \omega_{y,\max}$ , red is positive, blue negative. Inside the region marked by solid black line

there is a backflow. The small-scale wiggles are numerical artifacts. Only a portion of the  $xz$ -plane is shown

wall-normal vorticity of mode C and the steady flow is compared in Fig. 14. In Fig. 14(a) the black contour marks the region of reversed flow ( $u = 0$ ) in the wall region downstream of the jet orifice. On each side of the recirculation zone, two lobes of positive and negative wall-normal vorticity are observed. This is strikingly similar to the unstable steady solution computed for the wake behind a circular cylinder [13, Fig. 1]. Moreover, the global mode shown in Fig. 14(b) shows alternating positive and negative wall-normal vorticity, which is almost identical to the first global mode of the cylinder wake [13, Fig. 3]. It thus seems that although, the jet is a “soft” body and there exists a rigid flat wall, the vortex street of von Kármán is present. One can compare the low frequency oscillation of the separation bubble in the spanwise direction with  $St_1 = 0.017$ , with the Strouhal number of the von Kármán vortex street behind a solid cylinder. For a cylinder wake, the relevant Strouhal number is defined as  $St_c = fD/U$  with  $U$  being the uniform flow velocity in the far field. Adapting the present definition of the frequency based on the jet velocity gives  $St_c = St_1(V_{\text{jet}}/U_\infty)(U_\infty/U)$ . Assuming  $U/U_\infty \approx 1/3$  due to the reduced streamwise velocity in the proximity of the wall gives  $St_c \approx 9St_1 = 0.153$ , which is close to the cylinder wake frequency in the supercritical range ( $Re = 50\text{--}100$  is approximately  $St_c = 0.13\text{--}0.16$ ). It should be mentioned that mode A, which is associated with the elliptic instability in the jet region, also contains the von Kármán instability near the wall, although not as dominant and distinct as mode C.

*Relation to the Separated Region* Global modes do not directly identify the mechanisms that initially generate a disturbance, i.e. rather than the source of the instability, the consequences of the instability are identified. It has therefore been difficult to establish a rigorous connection between unstable linear global eigenmodes and separated regions in the flow, although there is some evidence [36, 78] and an increasingly number of investigations [5, 14, 100] that couple them. Instead, local stability concepts based on the notions of absolute and convective instabilities applied to weakly non-parallel flows have been useful in this context. It is shown that spatially developing flows with self-sustained oscillatory behavior have localized regions in the flow that act as oscillators and localized regions in the flow that act as amplifiers (see [42], for a review). Observations and analysis indicate that sufficiently large separated regions act as oscillators and various co-flowing shear layers act as amplifiers. Although not rigorously investigated in this paper, it is likely that for the jet in crossflow an oscillator—the separated region downstream of the orifice—periodically sheds patches of vorticity, which are convected into the jet, wake and wall regions and amplified due to different *local* mechanisms (such as Kelvin-Helmholtz or short-wave elliptic instability).

### 2.3 Koopman Modes

When global instabilities saturate after a transient phase, a global mode analysis of the fully nonlinear flow has to be

undertaken. Another issue is that, while in numerical simulations and analytical studies the full state  $\mathbf{u}$  can be “observed”, in experiments this is not the case. Usually the velocity is probed—either at a point using hot-wire measurements or at 2D planes using Particle Image Velocimetry (PIV)—or some bulk quantity associated with the flow is measured (such as mass flux, drag, lift). It turns out (see e.g. [73]) that by observations of one or more time signals only, called *observables*, one can characterize the (possibly low-dimensional) behavior of fluid systems (such as chaotic or quasiperiodic attractors, heteroclinic cycles etc.). The important point here is that, monitoring an observable over a very long time interval allows in a statistical sense the reconstruction of the phase space.

An observable is defined as a function  $a(\mathbf{u})$  that associates a scalar to each  $\mathbf{u} \in \mathbb{U}$ . Define the *Koopman*<sup>4</sup> operator  $U : L^2(\mathbb{U}) \rightarrow L^2(\mathbb{U})$  [53], with respect to  $\mathbf{g}$ , as the operator that steps forward the observable, i.e.

$$Ua(\mathbf{u}) = a(\mathbf{g}(\mathbf{u})). \quad (9)$$

Comparing (9) with (4), we observe that whereas the finite-dimensional and nonlinear operator  $\mathbf{g}$  steps forward the state, the Koopman operator is infinite-dimensional and it steps forward an observable. The operator is linear since for  $a, b \in L^2(\mathbb{U})$ ,

$$\begin{aligned} U(\alpha a(\mathbf{u}) + \beta b(\mathbf{u})) &= \alpha a(\mathbf{g}(\mathbf{u})) + \beta b(\mathbf{g}(\mathbf{u})) \\ &= \alpha Ua(\mathbf{u}) + \beta Ub(\mathbf{u}). \end{aligned}$$

We can study certain properties of the trajectory of the nonlinear flow  $\mathbf{g}$  by the spectral properties of linear operator  $U$ . Let therefore,  $\varphi_j : \mathbb{U} \rightarrow \mathbb{R}$  denote the eigenfunctions and  $\lambda_j \in \mathbb{C}$  denote the eigenvalues<sup>5</sup> of the Koopman operator,

$$U\varphi_j(\mathbf{u}) = \lambda_j\varphi_j(\mathbf{u}), \quad j = 0, 1, 2, \dots$$

<sup>4</sup>The analysis requires some measure theory, but here we make no attempt to be mathematically precise and refer to [56] for rigorous treatment on the subject. Most importantly, we need to introduce an *invariant measure*, essentially meaning that we can find a measure  $\mu$  such that the value of a integral,

$$\int_{\mathbb{U}} a(\mathbf{u})d\mu = \int_{\mathbb{U}} a(\mathbf{g}(\mathbf{u}))d\mu.$$

is invariant. Henceforth we drop  $\mu$  and use the notation  $d\mu = d\mathbf{u}$ . Such a measure can always be found [56] if  $\mathbf{g}$  satisfies certain properties (that  $\mathbf{g}$  is a measure-preserving operator). Observables are thus elements in the space

$$L^2(\mathbb{U}) = \left\{ a : \mathbb{U} \rightarrow \mathbb{R} \mid \int_{\mathbb{U}} |a|^2 d\mathbf{u} < \infty \right\}.$$

<sup>5</sup>Here, we consider only the point spectrum of  $U$ , see [65] for the continuous spectrum.

It can be shown (e.g. [23]) that as  $t \rightarrow \infty$ ,  $U$  is a unitary operator and therefore the sequence of its eigenfunctions  $\{\varphi_j\}_{j=0}^{\infty}$  forms an orthonormal expansion basis.

We proceed with defining the global modes that are referred to as Koopman modes, by first introducing a vector-valued observable  $\mathbf{a}(\mathbf{u}) : \mathbb{U} \rightarrow \mathbb{R}^P$ . For example, the scalar observable  $a(\mathbf{u})$  can be considered as an observation of a velocity component at a single coordinate in  $\Omega$  (obtained via hot-wire measurements) and  $\mathbf{a}(\mathbf{u})$  can be considered as a velocity measurement in a plane in  $\Omega$  (obtained via PIV). Consider a long time series of the observable  $\mathbf{a}$  on the trajectory of the system  $\mathbf{g}$  starting at the initial condition  $\mathbf{u}_0$ ,

$$\mathbf{X} = [\mathbf{a}(\mathbf{u}_0) \quad \mathbf{a}(\mathbf{u}_1) \quad \mathbf{a}(\mathbf{u}_2) \quad \dots]. \quad (10)$$

Next, assuming that each of the components of  $\mathbf{a}(\mathbf{u}_0)$  lies within the span of  $\{\varphi_j\}_0^{\infty}$  (see [65] for the general case), an orthogonal projection of  $\mathbf{a}(\mathbf{u}_0)$  onto the space spanned by the Koopman eigenfunctions yields,

$$\mathbf{a}(\mathbf{u}_0) = \sum_{j=0}^{\infty} \boldsymbol{\phi}_j \varphi_j(\mathbf{u}_0)$$

where the vector-valued expansion coefficient  $\boldsymbol{\phi}_j \in \mathbb{R}^P$ , given by

$$\boldsymbol{\phi}_j = \langle \mathbf{a}(\mathbf{u}_0), \varphi_j(\mathbf{u}_0) \rangle_{L^2(\mathbb{U})} = \int_{\mathbb{U}} \mathbf{a}(\mathbf{u}_0) \varphi_j^*(\mathbf{u}_0) d\mathbf{u}_0 \quad (11)$$

is defined as the  $j$ th *Koopman mode* under the map  $\mathbf{g}$ . Note that in numerical simulations, where the entire flow field is observable  $\mathbf{a}(\mathbf{u}) = \mathbf{u}$ , the Koopman modes are fully global,  $\boldsymbol{\phi}_j \in \mathbb{U}$ . The Koopman modes and eigenfunctions are determined only for the first sample in (10) and the remaining samples on the trajectory can be expressed entirely in terms of these. To see this, note that the  $k$ th sample in the series (10) is given by,

$$\mathbf{a}(\mathbf{u}_k) = U^k \mathbf{a}(\mathbf{u}_0) = U^k \left( \sum_{j=0}^{\infty} \varphi_j(\mathbf{u}_0) \boldsymbol{\phi}_j \right) = \sum_{j=0}^{\infty} \lambda_j^k \varphi_j(\mathbf{u}_0) \boldsymbol{\phi}_j.$$

We expand the entire sequence (10) in Koopman eigenfunctions and write it in matrix form

$$\mathbf{X} = \boldsymbol{\Phi} \mathbf{S}, \quad (12)$$

where the columns of  $\boldsymbol{\Phi}$  contain the Koopman modes and the corresponding Koopman eigenfunctions,

$$\boldsymbol{\Phi} = [\varphi_0(\mathbf{u}_0)\boldsymbol{\phi}_0 \quad \varphi_1(\mathbf{u}_0)\boldsymbol{\phi}_1 \quad \varphi_2(\mathbf{u}_0)\boldsymbol{\phi}_2 \quad \dots]$$

and  $\mathbf{S}$  is the infinite Vandermonde matrix

$$\mathbf{S} = \begin{bmatrix} 1 & \lambda_0 & \lambda_0^2 & \dots \\ 1 & \lambda_1 & \lambda_1^2 & \dots \\ \vdots & \vdots & \vdots & \ddots \end{bmatrix}. \quad (13)$$

Note that the first eigenfunction of  $U$ , corresponding to the eigenvalue  $\lambda_0 = 1$ , is related to the time average of a sequence  $\mathbf{X}$ ,

$$\varphi_0(\mathbf{u}) = \lim_{n \rightarrow \infty} \frac{1}{n} \sum_{j=0}^{n-1} a(\mathbf{u}_j). \quad (14)$$

This can be easily seen, since the average  $\varphi_0$  is constant on the orbit  $\mathbf{g}(\mathbf{u})$ ,

$$\varphi_0(\mathbf{u}) = \varphi_0(\mathbf{g}(\mathbf{u})) = U\varphi_0(\mathbf{u}).$$

The sequence of observables obtained from  $\mathbf{g}$  starting with  $\mathbf{u}_0$ , can thus be decomposed into spatial structures (Koopman modes) whose temporal behavior is given by the associated Koopman eigenvalue, i.e. the phase  $\arg(\lambda_j)$  determines its frequency, and the magnitude  $|\lambda_j|$  determines the growth rate of mode  $\phi_j$ . The Koopman eigenfunctions  $\varphi_j$ , on the other hand, associate with each Koopman mode  $\phi_j$  an amplitude, which determines the significance of that mode. As explained in [66] and [65], by investigating a large number of trajectories (starting from different  $\mathbf{u}_0$ ), the state space can be partitioned into level sets of constant  $\varphi_j$ , i.e. one can identify regions in  $\mathbb{U}$  that oscillate with a single frequency only and the value  $\varphi_j$  determines how significant that frequency is in the flow. For complex flows, after a transient regime, the flow evolves near some attracting set in  $\mathbb{U}$ , which might show very complicated behavior such as strange attractors or simple behavior, such as periodic orbits. In this limit there exists a countable set of nonzero eigenvalues  $\lambda_j$  that all are on the unit circle,  $|\lambda_j| = 1$  for all  $j$ . This means that each eigenfunction  $\varphi_j$  is associated with a temporal frequency  $\omega_j$  (the phase of  $\lambda_j$ ) only since the growth rate is zero for all modes.

The Koopman modes can in principle be determined by solving the integral (11). However, this is too expensive, since every possible initial condition has to be considered. Alternatively, one can use *harmonic averages* as described by [65] or by finding the inverse of the truncated Vandermonde matrix, i.e.  $\Phi = \mathbf{X}_r \mathbf{S}^{-1}$ , as shown in Sect. 4.2.

### 2.3.1 Other Approaches

It has somewhat “accidentally” been noticed that a linear stability analysis using the time-average mean flow, instead of a truly steady flow, provides modes whose discrete frequencies are in good agreement with the global nonlinear shedding frequency. As a consequence a number of linear stability studies (see e.g. [13, 78, 101], and references therein) have recently been conducted in order to identify coherent structures that can be associated with vortex shedding. Although the averaged mean flow takes into account some of the nonlinear effects implicitly, such analysis is “ad-hoc” and lacks rigorous foundation. In fact, it was shown

[93] that such an analysis works only for some specific cases, such as the circular cylinder.

Proper orthogonal decomposition (POD) is a method to extract information from large datasets, either obtained from numerical simulations or experiments. The method was introduced by [62] for fluid systems for extracting coherent structures in turbulent flows. The POD modes identify those parts of the phase space which contain the most kinetic energy, typically attractors in phase space [40]. It is likely that the structures are a result of the vortex shedding. Unfortunately, the POD method averages in time and the correlation in time is completely lost, rendering the task of pinning down one structure to one frequency difficult.

### 2.3.2 Koopman Modes of the Jet in Crossflow

A long sequence of flow-field snapshots are collected from direct numerical simulations (DNS) of the jet in crossflow. The transient time from the unstable fixed point to the attractor is not sampled, i.e. only the asymptotic motion in phase space is considered. The eigenvalues  $\lambda_j$ , eigenfunctions  $\varphi_j$  and the global modes  $\phi_j$  associated with the Koopman operator of the sequence are computed using the DMD algorithm described in Sect. 4.2. The time-discrete spectrum and the time-continuous spectrum of the Koopman operator are shown in Fig. 15. The two spectra are related to each other via a linear transformation (see Sect. 4.1). From the time-discrete (Fig. 15(a)) we can observe that nearly all the eigenvalues lie on or very close to the unit circle. Note that as  $t \rightarrow \infty$  all the eigenvalues will lie exactly on the unit circle since the Koopman operator is unitary. The time-continuous spectrum (Fig. 15(b)) confirms that all eigenvalues are marginally stable and therefore one cannot expect any flow structures growing or decaying exponentially in the nonlinear flow.

The Koopman mode corresponding to the Koopman eigenvalue  $\lambda_0$  is the time-averaged flow and is depicted with blue symbol in Fig. 15. The other (unsteady) Koopman eigenvalues vary smoothly in color from red to white, depending on the magnitude (Koopman eigenfunctions)  $\varphi_j$  of the corresponding Koopman mode. The magnitudes of the modes are shown in Fig. 16(a) with the same coloring as the spectrum, where a few (10–14) leading modes are observed to have significantly larger values, as the magnitudes rapidly decay and gradually level out. In Fig. 16(b) each mode is displayed with a vertical line scaled with its magnitude at its corresponding Strouhal number. Only the  $\omega_j \geq 0$  are shown, since the eigenvalues come in complex conjugate pairs. Ordering the modes with respect to their magnitude, the first (1–2) and second (3–4) pair of modes oscillate with  $St_2 = 0.141$  and  $St_4 = 0.136$  respectively, whereas the third pair of modes (5–6) oscillate with  $St_6 = 0.017$ . All linear combinations of the frequencies excite higher modes, for instance, the nonlinear interaction of the first and third pair

**Fig. 15** Time-discrete (a) and time-continuous (b) Koopman spectra of the JCF. The Koopman eigenvalue  $\lambda_0$  is shown with a blue symbol, while the other eigenvalues vary smoothly in color from red (high magnitudes) to white, depending on the magnitude  $\varphi_j$  of the corresponding Koopman mode (Color figure online)

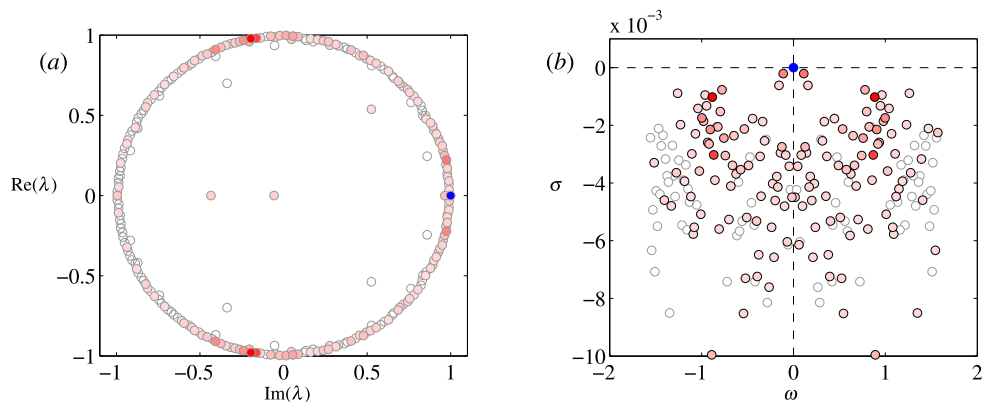


**Fig. 16** Left figure: The magnitudes  $\varphi_j$  associated with the Koopman modes  $j = 1, \dots, 40$ . Right figure: The magnitudes  $\varphi_j$  are plotted as a function of the Strouhal number  $St_j$

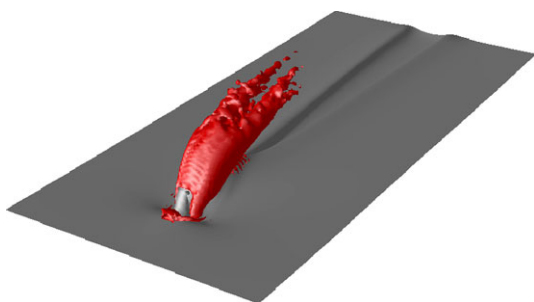
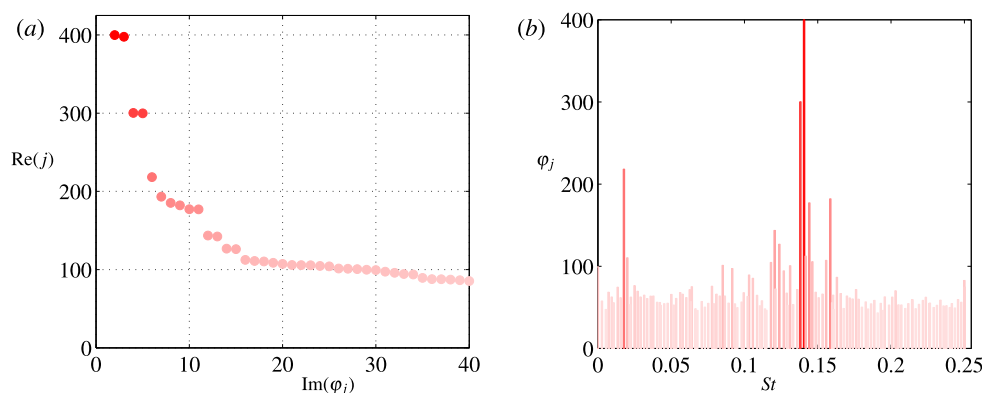


**Fig. 17** The zeroth Koopman mode (time-averaged mean flow) is shown with red contour levels depicting the  $\lambda_2$ -criterion and gray contour level show the  $u$  component (Color figure online)

results in the fourth pair, i.e.  $St_8 = 0.157$  and so on. Therefore, the spectral properties of the Koopman operator for the jet in crossflow, suggest that the attractor dynamics is dominated by a few discrete distinct frequencies. The associated Koopman modes are considered next, where each global mode identifies a region where the flow oscillates with its corresponding frequency.

The zeroth Koopman mode  $\phi_0$  (shown in Fig. 17) is the time-averaged mean flow, corresponding to the eigenvalue marked with a blue symbol in the spectrum. A common feature of unsteady flows with separated regions is a large difference between the steady solution and the time-averaged mean flow solution, which is due to a significant transient

time from the fixed point to the attractor. The difference between the two flows, usually called mean flow distortion (or mean flow correction), quantifies how much the saturated disturbances modify the steady flow, i.e. where the mean flow distortion is large there is significant alteration of the steady solution due to the saturated disturbance. Physically, the mean flow correction is due to the Reynolds stresses generated by the fluctuating field. The most significant change in the flow is due to breakdown of the CVP (possibly attributed to the elliptic instability) resulting in a retardation of the two CVP vortex tubes, whereas the cylindrical vortex sheet, horse-shoe/wall vortices are not modified noticeably. The separated region downstream of the jet orifice is reduced in size (compared to the steady flow), similarly to the observations made by other researchers [13, 71]. The mean flow distortion being confined to the CVP and the separated region near the wall indicates that the saturating fluctuations are large in those locations.

The first pair of unsteady Koopman modes  $\phi_1 - \phi_2$  oscillates with  $St_2 = 0.14$ —which is precisely the fundamental shedding frequency observed in the numerical simulations—and is an anti-symmetric nonlinear wavepacket. The mode (shown in Fig. 18(a)) identifies the regions in the flow domain where the frequency  $St_2 = 0.14$  can be detected. The largest amplitude is along the jet trajectory; the streamwise velocity of opposite sign gives rise to the

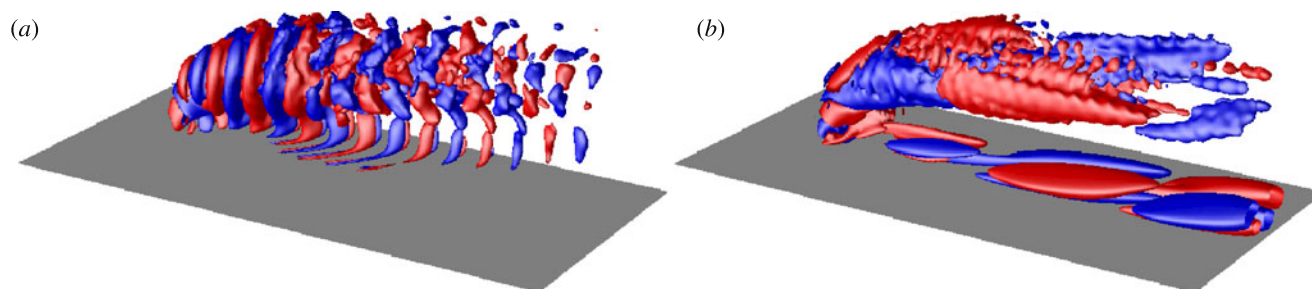


**Fig. 18** The positive (*red*) and negative (*blue*) streamwise velocity component of the first (**a**) and fifth (**b**) Koopman modes. The flat plate is shown in gray (Color figure online)

**Table 2** Comparison of the frequencies (St) obtained from DNS probes (shown in Fig. 7); the global eigenmodes of the linearized Navier–Stokes; POD modes 1 and 6, corresponding to mainly shear-layer and wall oscillations, respectively; and Koopman modes

Mode	DNS	Global	POD	Koopman
Shear layer	0.141	0.169	0.138, 0.158, 0.121	0.141
Wall	0.017	0.043	0.0188, 0.0094, 0.158, 0.121	0.017%

spanwise-oriented vortex loops that gradually break up into smaller vortex filaments in the downstream direction. Similar to the mean flow, most coherence in the spatial structure is located in region where jet fluid and crossflow come into contact; its shape is similar to the “array of transverse secondary vortex pairs” observed in the late nonlinear stages of the short-wave instability as reported by [55] and [59]. This analysis clearly shows that the fundamental shedding frequency of the jet in crossflow is associated with vortex loop structures on the jet, as a result from a saturation of the first global instability mode discussed in the previous section.

The third pair  $\phi_5$ – $\phi_6$  oscillates with precisely the low-frequency vortex shedding,  $St_1 = 0.017$  observed from numerical simulations. This anti-symmetric mode is shown in Fig. 18(b) and is clearly related to coherent structures in the wall region. The alternating positive and negative streamwise velocity near the wall contributes to the wall-normal vorticity constituting the nonlinear von Kármán vortex street. In fact, the structure of the wall-normal vorticity near the wall is similar to the nonlinear wavepacket reported by [78] and [13] for the cylinder wake flow. We conclude that the low-frequency shedding of the jet in crossflow is indeed associated with the von-Kármán vortex street developing near the wall downstream of the jet, resulting from a saturation of the global instability modes. It can be noted that this mode has a nonzero amplitude in the jet region (along the jet body), which is confirmed by the observation that the whole jet wiggles back and forth in the spanwise direction.

### 2.3.3 Concluding Remarks

For complex flows, where several self-sustained oscillations exist and are potentially coupled, one is interested in study-

ing the dynamics of the different oscillations separate from each other. The Koopman modes are able decouple and isolate these dynamics. In Table 2 the frequencies obtained from the analysis based on the Koopman modes and global eigenmodes of the linearized system for the jet in crossflow are shown. For completeness, the frequencies extracted from the Proper Orthogonal Decomposition (POD) modes are also included in the table. The POD modes of the JCF are described in [88]. The global eigenmodes capture the dynamics only in a neighborhood of the unstable fixed point, resulting in linear frequencies that are different from the nonlinear shedding frequencies. The Koopman modes, on the other hand, correctly capture to the asymptotic dynamics on the attractor of the nonlinear system. The method is thus able (by construction) to extract global modes that oscillate with precisely the same frequency as the shedding frequencies. Although, POD modes are also associated with the nonlinear system, they capture the most energetic structures, resulting in modes that contain several frequencies. The coefficient of the first POD mode oscillates mainly with frequency  $St = 0.138$ , which is close to the shear-layer oscillation frequency  $St_2 = 0.141$  observed in DNS. However, the signal contains other frequencies as well, resulting from the interaction of the two fundamental oscillations (shear-layer and wall),  $St = 0.138 \pm 0.017$ , which cause the beating shown in Fig. 19.

### 3 Flow Control Using Balanced Modes

In wall-bounded shear flows, for a given Reynolds number  $Re > Re_c$ , a laminar flow is observed if disturbance amplitudes are below a critical value, whereas a fluctuating tur-

bulent flow is gradually developed for higher amplitudes. As discussed in Sect. 1.1, the aim of transition control is to keep the amplitudes of the incoming perturbations small, in order to avoid turbulence. It thus suffices to focus on the dynamics of small amplitude disturbances near the laminar solution governed by the linear system  $\dot{\mathbf{u}} = \mathbf{A}\mathbf{u}$ . For the flat-plate boundary layer, significant amplification of disturbances  $\mathbf{u}$ —usually several orders of magnitude—takes place before disturbances eventually propagate out of the flow domain and leave behind the steady unperturbed boundary-layer flow. This transient growth of disturbance energy is due to the nonnormality [104] of the stable matrix  $\mathbf{A}$ .

We return to the flat-plate example introduced in Sect. 1, where the emergence of a turbulent spot from a finite-amplitude disturbance was discussed. In Fig. 20 a sketch of flat-plate configuration is shown, where in addition to the disturbances upstream in the boundary layer, one row of sensors and one row of actuators are introduced near the wall. The objective is to use the sensor-actuator system to mini-

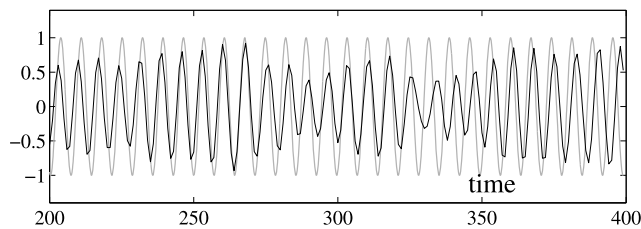


**Fig. 19** Comparison of time coefficients: the projection of the flow field onto the most energetic POD mode (black), and the coefficient of the most energetic Koopman mode (gray)

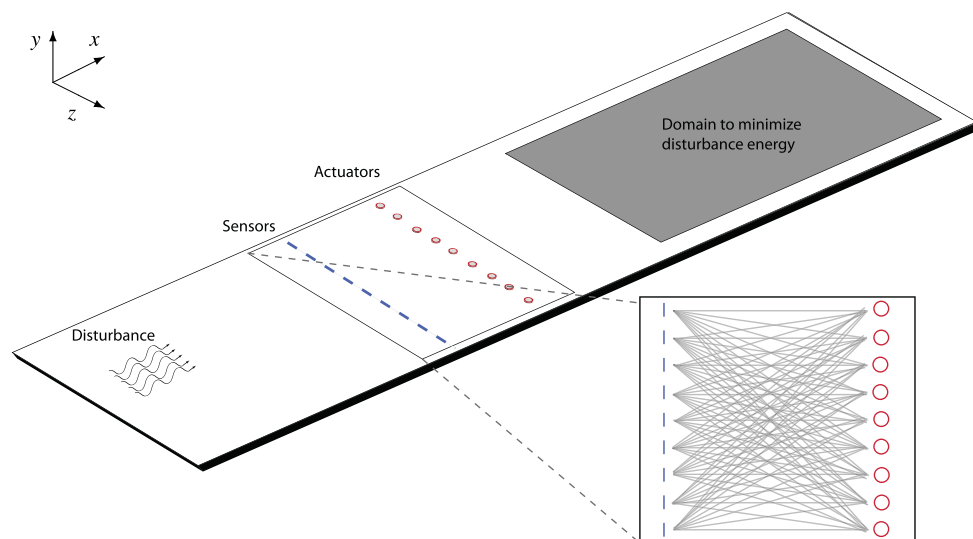


**Fig. 20** Sketch of the input-output configuration. The disturbance is located far upstream inside the boundary layer. Approximately half way in the downstream direction, 9 actuators are modelled by a spanwise row of localized volume forcing. Similarly, the sensor measurements used for estimation consist of a spanwise array of 9 localized

mize the disturbance energy in a domain downstream in the boundary layer. This domain is spanned by a number of prudently chosen (objective) functions. In the present configuration, there are 10 inputs (one disturbance, 9 actuators) and 19 outputs (9 sensors, 10 objective functions). Assuming all inputs and outputs have been modelled appropriately, there are a number of important decisions to be made:

- Given the sensor measurements, how do we determine what action the actuators should take in order to minimize the disturbance energy?
- Should the action of an actuator depend on all sensors measurements or only the sensor located upstream of it?
- How can we model sensor noise or penalize the actuation effort? Are there guarantees that the actuators will not introduce more “dangerous” disturbances in flow?

These issues can be addressed in a systematic way by control theory. In particular, the objective of feedback control is to minimize the effects of external influences on the system behavior when not having a complete knowledge of the disturbances that are present. This indirectly means that a more reliable system (closed-loop system) is designed whose amplifying behavior of disturbances is significantly reduced, and as a consequence less likely to transition to turbulence. In Fig. 21(a) the energy evolution (red solid line) of a infinitesimal-amplitude disturbance clearly demonstrates the transient growth phenomena; we observe an exponential growth of three orders of magnitude until the energy peaks at  $t = 2000$  and then decays rapidly. In the same figure the disturbance energy of the closed-loop system obtained using feedback control is shown with a blue line. We observe

functions (same as actuators) near the wall placed a small distance upstream of the actuators. The inset figure shows the how the sensors are connected to the actuators. Finally, 10 sensors, located further downstream are used to define the objective functional (36). The numerical parameters are given in Table 5 (case 3D-LIN-BL) in Sect. 4.4

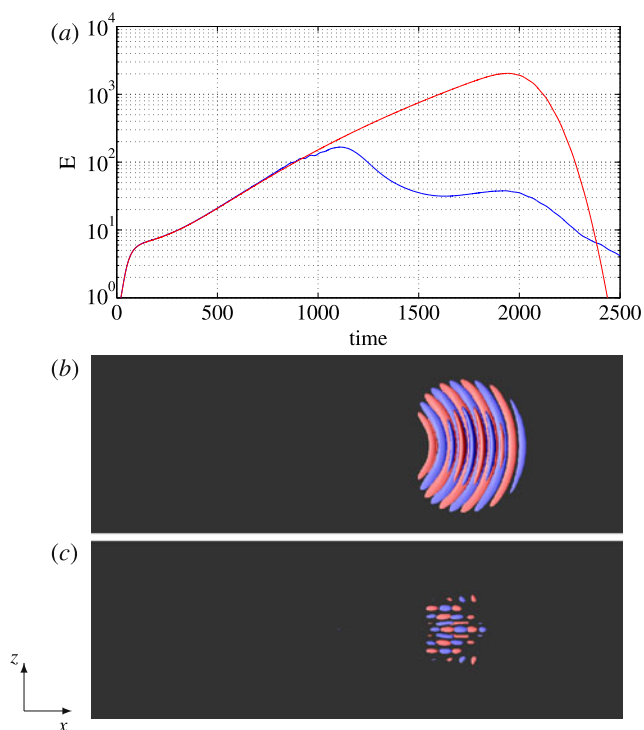


**Fig. 21** (a) Kinetic energy of a three-dimensional disturbance in the flat-plate boundary layer without (*red*) and with feedback control (*blue*). A sketch of the control configuration is given in Fig. 20. Snapshots of the disturbance field at  $t = 1750$  without (b) and with feedback control (c) (Color figure online)

that the peak value of the disturbance energy is considerably smaller (about one order of magnitude) than the original system. Snapshots of disturbances of the two systems at  $t = 1750$  are compared in Fig. 21(b)–(c), where we clearly see that the nearly two-dimensional structure of disturbance of the Navier–Stokes system has been replaced by a smaller scale three-dimensional disturbance in the closed-loop system.

Although optimal and robust feedback control have been used for several centuries to modify dynamics and a rigorous theory has existed for several decades, it is only very recently that it has been used in flow control applications. The main reason is that control theoretical tools have essentially been inaccessible to all but the very simplest fluid systems, due to the high-dimensional system that arise from discretization of the Navier–Stokes equations. Model reduction, where the complex system is approximated with a very low-order system, is therefore an important step in the control design process.

### 3.1 Control Design: an Overview

The main steps of the control design process are outlined in this subsection. Throughout the section, examples on the simpler two-dimensional flat-plate configuration are provided. The three-dimensional configuration can be treated

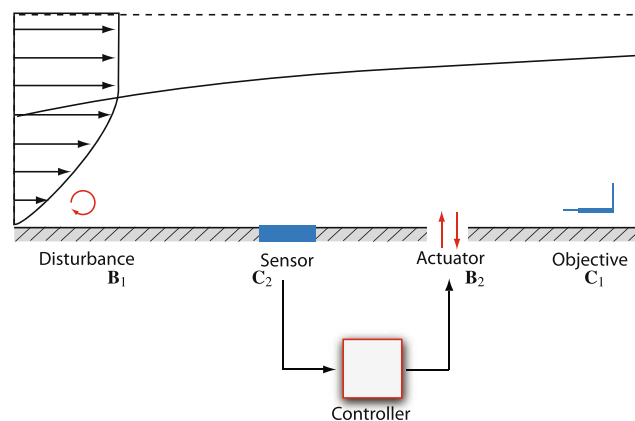


**Fig. 22** A sketch of input-output configuration for the control of perturbations in a two-dimensional flat-plate geometry. The domain size and numerical parameters are listed in Table 5 (case 2D-LIN-BL) in Sect. 4.4

in an analogous manner, although the design requires more care due to the additional direction in the spanwise direction.

A sketch of the configuration for the control of two-dimensional perturbations is shown in Fig. 22. The first input  $\mathbf{B}_1$ , located far upstream, models the initial receptivity phase, where disturbances are induced by free-stream turbulence, acoustic waves or wall roughness. The second input is the actuator,  $\mathbf{B}_2$ , which provides a way to manipulate the flow. Two sensors,  $\mathbf{C}_1$  and  $\mathbf{C}_2$ , are used to provide measurements of the perturbation. The upstream measurements are used to estimate the amplitude and the phase of the incoming perturbations, while the downstream sensor is used to quantify the modification of the flow due to the action of the actuator. The aim is to minimize the kinetic energy of the disturbance in the region defined by  $\mathbf{C}_1$ , using the actuator  $\mathbf{B}_2$  and sensor  $\mathbf{C}_2$ . Of course, the overall goal is to reduce the perturbation growth in the entire flow domain in order to delay the initial phase of the transition process. However, this is achieved by placing  $\mathbf{C}_1$  far downstream: if we demand the disturbance energy to be small at  $\mathbf{C}_1$ , the disturbance amplitude has to decrease significantly before it reaches the objective function to accomplish this task. For the three-dimensional disturbance discussed in the beginning of this section,  $\mathbf{C}_1$  must be chosen with more care to achieve a significant damping of perturbation. The choice of the relative position of the actuator and sensor is based on the knowledge of the behavior of boundary layer instabilities and is described in [10].

The key point is that the signal given to the actuator at each instant in time is based only on the measurement signal provided by the sensor  $\mathbf{C}_2$ . Rather than velocity fields  $\mathbf{u} \in \mathbb{U}$ , we are interested in characterizing time signals and in particular the relation between input signals and output signals, since this relation underlies most of the basic treatments in the control design. We adopt an operator-viewpoint, where the operators represent “systems” that map input signals

**Table 3** Properties of the three systems considered in this paper. See text for additional information

	System	Complexity	2-Norm	$\infty$ -Norm
Plant	$\mathbf{G}$	$10^5$	9.7	144.6
Reduced-order model	$\mathbf{G}_r$	60	9.4	144.3
Closed-loop system	$\mathbf{G}_c$	$10^5$	0.4	6.4

to output signals. In particular, three systems will be used throughout this section, each of them related to one major step in the control design:

1. The characterization of the input-output behavior of the plant (open-loop system)  $\mathbf{G}$ , represented by the linearized Navier–Stokes equations including two-dimensional disturbances, actuators, sensors and objective functions. In Sect. 3.2 the input-output behavior between signals is evaluated by computing system norms (2-norm and  $\infty$ -norm).
2. Section 3.3 describes a method to construct a low-dimensional model  $\mathbf{G}_r$  that essentially shows the same input-output behavior as the plant  $\mathbf{G}$ .
3. The final step is taken in Sect. 3.4, using  $\mathbf{G}_r$ , the closed-loop system  $\mathbf{G}_c$  is designed such that its norms—thus its amplifying behavior of disturbances—are small compared to the plant  $\mathbf{G}$ .

The three systems and their properties are listed in Table 3.

### 3.2 Linear Systems and Input-Output Signals

In order to characterize the input-output behavior of a linear system we first need to define systems and signals. We begin with defining a *linear state-space system* as

$$\dot{\mathbf{u}} = \mathbf{A}\mathbf{u} + \mathbf{B}\mathbf{w} \quad (15a)$$

$$\mathbf{y} = \mathbf{C}\mathbf{u} + \mathbf{D}\mathbf{w} \quad (15b)$$

where  $\mathbf{u} \in \mathbb{U}$  is the state variable,  $\mathbf{w} \in \mathbb{R}^m$  is the input and  $\mathbf{y} \in \mathbb{R}^p$  is the output of the system. The input space and output space are endowed with the Euclidean norm denoted by  $|\cdot|$ . The matrices  $\mathbf{A} \in \mathbb{R}^{n \times n}$ ,  $\mathbf{B} \in \mathbb{R}^{n \times m}$  and  $\mathbf{C} \in \mathbb{R}^{p \times n}$  are constant and the latter two matrices are usually low-rank, i.e.  $m, p \ll n$ . We assume (15a)–(15b) is stable, meaning that all the eigenvalues of  $\mathbf{A}$  have negative real part. Since it does not affect the results, assume for now that both the initial condition  $\mathbf{u}_0$  and the feed-through term  $\mathbf{D} \in \mathbb{R}^{p \times m}$  are zero.

A *signal* is a (vector-valued) function of the independent variable time only, and is an element of the function space

$$L^2_s(t_1, t_2) = \left\{ \mathbf{z}(t) : \mathbb{R} \rightarrow \mathbb{R}^s \mid \int_{t_1}^{t_2} |\mathbf{z}|^2 \leq \infty \right\},$$

where  $s = m$  for the input space  $s = p$  for the output space (subscript will omitted in most cases). Often we will consider signals over the infinite time intervals  $L^2(-\infty, \infty)$ ,  $L^2(0, \infty)$  and  $L^2(-\infty, 0)$ , which physically can be obtained after the transients asymptotically die out (owing to stability). The time-domain space  $L^2(-\infty, \infty)$  can be represented by a frequency-domain space  $\hat{L}^2(i\mathbb{R})$  by means of a Fourier transform, which preserves the inner-product (Parseval's theorem), i.e.

$$\|\mathbf{z}\|_{L^2} = \|\hat{\mathbf{z}}\|_{\hat{L}^2}.$$

Therefore we will not make notational distinction between time-domain signals and their frequency-domain counterparts.

A *system* is a linear mapping between an input signal to an output signal,  $\mathbf{G} : L^2 \rightarrow L^2$

$$\mathbf{y}(t) = (\mathbf{G}\mathbf{w})(t).$$

We are interested in the asymptotic and causal input-output properties; assuming knowledge of  $\mathbf{w}(t)$  in the time interval  $(-\infty, t)$ , the output at time  $t$  is uniquely given by the system  $\mathbf{G} : L^2(-\infty, \infty) \rightarrow L^2(-\infty, \infty)$

$$\mathbf{y}(t) = (\mathbf{G}\mathbf{w})(t) = \mathbf{C} \int_{-\infty}^t e^{\mathbf{A}(t-s)} \mathbf{B}\mathbf{w}(s) ds \quad (16)$$

where  $\exp(\mathbf{A})$  is the matrix exponential [104]. Similar to signals, linear time-invariant (LTI) systems can be represented in the frequency domain. A Laplace transform of (16) results in a transfer function matrix

$$\mathbf{y}(s) = \hat{\mathbf{G}}(s)\mathbf{w}(s) = (\mathbf{C}(s\mathbf{I} - \mathbf{A})^{-1}\mathbf{B})\mathbf{w}(s) \quad (17)$$

with  $s \in \mathbb{C}$ . Henceforth the hat on  $\hat{\mathbf{G}}$  is omitted since it is related to  $\mathbf{G}$  by a linear transformation. Occasionally we write the input-output system in compact form

$$\mathbf{G} = \begin{pmatrix} \mathbf{A} & \mathbf{B} \\ \mathbf{C} & \mathbf{D} \end{pmatrix}. \quad (18)$$

Performance criteria for control design and error bounds for model reduction are given by different system norms. In general,  $\|\mathbf{G}\|_2$  is an appropriate measure of performance when the input signal is a stochastic process, whereas  $\|\mathbf{G}\|_\infty$  is appropriate when considering largest possible amplification due to an input signal. The latter norm quantifies the amplification of an input signal, which is given by the induced  $L^2$ -norm of a system,

$$\|\mathbf{G}\|_\infty = \sup_{\mathbf{w} \neq 0} \frac{\|\mathbf{G}\mathbf{w}\|_{L^2}}{\|\mathbf{w}\|_{L^2}}.$$

It can be shown (see e.g. [31], p. 92) that the induced norm is the infinity norm of its transfer function matrix,

$$\|\mathbf{G}\|_\infty = \sup_{\omega} |\mathbf{G}(i\omega)|, \quad (19)$$

where  $|\mathbf{G}|$  denotes the largest singular value of the transfer function matrix. Moreover, this norm is finite for all stable systems. So,  $\|\mathbf{G}\|_\infty$  measures how much energy is transferred from the input to the output.

The 2-norm of system  $\mathbf{G}$  is the expected root-mean-square (RMS) value of the output when the input is a white noise process with unit variance. If  $\mathbf{w}(t)$  is white noise, then

$$\|\mathbf{G}\|_2^2 = E\left(\frac{1}{T}\|\mathbf{G}\mathbf{w}\|_{L^2}^2\right) = E\left(\frac{1}{T}\int_0^T |y|^2 dt\right) \quad (20)$$

where it can be shown (see e.g. [31], p. 94) that as  $t \rightarrow \infty$

$$\|\mathbf{G}\|_2^2 = \frac{1}{2\pi} \int_{-\infty}^{\infty} \text{trace}(\mathbf{G}(i\omega)\mathbf{G}^T(i\omega))d\omega. \quad (21)$$

The 2-norm can be computed either by the average output energy of a large number of realizations to stochastic forcing, or by solving one Lyapunov equation [31]. However, when  $n$  is large, as in our case, a more feasible way is to compute the output energy of an impulse response, since white noise is a set of impulses that are uncorrelated in time.

Comparing Eq. (21) with Eq. (19), we note that  $\infty$ -norm measures the response to the “worst” frequency, whereas 2-norm measures the response to all frequencies in an average sense.

### 3.2.1 Input-Output Analysis of the Flat-Plate Boundary Layer

Before we consider the full system in Fig. 22, the input-output behavior between the disturbance and objective function is characterized; the “sensor”, “controller” and “actuator” are not included in the analysis for now. Consider the stable linear system  $\mathbf{G}$  given by; (i) the Navier–Stokes equations linearized about the steady boundary-layer flow ( $\mathbf{A} \in \mathbb{R}^{n \times n}$ ), (ii) a two-dimensional volume forcing inside the boundary layer at an upstream location ( $\mathbf{B}_1 \in \mathbb{R}^{n \times 1}$ ) and (iii) a two-dimensional sensor ( $\mathbf{C}_1 \in \mathbb{R}^{1 \times n}$ ), also represented by function inside the boundary layer, but located further downstream.

We will characterize  $\mathbf{G}$  by computing its 2-norm and  $\infty$ -norm, since these measures are necessary components when performing model reduction and designing control schemes in the subsequent sections. The norms are obtained by computing the energy of the output signal  $\mathbf{y}$  when the input  $\mathbf{w}$  is a impulse/stochastic (2-norm) signal and harmonic signal ( $\infty$ -norm).

The 2-norm, defined by Eq. (20), is given by the output energy due to an impulsive input  $\mathbf{w}(t) = \delta(t)$ . The impulse response given by,

$$\mathbf{y}(t) = \mathbf{C}e^{\mathbf{A}t}\mathbf{B}, \quad (22)$$

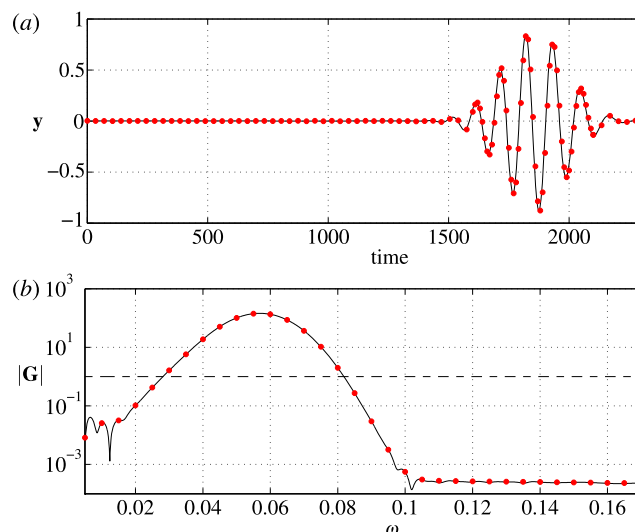


**Fig. 23** Impulse (a) and frequency response (b) of the flat-plate boundary layer. The black lines show responses from DNS computations ( $n \approx 10^5$ ). The red symbols show the responses from the reduced-order model ( $r = 60$ ) (Color figure online)

is shown in Fig. 23(a) with a black solid line. The impulse triggers a wavepacket that grows in amplitude as it propagates in the downstream direction. The output signal  $\mathbf{y}(t)$  is zero for a long time, but as the disturbance passes the sensor location, the wavepacket is registered. The 2-norm of  $\mathbf{G}$ , which for the present case is  $\|\mathbf{G}\|_2 = \|\mathbf{y}\|_{L^2} = 9.7$  quantifies the signal amplification of a unit norm input in an averaged sense.

The  $\infty$ -norm, defined by Eq. (19), is computed by finding the harmonic input signal that results in the largest output energy. The response to harmonic forcing  $\mathbf{w}(t) = e^{i\omega t}$  is given by

$$\mathbf{y}(t) = |\mathbf{G}(i\omega)|e^{i\omega t + \phi}. \quad (23)$$

Due to the linear nature of the system, the input frequency  $\omega$  will generate an output signal with same frequency but with a phase shift  $\phi = \text{Arg}(\mathbf{G})$  and a gain  $|\mathbf{G}(i\omega)|$ . The gain is shown in Fig. 23(b) with a black solid line. A range of frequencies are amplified with the peak at  $\omega = 0.055$ , whereas the low and high frequencies are damped. The  $\infty$ -norm is given by the peak value of the gain  $|\mathbf{G}|$ . In Table 3 the norms of  $\mathbf{G}$  are listed. In the next section, we attempt to construct a new system,  $\mathbf{G}_r$  with system norms very close to  $\mathbf{G}$ , but a significantly smaller dimension.

### 3.3 The Model Reduction Problem

The state space  $\mathbb{U}$  contains all possible solenoidal velocity fields that satisfy the boundary conditions. However, for a given structure of  $\mathbf{B}$  and  $\mathbf{C}$ , only certain velocity fields can be triggered by the input and observed by the output. These

states are called controllable and observable states respectively. The flow structures that are neither controllable nor observable are redundant for the input-output behavior. The minimum number of states<sup>6</sup>  $\hat{n} \leq n$  that can be both observed and controlled for a given  $\mathbf{B}$  and  $\mathbf{C}$  is defined as the *complexity* of  $\mathbf{G}$ . Henceforth we will omit the hat on  $\hat{n}$ . It turns out that when  $m, p \ll n$ , the complexity of  $\mathbf{G}$  can be significantly reduced, while preserving the relation between the inputs and outputs. The reason for this reduction is that a large number of the states are nearly uncontrollable/unobservable and they can be discarded since they have a very weak influence on the input-output behavior. A systematic approach of removing these states is called balanced truncation [69].

A *reduced-order system* (ROM) is an “approximation” of  $\mathbf{G}$ , defined as

$$\mathbf{G}_r = \left( \begin{array}{c|c} \mathbf{A}_r & \mathbf{B}_r \\ \hline \mathbf{C}_r & \mathbf{D}_r \end{array} \right),$$

such that the complexity of  $\mathbf{G}_r$  is  $r$  where  $r \ll n$ . We would like to choose  $\mathbf{G}_r$  such that

$$\|\mathbf{G} - \mathbf{G}_r\|_\infty \quad (24)$$

is small. Requiring a small error in the 2-norm is a substantially more difficult problem.

### 3.3.1 SVD of the Hankel Operator

Matrices and linear systems are both linear transformations and have thus a lot in common. It is well known that if one wants to approximate an  $n$ -rank matrix  $\mathbf{A}$  with a  $r < n$  rank matrix  $\mathbf{A}_r$ , then the smallest possible error is given by

$$\min_{\text{rank}(\mathbf{A}_r) \leq r} \|\mathbf{A} - \mathbf{A}_r\| = \sigma_{r+1}, \quad (25)$$

where  $\|\cdot\|$  is the induced Euclidean norm and  $\sigma_{r+1}$  is the  $r + 1$  largest singular value of  $\mathbf{A}$ . One can also compute singular value decomposition (SVD) of signals which amounts to a POD analysis [69]. However, a SVD of a linear input-output system  $\mathbf{G}$  in order to find a  $\mathbf{G}_r$  is not straightforward, since  $\mathbf{G}$  is not always a finite rank operator. In fact there is no known solution to the optimal model reduction problem in the infinity norm. A simpler input-output mapping, is the finite-rank *Hankel operator*  $\mathbf{\Gamma}_G : L^2(-\infty, 0] \rightarrow L^2[0, \infty)$  of the system  $\mathbf{G}$ , defined by

$$(\mathbf{\Gamma}_G \mathbf{w})(t) = \int_{-\infty}^0 \mathbf{C} e^{\mathbf{A}(t-s)} \mathbf{B} \mathbf{w}(s) ds.$$

The induced norm of  $\mathbf{\Gamma}_G$  is equal to the Hankel norm of  $\mathbf{G}$ ,

$$\|\mathbf{\Gamma}_G\|_\infty = \|\mathbf{G}\|_H$$

<sup>6</sup>In the literature,  $\hat{n}$  is referred to as the McMillan degree.

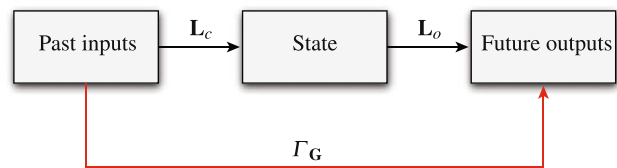


**Fig. 24** The controllability operator  $\mathbf{L}_c$  relates past inputs to the present state, while the observability mapping  $\mathbf{L}_o$  relates the present state to the future outputs. Their combined action is expressed by the Hankel operator  $\mathbf{\Gamma}_G$

The Hankel norm quantifies the energy transferred from past inputs to future outputs. In this norm there is a solution to the optimal model reduction problem, called the Hankel norm approximation [29]. However, we will use the Hankel operator to introduce a non-optimal model reduction problem, referred to as balanced truncation, which has error bounds very close (a factor of 2 larger in  $\infty$ -norm) to the Hankel norm approximation, but is considerably easier to compute.

To understand why  $\mathbf{\Gamma}_G$  has finite rank, we decompose the input-output operator into two parts

$$\mathbf{\Gamma}_G = \mathbf{L}_o \mathbf{L}_c.$$

The controllability operator  $\mathbf{L}_c : L^2(-\infty, 0] \rightarrow \mathbb{U}$ , maps past input signals to an initial state  $\mathbf{u}_0$ ,

$$\mathbf{L}_c \mathbf{w} = \int_{-\infty}^0 e^{-\mathbf{A}s} \mathbf{B} \mathbf{w}(s) ds. \quad (26)$$

The second mapping  $\mathbf{L}_o : \mathbb{U} \rightarrow L^2[0, \infty)$ , called observability operator, is from the initial state to future outputs signals,

$$\mathbf{L}_o \mathbf{u}_0 = \mathbf{C} e^{\mathbf{A}t} \mathbf{u}_0 \quad t \geq 0. \quad (27)$$

As sketched in Fig. 24, the input is mapped via a state at a reference time  $t = 0$ , given by  $\mathbf{u}_0 = \mathbf{L}_c \mathbf{w}$ , to the output given by  $\mathbf{y} = \mathbf{L}_o \mathbf{u}_0$ . Therefore in order to determine the output, it is sufficient to know the state  $\mathbf{u}_0$  that results from driving the system with  $\mathbf{w}$ . The key point is: all inputs that give rise to the same  $\mathbf{u}_0$  produce the same output. Any two linearly independent states,  $\mathbf{u}_1, \mathbf{u}_2 \in \mathbb{U}$  result in two linearly independent future outputs  $\mathbf{y}_1, \mathbf{y}_2 \in \mathbb{R}^p$ . Thus, the number of linearly independent outputs, and hence the rank of  $\mathbf{\Gamma}_G$ , is  $n$ .

We can compute the singular value decomposition (SVD) of  $\mathbf{\Gamma}_G$ ,

$$(\mathbf{\Gamma}_G \mathbf{w})(t) = \sum_{j=1}^n \sigma_j \langle \mathbf{s}_j, \mathbf{w} \rangle_{L^2} \mathbf{t}_j, \quad (28)$$

where  $\mathbf{s}_j \in L^2(-\infty, 0)$  and  $\mathbf{t}_j \in L^2(0, \infty)$  are sets of orthonormal signals. The singular values of  $\mathbf{\Gamma}_G$ ,  $\sigma_j > 0$  are called *Hankel singular values* (HSV) of  $\mathbf{G}$  and are ordered in descending order of magnitude. Of all possible unit-norm (past) input signals,  $\mathbf{s}_1$  results in the (future) output signal with the largest norm, given by  $\sigma_1^2 \mathbf{t}_1$ .

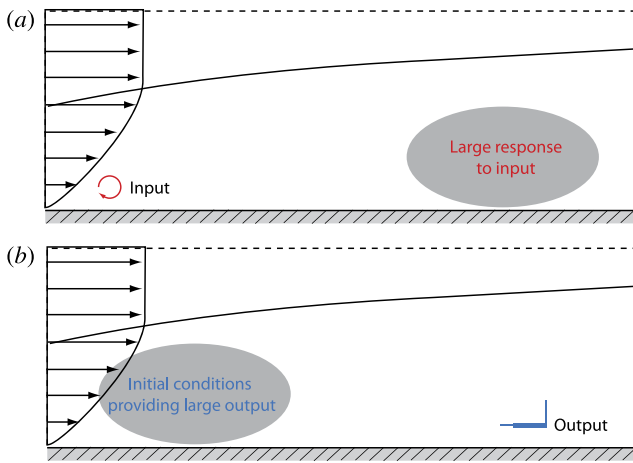


**Fig. 25** Sketch of controllability (a) and observability (b) for the flat-plate boundary layer. The response to an input is large downstream (because of strong convection), which results in a large controllability of flow structures in the downstream part of the domain. Similarly, the flow structures that will after a transient time, result in a large sensor output are located far upstream, resulting in strong observability in that region

### 3.3.2 Reduced-Order System

The mappings,  $\mathbf{L}_c$  and  $\mathbf{L}_o$ , are related to the concepts of controllability and observability. A state is called controllable if it belongs to the range of  $\mathbf{L}_c$ , that is, if  $\mathbf{u} = \mathbf{L}_c \mathbf{w}$  exists for some  $\mathbf{w}$ . By forming the  $n \times n$  positive (semi) definite matrix  $\mathbf{P}$ ,

$$\mathbf{P} = \mathbf{L}_c \mathbf{L}_c^T = \int_0^\infty e^{\mathbf{A}t} \mathbf{B} \mathbf{B}^T e^{\mathbf{A}^T t} dt, \tag{29}$$

called the controllability Gramian, we can rank different states according to how easily they can be influenced by an input. In particular, the most easily influenced, or most controllable, flow structures are the eigenvectors of  $\mathbf{P}$  associated to the largest eigenvalues of  $\mathbf{P}$ .

The linear system  $\mathbf{G}$  is observable if  $\mathbf{L}_o \mathbf{u}_0 = 0$  occur only if  $\mathbf{u}_0 = 0$ , i.e. if the knowledge of the output determines the initial state uniquely. Fluid systems are rarely completely observable when using localized sensing. However, among all possible  $\mathbf{u}_0$ , we can find the initial conditions which produce the largest possible output energy, by forming the  $n \times n$  observability Gramian  $\mathbf{Q}$ ,

$$\mathbf{Q} = \mathbf{L}_o^T \mathbf{L}_o = \int_0^\infty e^{\mathbf{A}^T t} \mathbf{C}^T \mathbf{C} e^{\mathbf{A}t} dt. \tag{30}$$

The matrix provides a way to rank states according to their contribution to the output. The most observable states are given by the eigenvectors of the matrix  $\mathbf{Q}$  corresponding to its largest eigenvalues. The sketch in Fig. 25, illustrates the concepts of the Gramians. Note that  $\mathbf{L}_o^T$  and  $\mathbf{L}_c^T$  are the adjoint observability and controllability operators respectively and are derived in [10].

It is easy to show (see [31], p. 344) that (28) holds if

$$\mathbf{P} \mathbf{Q} \boldsymbol{\phi}_i = \sigma_i^2 \boldsymbol{\phi}_i, \quad i = 1, \dots, n. \tag{31}$$

We call the eigenvectors,  $\boldsymbol{\phi}_j \in \mathbb{U}$ , *balanced modes*. This set is not orthogonal, and we define the set of left eigenvectors of  $\mathbf{P} \mathbf{Q}$  as the *adjoint balanced modes* and denoted them by  $\boldsymbol{\psi}_j \in \mathbb{U}$ . The two sets are bi-orthogonal, i.e.

$$\langle \boldsymbol{\phi}_i, \boldsymbol{\psi}_j \rangle_{\mathbb{U}} = \delta_{ij}.$$

The balanced mode  $\boldsymbol{\phi}_j$  is a global structure in the flow that is “influenced” by the input  $\mathbf{B}$  by an amount given by its HSV  $\sigma_j$ , whereas the corresponding adjoint mode  $\boldsymbol{\psi}_j$  is a flow structure that—if used as an initial condition—will result in an output energy  $\|\mathbf{y}\|_{L_2}$  given also by  $\sigma_j$ . These global modes that come in pairs have thus ranked the flow fields according to their response behavior (controllability) and output sensitivity (observability).

Let the columns of the matrices  $\boldsymbol{\Phi}$  and  $\boldsymbol{\Psi}$  contain  $r$  balanced modes and  $r$  adjoint modes respectively, corresponding to the  $r$  largest HSV,

$$\boldsymbol{\Phi} = [\boldsymbol{\phi}_1 \quad \dots \quad \boldsymbol{\phi}_r], \quad \boldsymbol{\Psi} = [\boldsymbol{\psi}_1 \quad \dots \quad \boldsymbol{\psi}_r].$$

The *reduced order system*  $\mathbf{G}_r$  is given by,

$$\mathbf{G}_r = \left( \begin{array}{c|c} \boldsymbol{\Psi}^T \mathbf{A} \boldsymbol{\Phi} & \boldsymbol{\Psi}^T \mathbf{B} \\ \hline \mathbf{C} \boldsymbol{\Phi} & \mathbf{D} \end{array} \right).$$

To obtain the above system, we have performed an oblique projection of the original high-dimensional state-space system (15a)–(15b) onto a subspace  $\mathbb{U}_r \subset \mathbb{U}$  spanned by  $r$  balanced modes. The projection is along a direction orthogonal to the subspace  $\mathbb{U}_r^* \subset \mathbb{U}$  spanned by the adjoint balanced modes (see [1], p. 12). Traditionally, to obtain  $\mathbf{G}_r$  one adopts a transformation-truncation approach [69] called *balanced truncation*. In this approach—which also explains the term balancing—the system  $\mathbf{G}$  is via a linear transformation represented in coordinates, where the controllability and observability Gramians are diagonal and equal to the HSV (the controllable and observable properties are thus “balanced”).

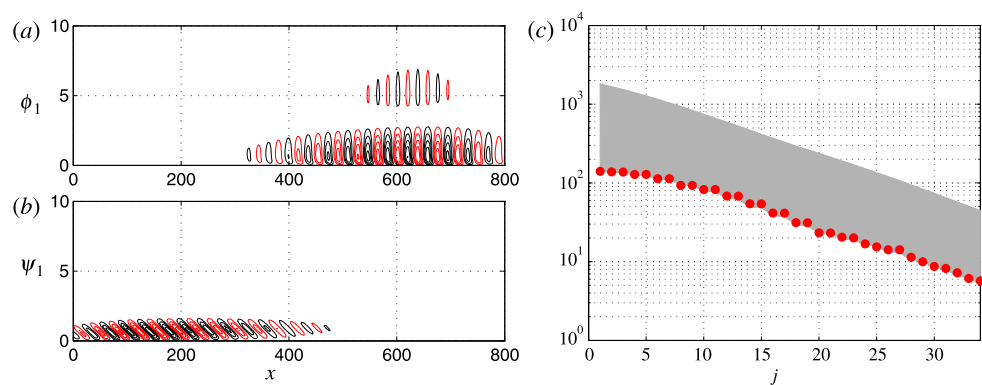
The system  $\mathbf{G}_r$  is not optimal in any way, although it is derived from SVD of the Hankel operator. Nevertheless, balanced truncation is arguably the most widely used method for model reduction of linear input-output systems, because of the following two properties:

1.  $\mathbf{G}_r$  is guaranteed to be asymptotically stable if  $\sigma_j \neq \sigma_{j+1}$  for all  $j$  [77];
2. there exist tight error bounds [29],

$$\sigma_{r+1} \leq \|\mathbf{G} - \mathbf{G}_r\|_\infty \leq 2 \sum_{j=r+1}^n \sigma_j \tag{32}$$

that can be determined *a priori* to computing  $\mathbf{G}_r$ .

**Fig. 26** *Left:* The streamwise velocity component (positive in red and negative in black) of first balanced mode  $\phi_1$  and its associated adjoint mode  $\psi_1$ . *Right:* The  $\infty$ -norm model reduction error. The upper and lower theoretical bounds (Eq. 32) are depicted with a gray region and the actual model reduction error is shown with red symbols (Color figure online)



Comparing the error bound to Eq. (25), we see that the Hankel singular values play a similar role in linear systems to singular values of matrices.

### 3.3.3 Model Reduction of the Flat-Plate Boundary Layer

We return to the single-input single-output flat-plate boundary layer example, where the number of degrees of freedom to describe two-dimensional disturbances is  $n \approx 10^5$ . In this section, we construct a low-order model  $\mathbf{G}_r$  using balanced modes and compare its performance to the Navier–Stokes system.

When the input  $\mathbf{B}_1$  is placed upstream and the output  $\mathbf{C}_1$  downstream, the controllable velocity fields and the observable fields are spatially separated in the streamwise direction. As shown in schematically in Fig. 25, observability is strong far upstream, whereas controllability is strong at the downstream part of the domain. This is a consequence of the convective nature of the instabilities arising in the Blasius flow where disturbances grow in amplitude as they are convected in the downstream direction. The large difference between observable and controllable states, makes it particularly important to perform balancing in order to construct a reduced-order model that captures the input-output behavior. Figure 26(a)–(b) show that the first adjoint ( $\psi_1$ ) and forward balanced mode ( $\phi_1$ ) appear as localized wavepackets, located at each end of the domain. Modes corresponding to higher HSV look similar, but have different spatial wavelengths. It is because of the bi-orthogonal projection, where the adjoint balanced modes account for the output sensitivity and the direct balanced modes for the most controllable structures, that the resulting reduced-order model captures the input-output behavior. It is interesting to point out that for many convectively unstable flows, this spatial separation is also observed between the global eigenmodes of the linearized Navier–Stokes equations and eigenmodes of the adjoint Navier–Stokes equations, where it is associated to the streamwise nonnormality of the system [20].

In Fig. 23 the impulse and frequency responses of the balanced reduced-order model  $\mathbf{G}_r$  ( $r = 60$ ) are compared to

full Navier–Stokes system ( $n = 10^5$ ). We observe that the curves essentially collapse for both types of forcing, albeit the remarkable reduction in the number of degrees of freedom. This clearly indicates that capturing the input-output behavior of a linear system when  $m, p \ll n$  (in this single-input single-output case  $m = p = 1$ ) requires significantly smaller degrees of freedom, compared to capturing the full spatiotemporal disturbance dynamics. A more quantitative evaluation is provided in Fig. 26(b), where the actual model reduction error  $\|\mathbf{G} - \mathbf{G}_r\|_\infty$  is compared to the theoretical error bounds given by HSV (32). We observe that the error (red circles) decays rapidly with increasing modes, and is close to the lower theoretical bound. Note that the lower bound in the  $\infty$ -norm holds for *any* model reduction procedure applied to a linear system and not only balanced reduced-order model. See also Table 3 for the norms of  $\mathbf{G}_r$  ( $r = 60$ ).

### 3.4 The Control Problem

In the previous sections, we have characterized the input-output behavior of the plant (Navier–Stokes system)  $\mathbf{G}$  by computing system norms. In the context of flow stability, large system norms are closely linked to transient growth of perturbation energy (see e.g. [16, 17], for more on this relation). By minimizing the system norms we can expect smaller transient growth of perturbations and a laminar flow system that is less likely to transition to turbulence.

The control problem can be formulated as follows: By applying feedback control to  $\mathbf{G}$ , find a closed-loop system

$$\mathbf{G}_c = \left( \begin{array}{c|c} \mathbf{A}_c & \mathbf{B}_c \\ \hline \mathbf{C}_c & \mathbf{D}_c \end{array} \right),$$

such that

$$\|\mathbf{G}_c\|_2 < \|\mathbf{G}\|_2 \quad (33)$$

and its complexity is of the same order as the plant  $\mathbf{G}$ . Recall from Sect. 3.2 that the 2-norm of a system is the output energy when the input to the system is a stochastic process.

In other words, forcing both systems  $\mathbf{G}$  and  $\mathbf{G}_c$  with unit-variance white noise, the closed-loop system is required to result in a significantly smaller output signal than the plant. The aim of this section is to design  $\mathbf{A}_c, \mathbf{B}_c, \mathbf{C}_c$  and  $\mathbf{D}_c$  such that the 2-norm of  $\mathbf{G}_c$  is the smallest possible. We present a systematic method to find  $\mathbf{G}_c$ , known as the linear quadratic Gaussian (LQG) optimal control problem [6, 25, 26, 60]. The main disadvantage of LQG is that it does not account for uncertainties of the system  $\mathbf{G}$  [24] which is required to guarantee a robust performance and even robust stability of the closed loop system  $\mathbf{G}_c$ . One can only check the robustness by *ad-hoc* testing the controller for various parameters. The LQG problem can be extended to robust optimal control problem referred to as the  $H_\infty$  control, see [11, 106].

### 3.4.1 The Plant

So far in this section, the inputs has represented disturbances and the outputs some arbitrary sensor measurements. In order to construct  $\mathbf{G}_c$  by formulating a feedback control problem, we need to arrange the inputs and outputs in a specific manner [25]. Consider the following stable plant (or open-loop system) with three inputs and two outputs,

$$\dot{\mathbf{u}} = \mathbf{A}\mathbf{u} + \mathbf{B}_1 w_1 + \mathbf{B}_2 w_2 \tag{34a}$$

$$y_1 = \mathbf{C}_1 \mathbf{u} + l w_2 \tag{34b}$$

$$y_2 = \mathbf{C}_2 \mathbf{u} + \alpha g. \tag{34c}$$

The system (34a)–(34c) in a compact form is given by

$$\mathbf{G} = \left( \begin{array}{c|cc} \mathbf{A} & \mathbf{B}_1 & 0 & \mathbf{B}_2 \\ \hline \mathbf{C}_1 & 0 & 0 & l \\ \mathbf{C}_2 & 0 & \alpha & 0 \end{array} \right). \tag{35}$$

Figure 22 shows a sketch corresponding to the above system. The physical shape of the inputs/outputs, described by the constant input and output vectors  $\mathbf{B} = [\mathbf{B}_1 \ 0 \ \mathbf{B}_2]$  and  $\mathbf{C} = [\mathbf{C}_1 \ \mathbf{C}_2]^T$ , were discussed in Sect. 3.1. The corresponding time signals  $\mathbf{w}(t) = [w_1 \ g \ w_2]^T$  and  $\mathbf{y}(t) = [y_1 \ y_2]^T$  represent the following:

- The disturbance signal  $w_1$  is assumed to be a temporal white noise with unit intensity.
- The control signal  $w_2$  is to be determined in order to minimize the objective function.
- The objective functional is the mean of the output signal  $y_1$ ,

$$E(\|y_1\|_{L^2}^2) = E\left(\int_0^\infty (\mathbf{u}^T \mathbf{C}_1^T \mathbf{C}_1 \mathbf{u} + l^2 w_2^T w_2) dt\right). \tag{36}$$

The disturbance energy is minimized in the domain defined by  $\mathbf{C}_1$ , and at the same time the control effort is penalized with a scalar  $l$ .

- The measurement signal  $y_2$  estimates amplification and phase of temporal frequencies in the flow at the location of the sensor  $\mathbf{C}_2$ . The signal is forced with an unit variance temporal noise  $g(t)$  (large values of the scalar  $\alpha$ , indicate high level of noise corruption).

As alluded to above, we will determine the optimal control  $w_2(t)$  in (34a)–(34c) based on noisy measurements  $y_2(t)$  such that the cost functional (36) is minimized. The assumptions that external disturbances  $w_1$  and the sensor noise  $g$  are white noise may in some applications be unrealistic, however, it is possible to describe a system with colored noise input, in terms of an augmented system with white-noise input [60].

### 3.4.2 Linear Quadratic Gaussian Design

One can show [25] that the system  $\mathbf{G}_c$  with smallest 2-norm, satisfies

$$\|\mathbf{G}_c\|_2^2 = \underbrace{\|\mathbf{G}_f\|_2^2}_{\text{Full information}} + \underbrace{\|\mathbf{G}_e\|_2^2}_{\text{Estimation}}.$$

In order to construct  $\mathbf{G}_c$  we need to compute two simpler linear systems  $\mathbf{G}_f$  and  $\mathbf{G}_e$ , by solving a full-information control and an estimation problem. It turns out that the two systems  $\mathbf{G}_f$  and  $\mathbf{G}_e$  can be solved independently from each other. Moreover, if both subsystems are stable and optimal then the closed-loop system is also guaranteed to be stable and optimal.

We briefly state the solution of the two problems and refer to [25] for details.

*Full-Information Problem* In this first step, assume we can measure the full state at all times. We further assume that the control  $w_2(t)$  and the state  $\mathbf{u}(t)$  satisfy a linear relation involving some yet unknown matrix  $\mathbf{K}$ , i.e.

$$w_2(t) = \mathbf{K}\mathbf{u}(t). \tag{37}$$

Inserting (37) into (34a)–(34c) and neglecting the redundant output  $y_2$ , we get

$$\mathbf{G}_f = \left( \begin{array}{c|c} \mathbf{A} + \mathbf{B}_2 \mathbf{K} & \mathbf{B}_1 \\ \hline \mathbf{C}_1 + l \mathbf{K} & 0 \end{array} \right).$$

It remains to choose  $\mathbf{K}$  such that  $\mathbf{G}_f$  is stable and the control signal  $w_2(t)$  minimizes the system norm  $\|\mathbf{G}_f\|_2$ . The solution is provided by a optimal control state-feedback problem, (see e.g. [6]), where the optimal control signal (37) is given by the feedback gain,

$$\mathbf{K} = -\mathbf{B}_2^T \mathbf{X},$$

and  $\mathbf{X}$  is a solution of the (algebraic) Riccati equation

$$0 = \mathbf{A}^T \mathbf{X} + \mathbf{X} \mathbf{A} - \mathbf{X} \mathbf{B}_2 \mathbf{B}_2^T \mathbf{X} + \mathbf{C}_1^T \mathbf{C}_1.$$

**Estimation Problem** The second step in constructing  $\mathbf{G}_c$  is to estimate the full state  $\mathbf{u}(t)$  via the linear system  $\mathbf{G}_e$  given only the noisy measurements  $y_2$ . Denoting the estimation error by  $\mathbf{u}_e = \mathbf{u} - \hat{\mathbf{u}}$ , where  $\hat{\mathbf{u}}$  is the estimated state and assuming that both  $w_1$  and  $g$  are white noise processes, an estimator can be formulated as follows

$$\dot{\mathbf{u}}_e = \mathbf{A}\mathbf{u}_e + \mathbf{B}_1 w_1 + \mathbf{L}(y_2 - \hat{y}_2) \quad (38a)$$

$$\hat{y}_2 = \mathbf{C}_2 \hat{\mathbf{u}} \quad (38b)$$

$$y_2 = \mathbf{C}_2 \mathbf{u} + \alpha g. \quad (38c)$$

In the above expression, we compare the measurement  $y_2$  from the state and the measurement  $\hat{y}_2$  from the estimated state and feed back the mismatch in these two quantities using the estimator gain  $\mathbf{L}$ .

It can be shown [49] that the estimation gain that minimizes the estimation error  $\|\mathbf{u}_e\|_{L^2(0,\infty)}$  and results in a stable estimator is given by

$$\mathbf{L} = -\mathbf{Y}\mathbf{C}_2^T,$$

where  $\mathbf{Y}$  is a solution of the Riccati equation,

$$0 = \mathbf{A}\mathbf{Y} + \mathbf{Y}\mathbf{A}^T - \mathbf{Y}\mathbf{C}_2^T\mathbf{C}_2\mathbf{Y} + \mathbf{B}_1\mathbf{B}_1^T.$$

Now, if the state has been successfully estimated, it can be shown that the optimal control signal  $w_2(t)$  is given by  $w_2(t) = \mathbf{K}\hat{\mathbf{u}}(t)$  where  $\mathbf{K}$  is the full information control gain computed previously. By substituting the explicit dependence of the two measurements on the state  $\mathbf{u}$  and the estimated state  $\hat{\mathbf{u}}$ , respectively, into the estimator (38a)–(38c) we obtain the second part of the closed-loop system  $\mathbf{G}_c$ :

$$\mathbf{G}_e = \left( \begin{array}{c|c} \mathbf{A} + \mathbf{L}\mathbf{C}_2 & \mathbf{B}_1 \quad \alpha\mathbf{L} \\ \hline \mathbf{K} & 0 \quad 0 \end{array} \right).$$

Note that the input of  $\mathbf{G}_e$  is  $[w_1 \ g]^T$  and the output is the control signal  $w_2$ .

**The Closed-Loop System** The cost of solving a Riccati equation is  $O(n^3)$ , which is a computationally intractable task when  $n > 10^5$ . In the previous section we showed that our reduced model  $\mathbf{G}_r$  is able to capture the input-output behavior of the Navier–Stokes system  $\mathbf{G}$ . During the design of  $\mathbf{G}_c$  we can assume that the reduced-model is the plant that we wish to control. Once we have determined  $\mathbf{G}_e$  and  $\mathbf{G}_f$  for this approximating model, we will apply it to the full Navier–Stokes system. This means that the feedback gains and have the same dimension ( $r$ ) as the reduced-order model  $\mathbf{G}_r$ .

The final step is to connect the controller  $\mathbf{G}_f$  and the estimator  $\mathbf{G}_e$  to the plant  $\mathbf{G}$  given by Eq. (35) to obtain the matrices  $\mathbf{A}_c$ ,  $\mathbf{B}_c$ ,  $\mathbf{C}_c$  and  $\mathbf{D}_c$  of closed-loop system  $\mathbf{G}_c$ . A straightforward derivation gives

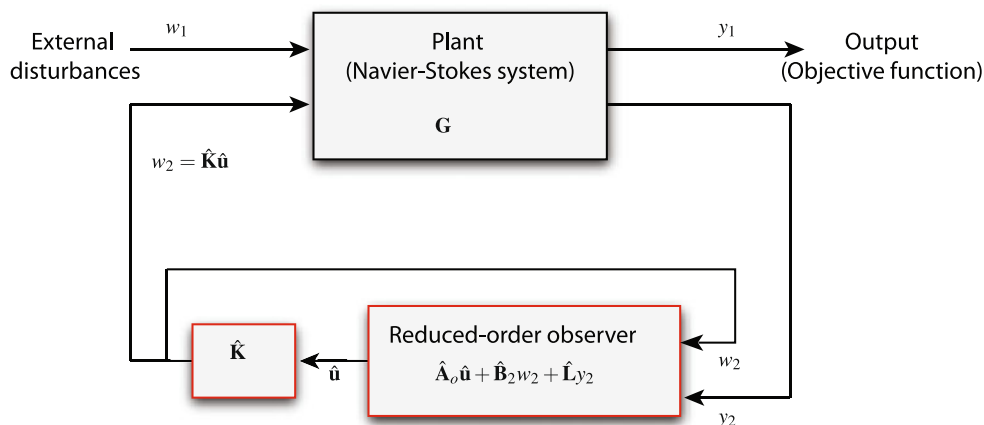
$$\mathbf{G}_c = \left( \begin{array}{cc|cc} \mathbf{A} & \mathbf{B}_2\hat{\mathbf{K}} & \mathbf{B}_1 & 0 \\ -\hat{\mathbf{L}}\mathbf{C}_2 & \hat{\mathbf{A}} + \hat{\mathbf{B}}_2\hat{\mathbf{K}} + \hat{\mathbf{L}}\hat{\mathbf{C}}_2 & 0 & -\alpha\hat{\mathbf{L}} \\ \hline \mathbf{C}_1 & \hat{\mathbf{L}}\hat{\mathbf{K}} & 0 & 0 \end{array} \right).$$

The output of the system is  $y_1$  and the inputs are  $[w_1 \ g]^T$ . The state for the above system is  $[\mathbf{u} \ \hat{\mathbf{u}}]^T \in \mathbb{R}^{(n+r) \times 1}$  where  $\mathbf{u} \in \mathbb{U}$  is the full state and the  $\hat{\mathbf{u}} \in \mathbb{R}^{r \times 1}$  is the reduced estimated state. A sketch of the closed-loop system is shown in Fig. 27. It is important to note that in the above closed-loop system the quantities marked with hat are of order  $r \ll n$ . This results in a fast “online” controller running in parallel with the experiments. As shown in Fig. 27, the controller can be decomposed into an observer governed by  $(\hat{\mathbf{A}} + \hat{\mathbf{L}}\hat{\mathbf{C}}_2)\hat{\mathbf{u}} + \hat{\mathbf{B}}_2 w_2 + \hat{\mathbf{L}}y_2$  and the feedback gain  $\hat{\mathbf{K}}$ .

### 3.4.3 Feedback Control of the Flat-Plate Boundary Layer

The full input-output system  $\mathbf{G}$  for the flat-plate boundary layer is shown in Fig. 22 and was described in Sect. 3.1. Recall that LQG design minimizes the 2-norm of the closed-loop system  $\mathbf{G}_c$  when the external disturbances ( $w_1, g$ ) are white noise process. We therefore force both systems  $\mathbf{G}$

**Fig. 27** Sketch of the closed-loop system  $\mathbf{G}_c$ . The controller (red borders) of order  $r$  consists of an observer and feedback gain  $\hat{\mathbf{K}}$  that forces the plant  $\mathbf{G}$  of size  $n$  with the control signal  $w_2$  based on the noisy measurements  $y_2$  so that the effect of  $w_1$  on the output signal  $y_1$  is minimized. The observer is governed by  $\hat{\mathbf{A}}_o = \hat{\mathbf{A}} + \hat{\mathbf{L}}\hat{\mathbf{C}}_2$  (Color figure online)



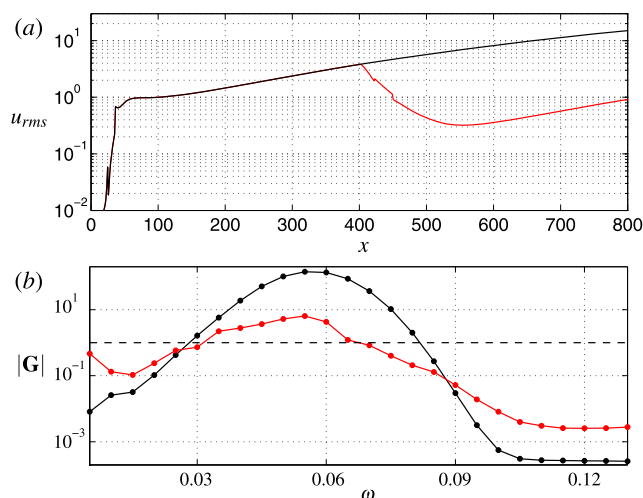


**Fig. 28** (a) The streamwise rms-values of the uncontrolled system (blacks), and the closed-loop (red) as a function of the streamwise direction  $x$ . (b) Comparison of the frequency response from disturbances to objective function of uncontrolled (black) and the closed-loop system (red) (Color figure online)

and  $\mathbf{G}_c$  with unit-variance white noise signal in  $w_1$  and compare the root-mean-square values (averaged in the directions  $z, y$  and the time  $t$ ) of the streamwise velocity component  $u$ . Note that the purpose of the measurement noise  $g$  is to account for uncertainties in the sensor measurements during the control design. When evaluating the closed-loop performance the system is only forced with  $w_1$ . In Fig. 28(a) the performance of a controller is investigated with (control penalty)  $l = 0.1$  and (sensor noise contamination)  $\alpha = 0.1$ . The rms-value of the disturbance grows exponentially downstream in the uncontrolled case until  $x = 800$ . The rms-value of the perturbation when the control is active grows only until it reaches the actuator position ( $x = 400$ ), where it immediately begins to decay. At the location of the objective function  $\mathbf{C}_1$  ( $x = 750$ ), the amplitude of the perturbation is one order of magnitude smaller than in the uncontrolled case.

There are a number of additional ways to evaluate the control performance. In Fig. 28(b) the frequency response from the disturbance  $\mathbf{B}_1$  to the objective function  $\mathbf{C}_1$  of the uncontrolled system is compared to that of the closed-loop system. The controller suppresses the most dangerous frequencies close to  $\omega = 0.055$  significantly. Note that compared to the uncontrolled model, the highly damped frequencies  $\omega > 0.11$  have larger gain in amplitudes. This behavior is often observed in closed-loop systems and is related to the “water-bed” effect, i.e. when certain frequencies are suppressed, the response at other frequencies is amplified. The 2-norm and the  $\infty$ -norm of  $\mathbf{G}_c$  are compared to those of the plant in Table 3, which illustrates the significantly smaller of the amplifying behavior of  $\mathbf{G}_c$ .

We have shown that by using systematic methods from control theory in combination with localized sensing/actu-

ation, it is possible to reduce the growth of small-amplitude disturbances in the boundary layer. As demonstrated in the introduction of this section, using this approach, the energy of three-dimensional disturbances are damped by an order of magnitude. Further conclusions are provided in the final section of this paper.

#### 4 Algorithms for Global Modes

To accurately describe the flow dynamics in two- or three-dimensional domains, a large number of degrees of freedom is necessary, yielding a high-dimensional dynamical system (2). Table 4 shows the dimension of the state space  $\mathbb{U}$  for the flow cases. Dynamical-system analysis involving the computation of steady solutions, global eigenmodes and Koopman modes commonly involves solving nonlinear systems or eigenvalue problems of size  $n$ . In systems and control theory the most elegant results require the solution of various matrix equations, such as the Riccati or Lyapunov equations. All of these computations scale  $O(n^3)$ , which means that even with the use of supercomputers it is prohibitively expensive to solve such problems for large systems. Therefore, numerical linear algebra and numerical algorithms to find approximate solutions have played a central role in computational fluid mechanics.

The main idea of the methods presented here is to identify a low dimensional subspace  $\mathbb{U}_r \subset \mathbb{U}$  with  $r \ll n$ , on which the large systems can be projected along a certain direction. The problem at hand can then be solved by standard methods in this low-dimensional subspace. The subspace is spanned by  $r$  prudently chosen states  $\mathbf{u}$

$$\mathbb{U}_r = \text{span}\{\mathbf{u}_1, \dots, \mathbf{u}_r\}.$$

In the simplest case, these states are simply sampled along one or more state trajectories obtained by integrating the governing equations, whereas in other cases a recurrence relation provides the necessary states. In either case, all the methods require flow fields at discrete time and it is therefore convenient to present the algorithms using discrete-time systems. In this so called “time-stepper approach”, matrices are never stored explicitly and storage demands in memory

**Table 4** Example of the state-space dimension for some of flow configurations

	Dimension of $\Omega$	Dimension of $\mathbb{U}$	Storage of $\mathbf{A}$
Ginzburg-Landau	1D	$10^2$	1 MB
Flat-plate boundary layer	2D	$10^5$	25 GB
Jet in crossflow	3D	$10^7$	500 TB

of all algorithms are of the same order as  $r$  times the storage of a single flow field.

Recall that the time-discrete dynamical system representing the discretized Navier–Stokes equations is given by

$$\mathbf{u}_{k+1} = \mathbf{g}(\mathbf{u}_k), \quad (39)$$

and let the linearized equations be given by

$$\mathbf{u}_{k+1} = \mathbf{A}_\mu \mathbf{u}_k \quad (40)$$

where

$$\mathbf{A}_\mu \mathbf{u}_k = \exp(\mathbf{A}\Delta t(k+1))\mathbf{u}(k\Delta t).$$

#### 4.1 Linear Global Eigenmodes

In Sect. 2.2 we defined the linear global eigenmodes as the eigenvectors  $\phi_j$  and eigenvalues  $\lambda_j$  of the discretized and linearized Navier–Stokes equations  $\mathbf{A}$ . Solving the enormous eigenvalue problem for the  $n \times n$  matrix  $\mathbf{A}$  using direct methods (such as the QR algorithm) is not only an unfeasible computational task when  $n \geq 10^5$ , but also very wasteful since we are interested in a small subset of the spectrum only: in order to determine the stability of the baseflow and to gain insight into the main instability mechanisms it is sufficient to compute a few, say  $r \ll n$ , of the least stable global modes. Fortunately, it turns out that we can compute  $r$  approximate global modes  $\tilde{\lambda}_j, \tilde{\phi}_j$  from a small eigenvalue problem of size  $r \times r$ .

Note that the  $j$ th eigenvalue,  $\lambda_j = \sigma_j + i\omega_j$ , of the time-continuous matrix  $\mathbf{A}$  is related to the  $j$ th eigenvalue,  $\lambda_{\mu,j}$ , of the time-discrete matrix  $\mathbf{A}_\mu$  as follows:

$$\omega_j = \arg(\lambda_{\mu,j})/\Delta t, \quad \sigma_j = \ln(|\lambda_{\mu,j}|)/\Delta t. \quad (41)$$

The eigenvectors of  $\mathbf{A}$  and  $\mathbf{A}_\mu$  are the same.<sup>7</sup> Henceforth, the subscript  $\mu$  on  $\mathbf{A}_\mu$  and  $\lambda_\mu$  is omitted and we work entirely with discrete-time systems.

Denoting the residual (i.e. the error) introduced by the approximation with  $\mathbf{r}_j$ , we have

$$\mathbf{A}\tilde{\phi}_j = \tilde{\phi}_j\tilde{\lambda}_j + \mathbf{r}_j, \quad j = 1, \dots, r. \quad (42)$$

One can show that by requiring the residual  $\mathbf{r}_j$  to be orthogonal to a  $r$ -dimensional subspace  $\mathbb{U}_r \subset \mathbb{U}$ , we can choose  $\tilde{\lambda}_j, \tilde{\phi}_j$  such the error is the smallest possible. Let  $r$  of linearly independent vectors given in the matrix,

$$\mathbf{X}_r = [\mathbf{u}_1 \quad \mathbf{u}_2 \quad \dots \quad \mathbf{u}_r] \in \mathbb{R}^{n \times r}, \quad (43)$$

<sup>7</sup>The eigenvectors are the same if the sampling period  $\Delta t$  is chosen properly, i.e. so that it reflects the characteristic time scale of the physical structures in the flow. More specifically, to avoid aliasing  $\Delta t$  must be small enough such that two sampling points in one period of the highest frequency mode are obtained (the Nyquist criterion).

span  $\mathbb{U}_r$ . We call  $\tilde{\lambda}_j$  the *Ritz values* of  $\mathbf{X}_r$  associated with the *Ritz vectors*  $\tilde{\phi}_j$  if

$$\tilde{\phi}_j \in \text{span}\{\mathbf{X}_r\}, \quad \mathbf{r}_j \perp \text{span}\{\mathbf{X}_r\}.$$

Since  $\tilde{\phi}_j \in \text{span}\{\mathbf{X}_r\}$ , we can expand it in terms of the columns of  $\mathbf{X}_r$ ,

$$\tilde{\Phi} = [\tilde{\phi}_1 \quad \tilde{\phi}_2 \quad \dots \quad \tilde{\phi}_r] = \mathbf{X}_r \mathbf{T}, \quad (44)$$

where the yet unknown matrix  $\mathbf{T} = [T_1 \quad \dots \quad T_r] \in \mathbb{R}^{r \times r}$  contains the expansion coefficients. Inserting this expansion into (42), multiplying from left with  $\mathbf{X}_r^T$  and letting

$$\tilde{\Lambda} = \text{diag}\{\tilde{\lambda}_1, \tilde{\lambda}_2, \dots, \tilde{\lambda}_r\},$$

we get

$$\underbrace{\mathbf{X}_r^T \mathbf{A} \mathbf{X}_r}_{\mathbf{C}_r} \mathbf{T} - \underbrace{\mathbf{X}_r^T \mathbf{X}_r}_{\mathbf{B}_r} \mathbf{T} \tilde{\Lambda} = 0, \quad (45)$$

since  $\mathbf{X}_r^T \mathbf{r}_j = 0$  for all  $j$ . The expansion coefficients  $\mathbf{T}$  are thus the eigenvectors and the Ritz values the eigenvalues of the small  $r \times r$  matrix  $\mathbf{B}_r^{-1} \mathbf{C}_r$ ,

$$(\mathbf{B}_r^{-1} \mathbf{C}_r) \mathbf{T} = \mathbf{T} \tilde{\Lambda}. \quad (46)$$

We have replaced the large eigenvalue problem (7) of size  $n$  with a smaller one (46) of size  $r \ll n$ . The question is, how fast the Ritz values and vectors converge to exact linear global eigenmodes and with what accuracy? The answer depends on the choice of vectors  $\mathbf{u}_j$  in  $\mathbf{X}_r$ . Note that the matrix  $\mathbf{C}_r$  can be interpreted as the orthogonal projection of  $\mathbf{A}$  onto the space spanned by the columns of  $\mathbf{X}_r$ , where the projector is given by  $\mathbf{P}_r = \mathbf{X}_r \mathbf{B}_r^{-1} \mathbf{X}_r^T$ .

##### 4.1.1 Arnoldi Algorithm

The best—and computationally the most involved to determine—choice of basis for  $\mathbb{U}_r$ , resulting in a fast convergence with a satisfactory accuracy is an orthonormal basis. The Arnoldi method [8] is an algorithm that simultaneously computes an orthonormal sequence  $\mathbf{B}_r = \mathbf{X}_r^T \mathbf{X}_r = \mathbf{I}$  and an upper Hessenberg matrix  $\mathbf{C}_r = \mathbf{X}_r^T \mathbf{A} \mathbf{X}_r$ .

The method of Arnoldi computes the  $j + 1$  basis vector in  $\mathbf{X}_r$  by the recurrence

$$\mathbf{v} = \mathbf{A} \mathbf{u}_j - (h_{1j} \mathbf{u}_1 + h_{2j} \mathbf{u}_2 + \dots + h_{jj} \mathbf{u}_j) \quad (47a)$$

$$\mathbf{u}_{j+1} = \mathbf{v} / h_{j+1,j} \quad (47b)$$

where  $h_{ij} = \langle \mathbf{A} \mathbf{u}_j, \mathbf{u}_i \rangle$  and  $h_{j+1,j} = \|\mathbf{v}\|$ . This is simply the Gram-Schmidt method of orthogonalizing and normalizing a sequence. If we start with some unit-norm initial vector

**Algorithm 1** Arnoldi method

---

$[\Phi, \Lambda, r] = \text{Arnoldi}(\mathbf{u}_1)$

**Input:** unit norm initial vector  $\mathbf{u}_1$

**Output:**  $r$  Ritz vectors  $\Phi$   
 $r$  Ritz values  $\Lambda$   
residuals  $\mathbf{r}$

**Requires:** time stepper  $\mathbf{A}_\mu$

- 1:  $\mathbf{X}(:, 1) = \mathbf{u}_1$
- 2: **for**  $j = 1$  to  $r$  **do**
- 3:  $\mathbf{v} = \mathbf{A}_\mu \mathbf{u}_j$
- 4: **for**  $i = 1$  to  $j$  **do**
- 5:  $\mathbf{M}(i, j) = \text{innerproduct}(\mathbf{A}\mathbf{u}_j, \mathbf{u}_i)$
- 6:  $\mathbf{v} = \mathbf{v} - \mathbf{M}(i, j)\mathbf{u}_i$
- 7:  $\mathbf{M}(j + 1, j) = \text{norm}(\mathbf{v})$
- 8:  $\mathbf{u}_{j+1} = \mathbf{v}/\mathbf{M}(j + 1, j)$
- 9: **end for**
- 10:  $\mathbf{X}(:, j + 1) = \mathbf{u}_{j+1}$
- 11: **end for**
- 12:  $[\mathbf{T}, \Lambda] = \text{eig}(\mathbf{M})$
- 13:  $\Phi = \mathbf{X}\mathbf{T}$
- 14:  $\mathbf{r} = \text{norm}(\mathbf{A}\Phi - \Phi\Lambda, 1)$

---

(usually noise)  $\mathbf{u}_1$  and perform the above recurrence  $r + 1$  times, we arrive at the following expression,

$$\mathbf{A}\mathbf{X}_r = \mathbf{X}_r\mathbf{M} + h_{r+1,r}\mathbf{u}_{r+1}\mathbf{e}_r^T,$$

where  $\mathbf{e}_r^T = [0 \ 0 \ \dots \ 0 \ 1] \in \mathbb{R}^{1 \times r}$  and  $\mathbf{M}$  is an upper Hessenberg matrix

$$\mathbf{M} = \begin{bmatrix} h_{11} & h_{12} & \dots & h_{1r} \\ h_{21} & h_{22} & \dots & h_{2r} \\ 0 & h_{32} & \dots & h_{3r} \\ \vdots & & & \vdots \\ 0 & 0 & \dots & h_{rr} \end{bmatrix} \in \mathbb{R}^{r \times r}.$$

By construction of the Arnoldi algorithm we have  $\mathbf{u}_{r+1} \perp \mathbf{X}_r$ , therefore from (45) it is easy to see that  $\mathbf{M} = \mathbf{B}_r^{-1}\mathbf{C}_r = \mathbf{C}_r$ . The Ritz values of  $\mathbf{A}$  in  $\mathbb{U}_r$  are the eigenvalues  $\tilde{\Lambda}$  of the upper Hessenberg matrix  $\mathbf{M}$  and the Ritz vectors are given by  $\tilde{\Phi} = \mathbf{X}_r\mathbf{T}$  where the columns of  $\mathbf{T}$  are the eigenvectors of  $\mathbf{M}$  (see Algorithm 1).

The residual in Eq. (42) of the  $j$ th Ritz pair is thus given by

$$\mathbf{r}_j = (\mathbf{A} - \tilde{\lambda}_j\mathbf{I})\tilde{\phi}_j = h_{r+1,r}T_j(r)\mathbf{u}_{r+1},$$

where  $T_j(r)$  is the last component of the  $j$ th eigenvector of  $\mathbf{M}$ . One can stop the algorithm when the desired accuracy—usually  $\|\mathbf{r}_j\| \leq 10^{-10}$ —is attained for the Ritz vectors of interest. To avoid a very large  $r$  and still obtain

low residuals, one can repeat the Arnoldi algorithm with the initial vector  $\mathbf{u}_1$  replaced by a Ritz vector or a combination of Ritz vectors [86]. In the Arnoldi-software package ARPACK [58] a more efficient method based on polynomial filtering [96] is applied to obtain an improved initial guess. Moreover, the standard Gram-Schmid (47a)–(47b) gives rise to severe cancellation errors, so in practice more advanced techniques such as the modified Gram-Schmid method [103] are used.

4.1.2 Dynamic Mode Decomposition

The simplest—and most ill-conditioned—choice of basis for  $\mathbb{U}_r$  (see [85, 86]) is simply samples (or snapshots) obtained from the time-stepper

$$\mathbf{u}_{j+1} = \mathbf{A}\mathbf{u}_j.$$

The basis  $\mathbf{X}_r = [\mathbf{u}_1 \ \mathbf{A}\mathbf{u}_1 \ \mathbf{A}\mathbf{u}_2 \ \dots \ \mathbf{A}\mathbf{u}_{r-1}]$  becomes gradually ill-conditioned, since its columns gradually align with the dominant eigenvectors of  $\mathbf{A}$ . For some  $r$ , the vector at step  $r + 1$  becomes nearly linearly dependent of the previous  $r$  vectors, i.e.

$$\mathbf{u}_{r+1} = c_1\mathbf{u}_1 + c_2\mathbf{u}_2 + \dots + c_r\mathbf{u}_r + \tilde{\mathbf{u}}_{r+1}, \tag{48}$$

where  $\tilde{\mathbf{u}}_{r+1}$  is the residual, i.e. the part of  $\mathbf{u}_{r+1}$  that is not in the span of  $\mathbf{X}_r$ . We can write (48) in matrix form,

$$\mathbf{A}\mathbf{X}_r = \mathbf{X}_r\mathbf{M} + \tilde{\mathbf{u}}_{r+1}\mathbf{e}_r^T, \tag{49}$$

where  $\mathbf{e}_r^T = [0 \ 0 \ \dots \ 0 \ 1] \in \mathbb{R}^{1 \times r}$  and

$$\mathbf{M} = \begin{bmatrix} 0 & 0 & \dots & 0 & c_1 \\ 1 & 0 & \dots & 0 & c_2 \\ 0 & 1 & \dots & 0 & c_3 \\ \vdots & & \ddots & & \vdots \\ 0 & 0 & \dots & 1 & c_r \end{bmatrix} \in \mathbb{R}^{r \times r} \tag{50}$$

is a matrix in companion form. It remains to determine the scalar elements  $c_j$  of  $\mathbf{M}$ . If we choose them such that  $\tilde{\mathbf{u}}_{r+1} \perp \mathbf{X}_r$  then from (45) it is easy to see that  $\mathbf{M} = \mathbf{B}_r^{-1}\mathbf{C}_r$ : the Ritz values of  $\mathbf{A}$  in  $\mathbb{U}_r$  and the Ritz vectors  $\tilde{\Phi} = \mathbf{X}_r\mathbf{T}$  are thus attained by diagonalizing the companion matrix  $\mathbf{M}$ , instead of the upper Hessenberg matrix obtained via the Arnoldi method.

A few remarks are appropriate at this point. There is no normalization step in the algorithm, and hence the modes come with amplitudes,  $a_i = |\tilde{\phi}_i|$  that provide a way to rank their contribution to the overall energy in the set  $\mathbf{X}_r$ . The normalized amplitude  $a_i/a_1$  for mode  $\tilde{\phi}_i$  serves as a condition number for that mode. If  $a_i/a_1 \leq \tau$  where  $\tau$  is some tolerance (usually  $\tau = 10^{-15}$ ), then the corresponding mode is discarded. See the example in Sect. 4.1.3.

The companion matrix may be a highly nonnormal matrix, which results in an ill-conditioned eigenvalue decomposition problem. One can improve the accuracy in several steps as it is done by default in the eigenvalue routines of Lapack (DxGEEV) and Matlab (EIG); first, *balancing* [75] of the matrix by a similarity transformation is performed, followed by a reduction to upper Hessenberg form via a second similarity transformation and finally the eigenvalues are computed using the QR algorithm. Alternatively, as a preconditioning, one can perform a similarity transformation (via a singular value decomposition) of the companion matrix to obtain a full matrix  $\tilde{\mathbf{M}}$  [90].

The norm of the residual in Eq. (42) of the  $j$ th Ritz pair is given by

$$\mathbf{r}_j = (\mathbf{A} - \tilde{\lambda}_j \mathbf{I}) \tilde{\boldsymbol{\phi}}_j = \tilde{\mathbf{u}}_{j+1} T_j(r) \quad (51)$$

For a given dimension of  $\mathbb{U}_r$ , the residuals from this algorithm are significantly higher than the Arnoldi method. The advantage of this algorithm is that it provides Ritz vectors and values of any sequence of data. In contrast to the Arnoldi method, it does not perform  $\mathbf{A}\mathbf{u}_j$  at each step and is unaware of  $\mathbf{A}$  altogether. As observed by [90], the present algorithm which we call *Dynamic mode decomposition* algorithm can thus also be used to extract Ritz vectors and values from experimental data or even from a sequence of snapshots collected from nonlinear simulations. In the next section we show that in the nonlinear case the Ritz vectors approximate the Koopman modes. However, first we compare the DMD and the Arnoldi method for a linear flow.

#### 4.1.3 Example: Linearized Blasius Boundary Layer

The Arnoldi and the DMD algorithm are applied to the Navier–Stokes equations linearized about a steady Blasius boundary layer solution to demonstrate the convergence behavior of the two methods. The resulting matrix  $\mathbf{A}$  ( $n \approx 10^5$ ) is stable, i.e. the flow is globally stable but it is locally unstable to two-dimensional Tollmien–Schlichting wavepackets (see e.g. [9]). Figure 29 shows the frequency  $\omega_j$  and growth rates  $\sigma_j$  associated with the linear global eigenmode  $\boldsymbol{\phi}_j$  computed with both the Arnoldi method (red symbols) and the DMD algorithm (black and gray symbols). It is interesting to note that, although the DMD algorithm is numerically less stable than the Arnoldi algorithm, the TS-wave branch in the spectrum matches the Ritz values obtained from the Arnoldi algorithm.

The residuals  $\|\mathbf{r}_j\|$  of the Ritz vectors computed using the Arnoldi method are of order  $10^{-15}$ . For the DMD algorithm, the average residual of the Ritz vectors are shown in Fig. 30(a) as a function of the number of snapshots included in the matrix  $\mathbf{X}_r$ . Initially, there is a rapid decay with increasing snapshots, but the average residual levels out at a rather large value. As discussed previously, this is due to the fact

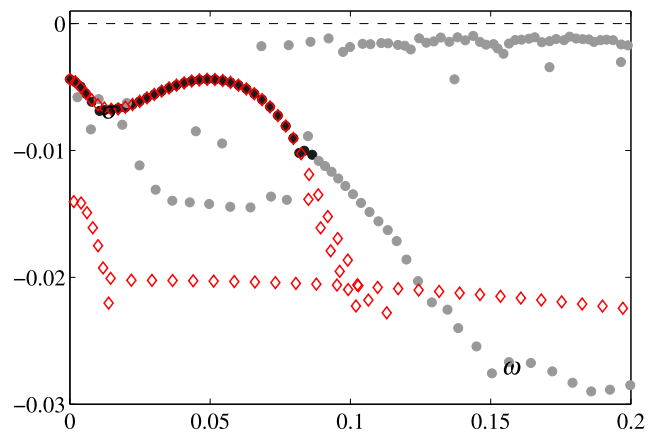


**Fig. 29** The two-dimensional global linear spectrum of the flat-plate boundary layer. Ritz values computed using the Arnoldi method (red symbol) and the DMD algorithm (black and gray symbols). DMD Ritz values that correspond to Ritz vectors with smaller magnitude than  $10^{-15}$  are shown in gray. The numerical parameters are given in Table 5 (case 2D-LIN-BL) in Sect. 4.4 (Color figure online)

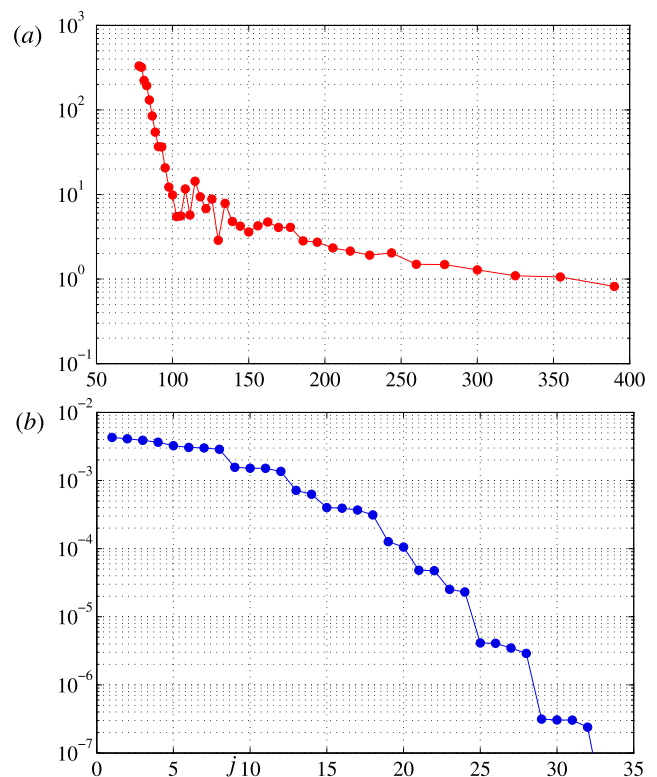


**Fig. 30** The average residuals, given by Eq. (51) as function of the number of snapshots included in  $\mathbf{X}_r$  are shown in (a). The magnitude  $a_j$  of the 32 first Ritz values computed for  $r = 390$  is shown in (b)

that the columns of  $\mathbf{X}_r$  become increasingly linearly dependent as they align with the most dominant Ritz vectors. The magnitudes  $a_j$  of the Ritz vectors from the DMD method are shown in Fig. 30(b), where—in contrast to the residuals—

a decay of several orders of magnitude is observed for first few Ritz vectors. The Ritz values obtained from the DMD algorithm that correspond to Ritz vectors with magnitudes smaller than  $10^{-15}$  are shown in gray symbols in the spectrum (Fig. 29). Thus it seems that the magnitudes (or condition numbers) of the Ritz vectors provide a way to rank the modes according to their significance; modes with very small magnitudes can be regarded as numerical noise and thus discarded.

## 4.2 Koopman Modes

The DMD algorithm described in the previous section yields Ritz vectors and values of a sequence of data without the knowledge of the system that generated the data sequence. It turns out, as first noticed by [84], that if the nonlinear system  $\mathbf{g}(\mathbf{u}_k)$  generated the sequence of data, then the Ritz vectors are approximations of Koopman modes under the map  $\mathbf{g}$ .

Let  $r$  vectors form the columns of the full-rank matrix,

$$\mathbf{X}_r = [\mathbf{a}(\mathbf{u}_0) \quad \mathbf{a}(\mathbf{u}_1) \quad \mathbf{a}(\mathbf{u}_2) \quad \dots \quad \mathbf{a}(\mathbf{u}_{r-1})] \quad (52)$$

where  $\mathbf{a}(\mathbf{u}_j)$  could be full flow field snapshots  $\mathbf{u}_j \in \mathbb{U} \subset \mathbb{R}^n$  obtained from numerical simulations or vector-valued observables  $\mathbf{a}(\mathbf{u}_j) \in \mathbb{R}^p$  from experimental measurements. By shifting the sequence with one time step, we obtain

$$\mathbf{X}_{r+1} = [\mathbf{a}(\mathbf{u}_1) \quad \mathbf{a}(\mathbf{u}_2) \quad \mathbf{a}(\mathbf{u}_3) \quad \dots \quad \mathbf{a}(\mathbf{u}_r)].$$

For a sufficiently long time series, we can assume that the  $r$ th sample  $\mathbf{a}(\mathbf{u}_r)$  is nearly linearly dependent on the previous  $r-1$  observables. Denoting the residual by  $\tilde{\mathbf{u}}_r$ , we have the following relation between the two sequences

$$\mathbf{X}_{r+1} = \mathbf{X}_r \mathbf{M} + \tilde{\mathbf{u}}_r \mathbf{e}_r^T, \quad (53)$$

where  $\mathbf{M}$  is a companion matrix. If  $\mathbf{X}_r$  is a sequence from a linear mapping  $\mathbf{A}$ , then  $\mathbf{X}_{r+1} = \mathbf{A}\mathbf{X}_r$  and we recover the DMD algorithm for computing Ritz values and vectors for linear systems. If, on the other hand, (52) is sequence of the observable  $\mathbf{a}$  on the trajectory of the system  $\mathbf{g}$  starting at the initial condition  $\mathbf{u}_0$ , then  $\mathbf{X}_{r+1}$  is given by applying the Koopman operator  $U$  on each element of this sequence

$$\begin{aligned} \mathbf{X}_{r+1} &= [U\mathbf{a}(\mathbf{u}_0) \quad U\mathbf{a}(\mathbf{u}_1) \quad U\mathbf{a}(\mathbf{u}_2) \quad \dots \quad U\mathbf{a}(\mathbf{u}_{r-1})] \\ &= U\mathbf{X}_r. \end{aligned}$$

The companion matrix for  $\mathbf{X}_r$  is uniquely determined by the direction of the residual  $\tilde{\mathbf{u}}_r$ . Similar to the previous section, we choose the elements of  $\mathbf{M}$  such that  $\tilde{\mathbf{u}}_r \perp \mathbf{X}_r$ . Now, we can define the *empirical Ritz values* of  $\mathbf{X}_r$  as the eigenvalues  $\tilde{\Lambda} = \text{diag}\{\tilde{\lambda}_0 \quad \tilde{\lambda}_1 \quad \dots \quad \tilde{\lambda}_{r-1}\}$  of  $\mathbf{M}$  associated with

## Algorithm 2 Dynamic mode decomposition

$[\tilde{\Phi}, \Lambda, r] = \text{DMD}(\mathbf{X})$

<b>Input:</b>	$r+1$ sequence of observables	$\mathbf{X} = (\mathbf{u}_1, \dots, \mathbf{u}_{r+1})$
<b>Output:</b>	$r$ empirical Ritz vectors	$\tilde{\Phi}$
	$r$ empirical Ritz values	$\Lambda$
	scalar residual	$r$

- 1:  $n = \text{size}(\mathbf{X}, 1)$
- 2:  $r = \text{size}(\mathbf{X}, 2) - 1$
- 3:  $\mathbf{u}_{r+1} = \mathbf{X}(:, r+1)$
- 4:  $\mathbf{X}_r = \mathbf{X}(:, 1:r)$
- 5:  $\mathbf{X}_{r+1} = \mathbf{X}(:, 2:r+1)$
- 6:  $\mathbf{c} = \mathbf{X}_r \setminus \mathbf{u}_{r+1}$
- 7:  $\mathbf{M} = \text{companion}(\mathbf{c})$
- 8:  $[\mathbf{T}, \Lambda] = \text{eig}(\mathbf{M})$
- 9:  $\tilde{\Phi} = \mathbf{X}_r \mathbf{T}$
- 10:  $r = \text{norm}(\mathbf{X}_{r+1} - \mathbf{X}_r \mathbf{C})$

the *empirical Ritz vectors*  $\tilde{\Phi} = [\tilde{\phi}_0 \quad \tilde{\phi}_1 \quad \dots \quad \tilde{\phi}_{r-1}]$  given by

$$\tilde{\Phi} = \mathbf{X}_r \mathbf{T} \quad (54)$$

where the columns of  $\mathbf{T}$  are the eigenvectors of  $\mathbf{M}$ . If the Ritz values are distinct, the matrix containing the left eigenvectors of the companion matrix is the Vandermonde matrix

$$\mathbf{T}^{-1} = \begin{bmatrix} 1 & \lambda_0 & \lambda_0^2 & \dots & \lambda_0^{r-1} \\ 1 & \lambda_1 & \lambda_1^2 & \dots & \lambda_1^{r-1} \\ \vdots & \vdots & & \ddots & \vdots \\ 1 & \lambda_{r-1} & \lambda_{r-1}^2 & \dots & \lambda_{r-1}^{r-1} \end{bmatrix} \in \mathbb{R}^{r \times r}. \quad (55)$$

Recall that in Sect. 2.3 the Vandermonde matrix  $\mathbf{S}$  given in (13) was identified as the expansion coefficients when expanding the sequence of observables (12) in terms of the Koopman modes  $\Phi$ , i.e.  $\mathbf{X} = \Phi \mathbf{S}$ . Similarly, we can observe that  $\mathbf{T}^{-1}$  contains the expansion coefficients when expanding the finite sequence  $\mathbf{X}_r$  in terms of the empirical Ritz vectors,  $\mathbf{X}_r = \tilde{\Phi} \mathbf{T}^{-1}$ ; each element in  $\mathbf{X}_r$  can be written as

$$\mathbf{a}(\mathbf{u}_k) = \sum_{j=0}^{r-1} \tilde{\lambda}_j^k \tilde{\phi}_j, \quad k = 0, \dots, r-1. \quad (56)$$

The empirical Ritz vector  $\tilde{\phi}_j$  thus approximates the product of the Koopman mode and the Koopman eigenfunction,  $\varphi_j(\mathbf{u}_0)\phi_j$ , and the Ritz value  $\tilde{\lambda}_j$  approximates the Koopman eigenvalue  $\lambda_j$ . Algorithm 2 applied to a set of data  $\mathbf{X}_r$  obtained from nonlinear flow provides the approximate Koopman modes and eigenvalues.

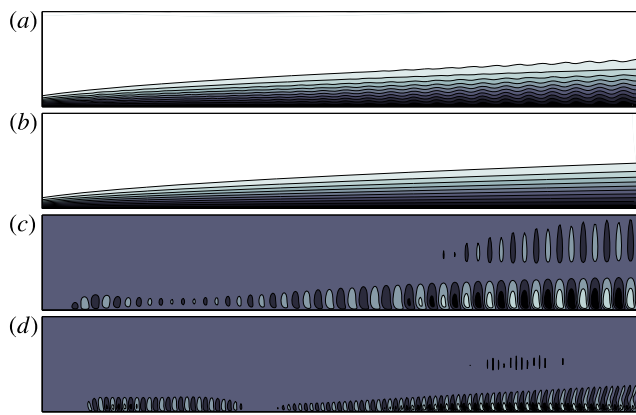


**Fig. 31** The streamwise velocity component of a snapshot from the nonlinear simulation at  $t = 85$  (a), the zeroth (b), first (c) and third (d) Koopman modes computed using the algorithm explained in Sect. 4.2

#### 4.2.1 Example: Periodically Forced Nonlinear Blasius Boundary Layer

When the sequence (52) is periodic, i.e.  $\mathbf{u}_{r-1} = \mathbf{u}_0$ , the companion matrix becomes

$$\mathbf{M} = \begin{bmatrix} 0 & 0 & \dots & 0 & 1 \\ 1 & 0 & \dots & 0 & 0 \\ 0 & 1 & \dots & 0 & 0 \\ \vdots & & \ddots & & \vdots \\ 0 & 0 & \dots & 1 & 0 \end{bmatrix} \in \mathbb{R}^{r \times r}$$

with the empirical Ritz values given by  $\lambda_k = e^{i\omega_k}$ , with  $\omega_k = 2\pi k/r$ . In this case the Vandermonde matrix  $\mathbf{T}^{-1}$  is the discrete Fourier transform matrix. This means for periodic data the Ritz vectors are Fourier modes, given by the discrete Fourier transform of the sequence.

Consider again the flow on a flat plate, where forcing is continuously applied upstream in the boundary layer with a given temporal frequency  $\omega_f = 0.036$  (non-dimensional frequency  $F = 120$ ). The amplitude of the forcing is sufficiently high to introduce a few higher harmonics. A snapshot at  $t = 85$  of the streamwise velocity component from the simulation is shown in Fig. 31(a), where we observe how the boundary layer is altered due to the periodic forcing. The snapshots ( $r = 100$ ) separated by  $\Delta t = 10$  from the simulation are stacked up in the matrix  $\mathbf{X}_r$  and its empirical Ritz values and vectors were computed using the DMD algorithm.

The Koopman modes  $\phi_0, \phi_1$  and  $\phi_3$  are shown in Fig. 31(b)–(d). The zeroth Koopman mode corresponds to the mean flow, which in this case is close to the steady Blasius boundary-layer flow. The first Koopman mode corresponds to a TS wave, where the corresponding Koopman eigenvalue  $\lambda_j$  has zero growth rate and a frequency that matches the forcing frequency  $\omega_f$  precisely. The TS wave

(Fig. 31(c)) decays in amplitude short distance downstream of the forcing location, but begins to grow exponentially at particular streamwise location (branch I) until a location further downstream (branch II). The location of branch I and II for this particular frequency matches the TS neutral curve found in the literature (see e.g. [91]). As we expect from the theory in Sect. 2.3, the first pair of Koopman modes correspond to the flow structure oscillating with the dominant frequency. The second pair of Koopman modes (one mode shown in Fig. 31(d)) correspond to the subharmonic  $2\omega_f$  frequency generated due to nonlinear interactions. This mode is also a TS wave but with a higher frequency. This simple example demonstrates how the DMD algorithm in Sect. 4.2 can be used to decompose a sequence of flow fields into spatial structures with periodic motion.

### 4.3 Balanced Modes

We turn our attention to the linear input-output system (15a)–(15b) introduced in Sect. 3. In the following, it is convenient to represent the time-continuous system matrix as  $\mathbf{A}$  and the discrete-time (i.e. time stepper) matrix as  $\mathbf{A}_\mu$  (so far in this section the subscript  $\mu$  has been omitted).

#### 4.3.1 Laub's Method

In Sect. 3.3.2 it was shown that the balanced modes are the eigenvectors of the product of the controllability Gramian  $\mathbf{P}$  (29) and observability Gramian  $\mathbf{Q}$  (30). It can be shown [31] that  $\mathbf{P}$  and  $\mathbf{Q}$  associated with the linear system (15a)–(15b) satisfy, respectively, the following *Lyapunov equations*

$$\mathbf{A}\mathbf{P} + \mathbf{P}\mathbf{A}^T + \mathbf{B}\mathbf{B}^T = 0$$

$$\mathbf{A}^T\mathbf{Q} + \mathbf{Q}\mathbf{A} + \mathbf{C}^T\mathbf{C} = 0.$$

For low and moderate dimensional systems  $n \leq 10^3$ , there are efficient direct or iterative methods for solving the Lyapunov equations [35, 95] and for computing balanced modes [57, 87].

One common way [57] of computing the balanced modes is as follows. Solve the two Lyapunov equations and compute their Cholesky factors  $\mathbf{X} \in \mathbb{R}^{n \times n}$ ,  $\mathbf{Y} \in \mathbb{R}^{n \times n}$  as

$$\mathbf{P} = \mathbf{X}\mathbf{X}^T, \quad \mathbf{Q} = \mathbf{Y}\mathbf{Y}^T$$

and compute the SVD of the  $n \times n$  matrix

$$\mathbf{Y}^T\mathbf{X} = \mathbf{U}\mathbf{\Sigma}\mathbf{V}^T. \quad (57)$$

The direct and adjoint balanced modes are then, respectively, given by

$$\mathbf{\Phi} = \mathbf{X}\mathbf{V}\mathbf{\Sigma}^{-1/2}, \quad \mathbf{\Psi} = \mathbf{Y}\mathbf{U}\mathbf{\Sigma}^{-1/2} \quad (58)$$

such that  $\Psi^T \Phi = \mathbf{I}$ . Note that  $\mathbf{X}$  and  $\mathbf{Y}$  are the numerical counterparts of the controllability operator  $\mathbf{L}_c$  and the observability operator  $\mathbf{L}_o$  defined in Sect. 3.3.1. Similarly  $\mathbf{Y}^T \mathbf{X}$  is the Hankel matrix, representing the Hankel operator  $\mathbf{\Gamma}_G$  and the diagonal matrix  $\mathbf{\Sigma}$  contains the Hankel singular values. Unfortunately, the above method is unfeasible for high-dimensional systems as the computational complexity is  $O(n^3)$  and storage requirement is  $O(n^2)$ .

#### 4.3.2 Low-Rank Cholesky Factors

Usually the number of inputs and outputs is much smaller than the state dimension,  $m, p \ll n$ . Therefore, the Gramians often have very low numerical rank  $k \ll n$  and the storage requirements can be reduced to  $O(nk)$  and computational complexity to  $O(k^3)$ . Moreover, if the purpose is model reduction, it seems imprudent to solve for all  $n$  balanced modes, to construct a reduced-order model of size  $r \ll n$ .

Consider the low-rank Cholesky factors  $\mathbf{X}_r \in \mathbb{R}^{n \times r}$  and  $\mathbf{Y}_r \in \mathbb{R}^{n \times r}$ ,

$$\mathbf{P} = \mathbf{X}_r \mathbf{X}_r^T + \mathbf{R}_P, \quad \mathbf{Q} = \mathbf{Y}_r \mathbf{Y}_r^T + \mathbf{R}_Q \quad (59)$$

where  $\mathbf{R}_P$  and  $\mathbf{R}_Q$  are residuals due to replacing the full Cholesky factors with partial ones. The SVD given in (57) can now be computed for the small  $r \times r$  matrix  $\mathbf{Y}_r^T \mathbf{X}_r = \mathbf{U}_r \mathbf{\Sigma}_r \mathbf{V}_r^T$  and subsequently  $r$  approximate balanced modes can be obtained from,

$$\Phi_r = \mathbf{X}_r \mathbf{V}_r \mathbf{\Sigma}_r^{-1/2}, \quad \Psi_r = \mathbf{Y}_r \mathbf{U}_r \mathbf{\Sigma}_r^{-1/2}. \quad (60)$$

The question is, how close  $\Phi_r$  and  $\Psi_r$  using low-rank Cholesky factors are to the “true” balanced modes  $\Phi$  and  $\Psi$  using full-rank factors. Are the two important properties (stability and tight error bounds) of the balanced reduced-model preserved when computed by  $\Phi_r$  and  $\Psi_r$ ? Antoulas [7] derives non-trivial estimates of the residuals given in (59). In general, numerical tests [1, 9, 10, 44] show that  $\Phi_r$  is a good approximation and that  $\mathbf{\Sigma}_r$  are close to the true HSV. This can be attributed, as mentioned earlier, to the low numerical rank of the Gramians, when  $m, p \ll n$ . Unfortunately, stability of the reduced-model is no longer guaranteed when using  $\mathbf{X}_r$ . Note that  $\mathbf{A}_r$  is stable if  $\mathbf{A}_r^T \mathbf{M} + \mathbf{M} \mathbf{A}_r + \mathbf{N} = 0$  has a solution for any  $\mathbf{N} = \mathbf{N}^T > 0$  and  $\mathbf{M} = \mathbf{M}^T > 0$ . One can derive (see e.g. [7]),

$$\mathbf{A}_r \mathbf{\Sigma}_r + \mathbf{\Sigma}_r \mathbf{A}_r^T + \mathbf{B}_r \mathbf{B}_r^T + \Psi_r^T (\mathbf{A} \mathbf{R}_P + \mathbf{R}_P \mathbf{A}^T) \Psi_r = 0$$

where the additional term due to the residuals is not necessarily positive definite.

We have thus dealt with the high-dimensionality problem if we can find low-rank Cholesky factors. The reduced-order model  $\mathbf{G}_r$  can be computed for very large system using Algorithm 3. Various methods may be used to find  $\mathbf{X}_r$ ,

#### Algorithm 3 Balanced reduced model

$[\mathbf{G}_r, e_l, e_u] = \text{balmodes}(\mathbf{X}_r, \mathbf{Y}_r)$

**Input:** low-rank Cholesky factor of  $\mathbf{P}$   $\mathbf{X}_r$   
low-rank Cholesky factor of  $\mathbf{Q}$   $\mathbf{Y}_r$   
**Output:** linear reduced-order model  $\mathbf{G}_r = (\mathbf{A}_r, \mathbf{B}_r, \mathbf{C}_r)$   
lower theoretical error bound  $e_l$   
upper theoretical error bound  $e_u$

1:  $[\mathbf{U}, \mathbf{\Sigma}, \mathbf{V}] = \text{SVD}(\mathbf{Y}_r^T \mathbf{X}_r)$   
2:  $\Phi = \mathbf{X}_r \mathbf{V} \mathbf{\Sigma}^{-1/2}$   
3:  $\Psi = \mathbf{Y}_r \mathbf{U} \mathbf{\Sigma}^{-1/2}$   
4:  $\mathbf{A}_r = \Psi^T \mathbf{A} \Phi$   
5:  $\mathbf{B}_r = \Psi^T \mathbf{B}$   
6:  $\mathbf{C}_r = \mathbf{C} \Phi$   
7:  $e_l = \mathbf{\Sigma}(r+1, r+1)$   
8:  $e_u = 2(\text{sum}((r+1:\text{end}, r+1)))$

and  $\mathbf{Y}_r$ : ADI/Smith methods [34, 76], snapshot-based methods [54, 83] and Krylov subspace methods [45]. As was observed by Sorensen & Rowley (private communication), there exists a close connection between Smith-type of methods and snapshot-based methods. The former is an iterative process aiming directly at solving the Lyapunov equation and requiring the knowledge of  $\mathbf{A}$ . The snapshot-based method on the other hand computes low-rank Cholesky factors directly from the definition of the Gramians, where the integrals are approximated by numerical simulations of the linear system.

#### 4.3.3 Snapshot-Based Method

We describe the snapshot-based method [83] for computing the low-rank Cholesky factor  $\mathbf{X}_r$  of the controllability Gramian  $\mathbf{P}$ . To obtain the factor  $\mathbf{Y}_r$  of the observability Gramian  $\mathbf{Q}$ , the method is applied to the dual input-output system, defined by

$$\mathbf{G}^* = \left( \begin{array}{c|c} \mathbf{A}^T & \mathbf{C}^T \\ \hline \mathbf{B}^T & 0 \end{array} \right).$$

Comparing the above dual equations with (18) we observe that the output and input matrices have exchanged place; the state is now forced with the adjoint of  $\mathbf{C}$  and the output is given by the adjoint of  $\mathbf{B}$ . Note that  $\mathbf{A}^T$  represents the discretized adjoint Navier–Stokes equations (see [10], for a thorough derivation of the dual system). This is a dual problem to  $\mathbf{G}$  (18), in the sense that the controllability Gramian of  $\mathbf{G}^*$  is equal to the observability Gramian of  $\mathbf{G}$ .

Suppose that we have  $p$  constant input vectors,

$$\mathbf{B} = [\mathbf{B}_1 \quad \dots \quad \mathbf{B}_p] \in \mathbb{R}^{n \times p}$$

associated with the input signals

$$\mathbf{w}(t) = [w_1(t) \quad \dots \quad w_p(t)] \in \mathbb{R}^{p \times 1}.$$

When  $w_j = \delta(t)$  and  $\mathbf{u}_0 = 0$ , the state at any time is given by,

$$\mathbf{u}_j(t) = e^{A^t} \mathbf{B}_j.$$

The controllability Gramian can thus be written as a sum of impulse responses to  $p$  inputs,

$$\mathbf{P} = \int_0^\infty e^{A^t} \mathbf{B} \mathbf{B}^T e^{A^T t} dt = \int_0^\infty \sum_{j=1}^p \mathbf{u}_j(t) \mathbf{u}_j(t)^T dt.$$

Define the *empirical controllability Gramian* as the quadrature approximation of  $\mathbf{P}$ ,

$$\tilde{\mathbf{P}}_r = \sum_{j=1}^r \sum_{i=1}^p \mathbf{u}_i(t_j) (\mathbf{u}_i(t_j))^T \delta_j = \mathbf{X}_r \mathbf{X}_r^T,$$

where the Cholesky factor  $\mathbf{X}_r \in \mathbb{R}^{n \times pr}$  is given by

$$\mathbf{X}_r = [\mathbf{u}_1(t_1)\sqrt{\delta_1} \quad \dots \quad \mathbf{u}_1(t_r)\sqrt{\delta_r} \quad \dots \\ \mathbf{u}_p(t_1)\sqrt{\delta_1} \quad \dots \quad \mathbf{u}_p(t_m)\sqrt{\delta_r}] \quad (61)$$

and  $\delta_j$  are the quadrature coefficients (for example resulting from a trapezoidal rule). To compute  $\mathbf{X}_r$ , one needs to perform  $p$  numerical simulations of the linear system. For each simulation  $r$  snapshots are collected, which results in memory requirements of the order  $O(npr)$  to store the Cholesky factor.

To obtain the factor  $\mathbf{Y}_r$  of the observability Gramian  $\mathbf{Q}$ , the above method is applied to the dual input-output system. Suppose

$$\mathbf{z}_j(t) = e^{A^T t} \mathbf{C}_j^T, \quad j = 1, \dots, m$$

is the impulse response of the adjoint system to output vector  $\mathbf{C}_j^T$ . Then the *empirical observability Gramian* is

$$\tilde{\mathbf{Q}}_r = \sum_{j=1}^r \sum_{i=1}^m \mathbf{z}_i(t_j) (\mathbf{z}_i(t_j))^T \delta_j = \mathbf{Y}_r \mathbf{Y}_r^T.$$

Similarly,  $\mathbf{Y}_r \in \mathbb{R}^{n \times mr}$  is obtained by  $m$  numerical simulations of the adjoint system,

$$\mathbf{Y}_r = [\mathbf{z}_1(t_1)\sqrt{\delta_1} \quad \dots \quad \mathbf{z}_1(t_m)\sqrt{\delta_m} \quad \dots \\ \mathbf{z}_m(t_1)\sqrt{\delta_1} \quad \dots \quad \mathbf{z}_m(t_r)\sqrt{\delta_r}]. \quad (62)$$

The snapshot method to compute Cholesky factors thus amounts to collecting snapshots from  $p$  simulations of the forward linear system and  $m$  simulation of the adjoint system. In this way, we trade the storage of very large matrices for numerical simulations.

A few remarks on the method are noteworthy. As shown by [63] a theoretical equivalence between snapshot-based

balanced truncation and a system identification technique called eigensystem realization algorithm (ERA) [48] exists. Unlike the snapshot-based method, ERA does not require the dual system (adjoint simulations) and the oblique projection onto a set of balanced modes is not performed. The method is significantly cheaper than the snapshot method; the main disadvantage is that it does not provide a set of global balanced modes, which can be useful for physical insight into the input-output properties of the linear system.

For more complex three-dimensional configurations, the number of inputs and output may become of the order  $p, m \in O(10^2)$  and a large number of snapshots  $r \in O(10^3)$  must be collected if there are slowly decaying modes that pulsate with different frequencies. As a consequence the storage requirement for each Cholesky factor is demanding and the SVD to compute the approximate balanced modes might become computationally intractable. Moreover, many inputs and outputs may have the same spatial structure and are located close to each other. This is the situation for actuators and sensors in the three-dimensional set-up sketched in Fig. 20. In such cases, the states triggered by the impulse response of each input/output do not differ significantly from each other. As a consequence the factors  $\mathbf{X}_r, \mathbf{Y}_r$  become gradually ill-conditioned for increasing number of snapshots, since the columns are nearly linearly dependent. There is remedy for very large and ill-conditioned Cholesky factors as first addressed by [34] for the so called modified Smith's method. However, the "modified" method also applies to the method of snapshot for computing low-rank Cholesky factors.

#### 4.4 Time Stepping

The methods presented to compute global modes are all "matrix-free" and based on flow field snapshots. These snapshots are obtained by abstract notion of a time stepper  $\mathbf{g}$ ,

$$\mathbf{u}_{k+1} = \mathbf{g}(\mathbf{u}_k). \quad (63)$$

In practice, the implementation of a validated, three-dimensional and efficient time-stepper to solve the time-dependent nonlinear Navier–Stokes equations is a formidable task to undertake. The Navier–Stokes equations given by (1a)–(1b) can be solved by splitting the task into a number of subproblems. Examples of subproblems are a scheme for time advancement, method for spatial discretization and how to address the pressure term in the Navier–Stokes equations (since an evolution equation for the pressure is missing in explicit form, the equations are not fully parabolic in time). Moreover, the choice of numerical method for each subproblem depends on the complexity of the geometry, numerical accuracy, efficiency, ability to parallelize etc. For example, even small modifications of a highly efficient parallelized Fortran implementation, where the different subproblems

are tightly coupled might turn out to be very time consuming and prone to errors. In other cases, flexible codes for example implemented using object-oriented design, makes the switch between different equations (linear, nonlinear, adjoint) simple and advanced algorithms (for computing global modes, steady solutions) can easily be “wrapped” around the code.

#### 4.4.1 Overview of Pseudo-Spectral Code

Essentially, all the results presented in this paper are based on an existing simulation code called Simson. The main structure of the code and the simulation parameters are given in the following. For details, the reader is referred to the comprehensive user guide [19].

The approach adopted in the Simson code, is based on pressure-free formulation of the Navier–Stokes equation (1a)–(1b). By applying the Laplace and curl operators to the momentum equations given by Eq. (1a), the Navier–Stokes equations in primitive variables  $\mathbf{u} = (u, v, w)$  can be replaced with a nonlinear advection-diffusion equation, describing quantities related to the wall-normal component of the velocity and vorticity.

The Simson code implements a spectral algorithm, where the solution is approximated by an expansion in Fourier functions in the wall-parallel directions ( $x, z$ ) and Chebyshev polynomials in the wall-normal direction ( $y$ ). In the so called pseudo-spectral approach, the nonlinear advection term is computed by forming products in physical space, whereas the linear diffusion term is computed in Fourier space. Therefore, efficient transformations between physical and spectral space are performed at each time-step using FFT routines and aliasing errors from the evaluation of the nonlinear terms are removed by the 3/2-rule. For sufficiently smooth velocity fields, the spectral approach is a significantly more accurate approximation compared to other discretization methods, such as finite difference or finite element. To preserve the spectral accuracy however, mapping of grid-points cannot be applied, and therefore more complex geometries are difficult (and inefficient) to model. The time advancement is a four-step third-order Runge-Kutta method for the nonlinear advection term, and a second-order Crank-Nicolson method the linear diffusion term.

#### 4.4.2 Boundary Conditions

Fourier expansion in the wall-parallel directions requires periodic boundary conditions in  $x$  and  $z$ , i.e.

$$\begin{aligned} \mathbf{u}(0, y, z) &= \mathbf{u}(L_x, y, z), \\ \mathbf{u}(x, y, -L_z/2) &= \mathbf{u}(x, y, L_z/2). \end{aligned} \quad (64)$$

However, since neither the boundary-layer flow nor the jet in crossflow are periodic in the streamwise direction  $x$ ,

a “fringe” region can be added at the downstream end of the computational box. In this region, the forcing function

$$F(\mathbf{u}) = \lambda_f(x)(\mathbf{v} - \mathbf{u}), \quad (65)$$

is applied. The desired inflow velocity is denoted by  $\mathbf{v}$ , which for simulations of boundary layer and the jet in crossflow is chosen as the laminar Blasius boundary-layer profile. The fringe function  $\lambda_f(x)$  is identically zero inside the physically relevant domain, and raises smoothly to order one inside the fringe region. The length of the region with  $\lambda_f > 0$  is about 20 % of the complete domain length. The fringe forcing has been thoroughly validated and we refer to [72] for details on the convergence properties and upstream influence of the method. The computation of the linear global eigenmodes is slightly dependent on the fringe (shape of the forcing and position). As discussed by [3] the growth rate of individual damped eigenvalues might depend on the outflow boundary condition. Moreover, there are also additional modes in the global spectrum related to the fringe forcing. However, these changes have been observed in the damped part of the spectrum; due to the nature of the fringe forcing, there is no growing fringe eigenmode to be expected.

For the simulation of disturbances evolving in the boundary layer, homogeneous no-slip condition is prescribed on the flat plate ( $y = 0$ ). Far away from the wall, in the free-stream the perturbation velocity is vanishingly small, where a Dirichlet boundary condition can be imposed. The boundary conditions in the wall-normal direction for the jet in crossflow are as follows. On the flat plate, no-slip conditions for the wall-parallel velocity components  $u$  and  $w$  are prescribed. The jet discharging into the crossflow is imposed by a wall-normal velocity

$$v(r, y = 0) = \frac{V_{\text{jet}}}{U_\infty} (1 - r^2) \exp(-(r/0.7)^4),$$

with  $r$  being the distance from the jet center ( $x_{\text{jet}}, z_{\text{jet}}$ ), normalized by half the jet diameter  $D$ . This inflow profile corresponds to a (laminar) parabolic velocity profile of the pipe flow, smoothed with a super-Gaussian function to allow for an efficient treatment with the spectral discretization of the simulation code. At top boundary of the computational box  $y = L_y$  the following Neumann condition is imposed,

$$\frac{\partial \mathbf{u}}{\partial y} \Big|_{y=L_y} = \frac{\partial \mathbf{U}}{\partial y} \Big|_{y=L_y}, \quad (66)$$

where  $\mathbf{U}(x, y)$  is a Blasius solution.

In Table 5 the parameters of the simulations performed in this paper are listed.

## 5 Conclusions

This section contains an overview of the results and a few suggestions for future work.

**Table 5** Parameters of the numerical simulations performed in this paper. For all simulations the fringe region is 20 % of the length of the domain ( $L_x$ )

Case	$Re_{\delta_0}^*$	Box ( $L_x, L_y, L_z$ )	Grid ( $n_x, n_y, n_z$ )	B.C. $y = 0/y = L_y$
JCF	165	(75, 20, 30)	(256, 201, 144)	Parabolic/Neumann
2D-LIN-BL	$10^3$	(1000, 30, 1)	(768, 101, 1)	No-slip/Dirichlet
3D-LIN-BL	$10^3$	(1000, 30, 370)	(768, 101, 120)	No-slip/Dirichlet
3D-NLIN-BL	$10^3$	(1000, 30, 250)	(768, 101, 256)	No-slip/Neumann

### 5.1 Analysis of Complex Flows

For complex flow configurations, assumptions like periodicity in a direction, a separation in space or time between the development of perturbations and the basic flow and other similar simplifications are not obvious to make. In many applications, there are a number of flow mechanisms and dynamic structures developing at different temporal and spatial scales. Moreover, the various structures might be tightly coupled, competing and interacting with each other. To get a complete picture of the dynamical structures that are present and their significance to the overall flow, it is necessary to adopt a global viewpoint.

The work presented here is among the first to apply a linear and a nonlinear analysis, using tools that have a theoretical foundation, to a fully three dimensional and highly unsteady flow, namely the jet in crossflow. In practice, the analysis is performed by the use of DNS in conjunction with “matrix-free” techniques from numerical linear algebra (e.g. Arnoldi and DMD). The work on the jet in crossflow can be considered as a “proof-of-concept” as it shows that is possible and numerically feasible to perform linear and nonlinear analysis of complex flows without making a number of simplifications on the geometry, the fluid properties or the flow parameters.

In the study performed here, the unsteady dynamics of the jet in crossflow was broken into two parts; the linear stability analysis of the steady flow and the nonlinear attractor analysis of the unsteady flow. The results and physical insights gained can be summarized as follows. Analysis of the computed global eigenmodes and the unstable steady solution of the jet in crossflow at a velocity ratio  $R = 3$  have revealed the presence of three types of elementary instabilities: elliptic instability; Kelvin-Helmholtz instability and a von Kármán type of instability. These instabilities have been studied extensively on simple canonical flows, and it is important to identify them in more complex flows, since they provide an understanding of the elementary physical mechanism for perturbation growth. This knowledge is indispensable for the modification of the flow behavior by external means, since the perturbations are responsible for the initial stage of the transition between different flow regimes.

In flows exhibiting vortex shedding, identifying precisely where in the domain the oscillations have a significant effect is useful both for the physical understanding and for

applications. For the jet in crossflow, placing probes in single points in the domain gave supporting evidence of two distinct sustained global oscillations: one high-frequency associated with the jet flow and one low-frequency associated with the wall region. However, probe placement is a local analysis, and collecting spectral data of each relevant spatial point in a three-dimensional domain is an impossible task. In this work, we have presented a method based on spectral analysis of the Koopman operator—that can be applied to experimental data as well—to extract global flow structures with periodic motion. The analysis identified a shear mode and wall mode corresponding to the high and low oscillations respectively.

There exists a number of future research directions. We outline a few examples.

*Sensitivity Analysis and Passive Control* Recent theoretical results [28] show that much physical insight can be gained by investigating the sensitivities of various flow properties to different parameters. The methods have their roots in calculus of variations and generally involve adjoint-based analysis and optimization. By solving the adjoint equations we can locate regions where the flow is most sensitive to forcing and we can compute the perturbations that are the most dangerous to the flow.

*Oscillator Versus Amplifier Region* Absolute and convective instabilities are local concepts applicable to weakly non-parallel flows and is not straight-forward to conduct such an analysis for the jet in crossflow. However, due to the fact that globally unstable flows have a region or pocket of local absolute instability somewhere in the flow [22] and that this pocket is connected to a region of significant backflow [36], it is likely that the separated region acts as an oscillator in the jet in crossflow. A local analysis of the steady solution could reveal regions in the flow that act as oscillators and regions that act as amplifiers.

*Bifurcation Analysis* We have performed linear global stability analysis of a steady solution of the jet in crossflow at a single velocity ratio. To fully understand the type of bifurcation that the flow undergoes, a more encompassing global stability analysis of the jet in crossflow, where the velocity ratio is varied should be performed. If the critical velocity ratio is found, a weakly nonlinear analysis could be

employed by tracing a global instability in time from its inception through its small-amplitude linear stage to saturation in order to evaluate the coefficients of the Landau equation.

*Koopman Modes of the Transient Regime* The theory based on the Koopman operator presented in this work considered the asymptotic nonlinear dynamics, whereas the linear analysis considered the dynamics in a small neighborhood of the steady solution. In the transition from a steady to unsteady flow, the transient time from the unstable fixed point to the attractor has not been considered. It could be possible to incorporate the spectral theory of the Koopman operator to account for this regime. An accurate description of the transient regime using global modes is important for reduced-order modeling of globally unstable flows [71].

## 5.2 Laminar-Turbulent Transition Delay

Many aspects in flow control have traditionally been based on intuition and physical insight into the specific flow configuration. There are a number of situations where this approach has proven successful. Nevertheless, there is a well established theory and a large number of methods for a more systematic approach to flow control. The advantages are that even small improvements in the control performance in many applications may have important consequences. For instance, the world-wide shipping consumes over 2.1 billion barrels of oil per year and the airline industry consumes more than 1.5 billion barrels per year. Finding the best possible solution, given certain constraints, that results in a few percents increase of performance can save a lot of money and resources. The work presented hereing takes us one step closer to incorporating theoretical tools into the flow control community.

The starting point of modern optimal and robust control design is an input-output formulation. Given the physical distribution of the inputs and outputs, the control design process amounts to the determination of input signals when output signals are given. Therefore, for successful control design it is sufficient to capture only a fraction of the dynamics, namely the relationships between the input and output signals. We have built a model of low dimension that captures the input-output behavior of the flat-plate boundary layer, and used this model for optimal feedback control design. We have shown that by using systematic methods from control theory in combination with localized sensing/actuation, it is possible to reduce the growth of small-amplitude disturbances in the boundary layer. It was demonstrated that the energy of two and three-dimensional disturbances are damped by an order of magnitude.

Although the significance of the order-of-magnitude reduction of perturbation energy for transition control remains to be tested, such a drastic energy reduction is likely to result in a delay of the initial stages of the transition process. If

the actuators and sensors represent realistic models of physically implementable devices, it is possible to use the low-dimensional controller designed numerically in laboratory experiments. The fact that we have modeled the inputs and outputs as volume forcing does not mean that they are unrealistic (see [9], for a similar analysis, but instead of volume forcing, the actuators are in homogeneous boundary conditions). It is the effect of an actuator that is important to model, and not the actuator itself. Therefore, the action that the volume forcing has on the flow, could possibly be reproduced for example using plasma actuators. Another issue that needs to be taken into account is control robustness. If the numerically-designed controller is used in laboratory experiments, it is unavoidable that some parameters (such as Reynolds number and pressure gradients) will mismatch. Fortunately, modern developments in robust control theory take rigorously into account uncertainties that may be present in the design process. The method for optimal control presented in this context, can be incorporated into a robust control framework. Another way that numerical investigations can be useful for wind-tunnel experiments, is by providing guidelines for the shape and spatial distribution of actuators and sensors. In this sense, one can set-up experiments after evaluating a large number of numerical simulations, in order to understand how to design and place actuators and sensors.

We have focused on the flat-plate geometry which still poses a computational challenge, however, the flow control techniques presented here do not rely on physical insight into the specific flow configuration and can in principle be applied to any geometry. A similar analysis on more complex flows, such as flows in ducts, corners, diffusers and on elliptic leading edges are waiting to be undertaken.

**Acknowledgements** I wish to thank Dan Henningson, Philipp Schlatter and Luca Brandt at KTH for the countless discussions and great ideas. Thanks to Peter Schmid and Clancy Rowley for my stays in LadHyx/Ecole Polytechnique and Princeton, where part of this work was performed. Financial support by the Swedish Research Council (VR-DNR 2010-3910) and computer time from the Swedish National Infrastructure for Computing (SNIC) is gratefully acknowledged.

## References

1. Ahuja S (2009) Reduction methods for feedback stabilization of fluid flows. PhD thesis, Princeton University, New Jersey
2. Åkervik E, Brandt L, Henningson DS, Høpfner J, Marxen O, Schlatter P (2006) Steady solutions of the Navier-Stokes equations by selective frequency damping. *Phys Fluids* 18(068102):1–4
3. Åkervik E, Ehrenstein U, Gallaire F, Henningson DS (2008) Global two-dimensional stability measures of the flat plate boundary-layer flow. *Eur J Mech B, Fluids* 27:501–513
4. Åkervik E, Høpfner J, Ehrenstein U, Henningson DS (2007) Optimal growth, model reduction and control in a separated boundary-layer flow using global eigenmodes. *J Fluid Mech* 579:305–314

5. Alam M, Sandham ND (2000) Direct numerical simulation of laminar separation bubbles with turbulent reattachment. *J Fluid Mech* 403:223–250. doi:[10.1017/S0022112099007119](https://doi.org/10.1017/S0022112099007119)
6. Anderson B, Moore J (1990) Optimal control: linear quadratic methods. Prentice Hall, New York
7. Antoulas CA (2005) Approximation of large-scale dynamical systems. SIAM, Philadelphia
8. Arnoldi WE (1951) The principle of minimized iterations in the solution of the matrix eigenvalue problem. *Q Appl Math* 9:17–29
9. Bagheri S, Åkervik E, Brandt L, Henningson DS (2009) Matrix-free methods for the stability and control of boundary layers. *AIAA J* 47:1057–1068
10. Bagheri S, Brandt L, Henningson DS (2009) Input-output analysis, model reduction and control design of the flat-plate boundary layer. *J Fluid Mech* 620:263–298
11. Bagheri S, Høpfner J, Schmid PJ, Henningson DS (2009) Input-output analysis and control design applied to a linear model of spatially developing flows. *Appl Mech Rev* 62(2). doi:[10.1115/1.3077635](https://doi.org/10.1115/1.3077635)
12. Bagheri S, Schlatter P, Schmid PJ, Henningson DS (2009) Global stability of a jet in crossflow. *J Fluid Mech* 624:33–44
13. Barkley D (2006) Linear analysis of the cylinder wake mean flow. *Europhys Lett* 75:750–756
14. Barkley D, Gomes MG, Henderson RD (2002) Three-dimensional instability in flow over a backward-facing step. *J Fluid Mech* 473:167–190
15. Batchelor G (1967) An introduction to fluid dynamics. Cambridge University Press, Cambridge
16. Bewley TR (2001) Flow control: new challenges for a new renaissance. *Prog Aerosp Sci* 37:21–58
17. Bewley TR, Liu S (1998) Optimal and robust control and estimation of linear paths to transition. *J Fluid Mech* 365:305–349
18. Blasius P (1908) Grenzschichten in flüssigkeiten mit kleiner reibung. *Z Angew Math Phys* 56(1)
19. Chevalier M, Schlatter P, Lundbladh A, Henningson DS (2007) A pseudo spectral solver for incompressible boundary layer flows. *Trita-Mek 7*, KTH Mechanics, Stockholm, Sweden (2007)
20. Chomaz JM (2005) Global instabilities in spatially developing flows: non-normality and nonlinearity. *Annu Rev Fluid Mech* 37:357–392
21. Chomaz JM, Huerre P, Redekopp LG (1987) Models of hydrodynamic resonances in separated shear flows. In: 6th symposium on turbulent shear flows, Toulouse, France
22. Chomaz JM, Huerre P, Redekopp LG (1991) A frequency selection criterion in spatially developing flows. *Stud Appl Math* 84:114–119
23. Ding J (1998) The point spectrum of Frobenius-Perron and Koopman operators. *Proc Am Math Soc* 126(5):1355–1361
24. Doyle JC (1978) Guaranteed margins for LQG regulators. *IEEE Trans Autom Control* 23:756–757
25. Doyle JC, Glover K, Khargonekar PP, Francis BA (1989) State-space solutions to standard  $H_2$  and  $H_\infty$  control problems. *IEEE Trans Autom Control* 34:831–847
26. Dullerud EG, Paganini F (1999) A course in robust control theory. A convex approach. Springer, New York
27. Fric TF, Roshko A (1994) Vortical structure in the wake of a transverse jet. *J Fluid Mech* 279:1–47
28. Giannetti F, Luchini P (2007) Structural sensitivity of the first instability of the cylinder wake. *J Fluid Mech* 581:167–197
29. Glover K (1984) All optimal Hankel-norm approximations of linear multivariable systems and the  $l^\infty$ -error bounds. *Int J Control* 39:1115–1193
30. Goldstein ME, Hultgren LS (1989) Boundary-layer receptivity to long-wave free-stream disturbances. *Annu Rev Fluid Mech* 21(1):137–166. doi:[10.1146/annurev.fl.21.010189.001033](https://doi.org/10.1146/annurev.fl.21.010189.001033)
31. Green M, Limebeer JN (1995) Linear robust control. Prentice Hall, New Jersey
32. Grundmann S, Tropea C (2008) Active cancellation of artificially introduced Tollmien–Schlichting waves using plasma actuators. *Exp Fluids* 44(5):795–806
33. Guckenheimer J, Holmes P (1983) Nonlinear oscillations, dynamical system and bifurcations of vector fields. Springer, New York
34. Gugercin S, Sorensen D, Antoulas A (2003) A modified low-rank Smith method for large-scale Lyapunov equations. *Numer Algorithms* 32:27–55
35. Hammarling SJ (1982) Numerical solution of the stable, non-negative definite Lyapunov equation. *IMA J Numer Anal* 2:303–323
36. Hammond DA, Redekopp LG (1998) Local and global instability properties of separation bubbles. *Eur J Mech B, Fluids* 17(2):145–164. doi:[10.1016/S0997-7546\(98\)80056-3](https://doi.org/10.1016/S0997-7546(98)80056-3). <http://www.sciencedirect.com/science/article/B6VKX-3W292RM-8/230F93c37bb57766823fe70d504e7dab>
37. Hammond EP, Bewley TR, Moin P (1998) Observed mechanisms for turbulence attenuation and enhancement in opposition-controlled wall-bounded flows. *Phys Fluids* 10(9):2421–2423. doi:[10.1063/1.869759](https://doi.org/10.1063/1.869759). <http://link.aip.org/link/?PHF/10/2421/1>
38. Henningson DS, Åkervik E (2008) The use of global modes to understand transition and perform flow control. *Phys Fluids* 20(031):302
39. Ho CM, Tai Y (1998) Micro-electro-mechanical systems MEMS and fluid flows. *Annu Rev Fluid Mech* 30:579–612
40. Holmes P, Lumley J, Berkooz G (1996) Turbulence coherent structures dynamical systems and symmetry. Cambridge University Press, Cambridge
41. Huerre P (2000) Open shear flow instabilities. In: Perspectives in fluid dynamics. Cambridge University Press, Cambridge, pp 159–229
42. Huerre P, Monkewitz P (1990) Local and global instabilities in spatially developing flows. *Annu Rev Fluid Mech* 22:473–537
43. Huerre P, Monkewitz PA (1985) Absolute and convective instabilities in free shear layers. *J Fluid Mech* 159:151–168. doi:[10.1017/S0022112085003147](https://doi.org/10.1017/S0022112085003147)
44. Ilak M, Rowley CW (2008) Modeling of transitional channel flow using balanced proper orthogonal decomposition. *Phys Fluids* 20(034):103
45. Jaimoukha IM, Kasenally EM (1994) Krylov subspace methods for solving large Lyapunov equations. *SIAM J Numer Anal* 31(1):227–251. <http://www.jstor.org/stable/2158160>
46. Jeong J, Hussain F (1995) On the identification of a vortex. *J Fluid Mech* 285:69–94
47. Jovanovic MR, Bamieh B (2005) Componentwise energy amplification in channel flows. *J Fluid Mech* 534:145–183
48. Juang J, Pappa RS (1985) An eigensystem realization algorithm for modal parameter identification and model reduction. *J Guid Control Dyn* 3(25):620–627
49. Kalman RE (1960) A new approach to linear filtering and prediction problems. *Trans ASME J Basic Eng* 82:24–45
50. Kelso R, Lim T, Perry A (1996) An experimental study of round jets in cross-flow. *J Fluid Mech* 306:111–144
51. Kelso RM, Smits AJ (1995) Horseshoe vortex systems resulting from the interaction between a laminar boundary layer and a transverse jet. *Phys Fluids* 7(1):153–158. doi:[10.1063/1.868736](https://doi.org/10.1063/1.868736). <http://link.aip.org/link/?PHF/7/153/1>
52. Kim J, Bewley TR (2007) A linear systems approach to flow control. *Annu Rev Fluid Mech* 39:383–417
53. Koopman B (1931) Hamiltonian systems and transformations in Hilbert space. *Proc Natl Acad Sci USA* 17:315–318
54. Lall S, Marsden JE, Glavaski S (2002) A subspace approach to balanced truncation for model reduction of nonlinear control systems. *Int J Robust Nonlinear Control* 12:519–535

55. Laporte F, Corjon A (2000) Direct numerical simulations of the elliptic instability of a vortex pair. *Phys Fluids* 12(5):1016–1031. doi:[10.1063/1.870357](https://doi.org/10.1063/1.870357). <http://link.aip.org/link/?PHF/12/1016/1>
56. Lasota A, Mackey CM (1994) *Chaos, fractals and noise: stochastic aspects of dynamics*. Springer, New York
57. Laub A, Heath M, Paige C, Ward R (1987) Computation of system balancing transformations and other applications of simultaneous diagonalization algorithms. *IEEE Trans Autom Control* 32(2):115–122
58. Lehoucq RB, Sorensen DC, Yang C (1998) *ARPACK users' guide: solution of large-scale eigenvalue problems with implicitly restarted Arnoldi methods*. SIAM, Philadelphia
59. Leweke T, Williamson CHK (1998) Cooperative elliptic instability of a vortex pair. *J Fluid Mech* 360:85–119. doi:[10.1017/S0022112097008331](https://doi.org/10.1017/S0022112097008331)
60. Lewis FL, Syrmos LV (1995) *Optimal control*. Wiley, New York
61. Lim TT, New TH, Luo SC (2001) On the development of large-scale structures of a jet normal to a cross flow. *Phys Fluids* 13(3):770–775. doi:[10.1063/1.1347960](https://doi.org/10.1063/1.1347960). <http://link.aip.org/link/?PHF/13/770/1>
62. Lumley JL (1970) *Stochastic tools in turbulence*. Academic Press, New York
63. Ma Z, Ahuja S, Rowley CW (2011) Reduced order models for control of fluids using the eigensystem realization algorithm. *Theor Comput Fluid Dyn* 25(1–4):233–247. doi:[10.1007/s00162-010-0184-8](https://doi.org/10.1007/s00162-010-0184-8)
64. Marquillie M, Ehrenstein U (2002) On the onset of nonlinear oscillations in a separating boundary-layer flow. *J Fluid Mech* 458:407–417
65. Mezić I (2005) Spectral properties of dynamical systems, model reduction and decompositions. *Nonlinear Dyn* 41(1):309–325
66. Mezić I, Banaszuk A (2004) Comparison of systems with complex behavior. *Physica D* 197(1–2):101–133
67. Milling W (1981) Tollmien–Schlichting wave cancellation. *Phys Fluids* 24(5):979–981
68. Monkewitz PA, Bechert DW, Barsikow B, Lehmann B (1990) Self-excited oscillations and mixing in a heated round jet. *J Fluid Mech* 213:611–639. doi:[10.1017/S0022112090002476](https://doi.org/10.1017/S0022112090002476)
69. Moore B (1981) Principal component analysis in linear systems: controllability, observability, and model reduction. *IEEE Trans Autom Control* 26(1):17–32
70. Moussa ZM, Trischka JW, Eskinazi S (1977) The near field in the mixing of a round jet with a cross-stream. *J Fluid Mech* 80(01):49–80. doi:[10.1017/S0022112077001530](https://doi.org/10.1017/S0022112077001530)
71. Noack B, Afanasiev K, Morzynski M, Tadmor G, Thiele F (2003) A hierarchy of low-dimensional models for the transient and post-transient cylinder wake. *J Fluid Mech* 497:335–363
72. Nordström J, Nordin N, Henningson DS (1999) The fringe region technique and the fourier method used in the direct numerical simulation of spatially evolving viscous flows. *SIAM J Sci Comput* 20(4):1365–1393
73. Packard NH, Crutchfield JP, Farmer JD, Shaw RS (1980) Geometry from a time series. *Phys Rev Lett* 45(9):712–716. doi:[10.1103/PhysRevLett.45.712](https://doi.org/10.1103/PhysRevLett.45.712)
74. Pang J, Choi KS (2004) Turbulent drag reduction by lorentz force oscillation. *Phys Fluids* 16(5):L35–L38. doi:[10.1063/1.1689711](https://doi.org/10.1063/1.1689711). <http://link.aip.org/link/?PHF/16/L35/1>
75. Parlett BN, Reinsch C (1969) Balancing a matrix for calculation of eigenvalues and eigenvectors. *Numer Math* 13(503):293–304
76. Penzl T (2000) A cyclic low-rank Smith method for large sparse Lyapunov equations. *SIAM J Sci Comput* 21:1401–1418
77. Pernebo L, Silverman L (1982) Model reduction via balanced state space representations. *IEEE Trans Autom Control* 27:382–387
78. Pier B (2002) On the frequency selection of finite-amplitude vortex shedding in the cylinder wake. *J Fluid Mech* 458:407–417
79. Prandtl L (1905) Über Flüssigkeitsbewegung bei sehr kleiner Reibung. *Verhandlungen des dritten internationalen Mathematiker-Kongresses in Heidelberg*
80. Provansal M, Mathis C, Boyer L (1987) Bénard-von Kármán instability: transient and forcing regimes. *J Fluid Mech* 182:1–22
81. Reddy SC, Henningson DS (1993) Energy growth in viscous channel flows. *J Fluid Mech* 252:209–238
82. Reynolds O (1883) An experimental investigation of the circumstances which determine whether the motion of water shall be direct or sinuous, and of the law of resistance in parallel channels. *Philos Trans R Soc Lond* 174:935–982. <http://www.jstor.org/stable/109431>
83. Rowley CW (2005) Model reduction for fluids using balanced proper orthogonal decomposition. *Int J Bifurc Chaos* 15(3):997–1013
84. Rowley CW, Mezic I, Bagheri S, Schlatter P, Henningson DS (2009) Spectral analysis of nonlinear flows. *J Fluid Mech* 641:115–127
85. Ruhe A (1984) Rational Krylov sequence methods for eigenvalue computation. *Linear Algebra Appl* 58:391–405. doi:[10.1016/0024-3795\(84\)90221-0](https://doi.org/10.1016/0024-3795(84)90221-0). <http://www.sciencedirect.com/science/article/B6V0R-45GWNPR-18/2/bd42c81b1a08d43ecbbcd66d74510c7b>
86. Saad Y (1980) Variations on Arnoldi's method for computing eigenvalues of large unsymmetric matrices. *Linear Algebra Appl* 34:269–295. doi:[10.1016/0024-3795\(80\)90169-X](https://doi.org/10.1016/0024-3795(80)90169-X). <http://www.sciencedirect.com/science/article/B6V0R-45GWNCR9-J/2/f5a9c162b4d796b406e56f57b5d2812a>
87. Safonov M, Chiang R (1989) A schur method for balanced-truncation model reduction. *IEEE Trans Autom Control* 34(7):729–733. doi:[10.1109/9.29399](https://doi.org/10.1109/9.29399)
88. Schlatter P, Bagheri S, Henningson DS (2010) Self-sustained global oscillations in a jet in crossflow. *Online first* (<http://www.springerlink.com/content/j325x70863266701/>)
89. Schlichting H, Gersten K (2000) *Boundary-layer theory*. Springer, Heidelberg
90. Schmid PJ (2010) Dynamic mode decomposition of numerical and experimental data. *J Fluid Mech* 656:5–28
91. Schmid PJ, Henningson DS (2001) *Stability and transition in shear flows*. Springer, New York
92. Schrauf G (2005) Status and perspectives of laminar flow. *Aeronaut J* 109(1102):639–644
93. Sipp D, Lebedev A (2007) Global stability of base and mean flows: a general approach and its applications to cylinder and open cavity flows. *J Fluid Mech* 593:333–358
94. Smith BL, Glezer A (1998) The formation and evolution of synthetic jets. *Phys Fluids* 10(9):2281–2297. doi:[10.1063/1.869828](https://doi.org/10.1063/1.869828). <http://link.aip.org/link/?PHF/10/2281/1>
95. Smith RA (1968) Matrix equation  $xa + bx = c$ . *SIAM J Appl Math* 16(1):198–201. <http://www.jstor.org/stable/2099416>
96. Sorensen D (1992) Implicit application of polynomial filters in a  $k$ -step Arnoldi method. *SIAM J Matrix Anal Appl* 13:357–385
97. Strykowski PJ, Niccum DL (1992) The influence of velocity and density ratio on the dynamics of spatially developing mixing layers. *Phys Fluids* 4(4):770–781. doi:[10.1063/1.858294](https://doi.org/10.1063/1.858294). <http://link.aip.org/link/?PFA/4/770/1>
98. Temam R (1997) *Infinite dimensional dynamical systems in mechanics and physics*, 2nd edn. Springer, New York
99. Theofilis V (2005) Advances in global linear instability analysis of nonparallel and three-dimensional flows. *Prog Aerosp Sci* 39:249–315
100. Theofilis V, Hein S, Dallmann U (2000) On the origins of unsteadiness and three-dimensionality in a laminar separation bubble. *Philos Trans R Soc Lond A* 358:3229–3246
101. Thiria B, Wesfreid JE (2007) Stability properties of forced wakes. *J Fluid Mech* 579:137–161. doi:[10.1017/S0022112007004818](https://doi.org/10.1017/S0022112007004818)

102. Trefethen LN (1997) Pseudospectra of linear operators. *SIAM Rev* 39(3):383–406
103. Trefethen LN, Bau D (1997) *Numerical linear algebra*. SIAM, Philadelphia
104. Trefethen LN, Embree M (2005) *Spectra and pseudospectra—the behavior of nonnormal matrices and operators*. Princeton University Press, New Jersey
105. Waleffe F (1990) On the three-dimensional instability of strained vortices. *Phys Fluids* 2(1):76–80. doi:10.1063/1.857682. <http://link.aip.org/link/?PFA/2/76/1>
106. Zhou K, Doyle JC, Glover K (2002) *Robust and optimal control*. Prentice Hall, New Jersey